



---

# Computational and Experimental Study of thin films of polymer blends

---

*Author:*

Mireille M Megnidio

*Supervisor:*

Dr Giuseppe Pellicane

*Co-Supervisor:*

Prof Genene Tessema Mola

Submitted in fulfillment of the academic requirements for the Doctoral Degree in Physics

School of Chemistry and Physics

College of Agriculture, Engineering and Science

University of KwaZulu-Natal

Pietermaritzburg

South Africa

March 23, 2016

To the loving memory of my late mother, Mawouet Madeleine.

# Preface

The research contained in this thesis was completed by the candidate while based in the Discipline of Physics, School of Chemistry and Physics of the College of Agriculture, Engineering, and Science, University of Kwazulu-Natal.

The research was financially supported by College of Agriculture, Engineering and Science.

The content of this work have not been submitted in any form to another university and, except where the work of other others in acknowledged in the text, the results reported are due to investigation by the candidate.

Signed: \_\_\_\_\_

Date: \_\_\_\_\_

## Declaration - Plagiarism

I, Mireille Merlise Megnidio-Tchoukouegno declare that

1. The research reported in this thesis, except where otherwise indicated, is my original research.
2. This thesis has not been submitted for any degree or examination at any other university.
3. This thesis does not contain other persons' data, pictures, graphs or other information, unless specifically acknowledged as being sourced from other persons.
4. This thesis does not contain other persons' writing, unless specifically acknowledged as being sourced from other researchers. Where other written sources have been quoted, then:
  - a. Their words have been rewritten but the general information attributed to them has been referenced.
  - b. Where their exact words have been used, then their writing has been placed in italics and inside quotation marks, and referenced.
5. where I have used material for which publication followed, I have indicated in detail my role in the work.
6. this thesis is primarily a collection of materials, prepared by my myself, published as journal articles or presented as a poster and oral presentations at conferences. In some cases, additional material has been included;
7. This thesis does not contain, text, graphics or tables copied and pasted from the Internet, unless specifically acknowledged, and the source being detailed in the thesis and in the References section.

Signed: \_\_\_\_\_

Date: \_\_\_\_\_

## Declaration - Publications

My role in each paper is indicated below each publication.

1. Title : Surface enrichment driven by polymer topology  
Authors : M. Megnidio Tchoukouegno, G. Pellicane, G. T. Mola, and M. Tsigé  
Status : Submitted ( *Physical Review Letters* (**87**, 101, (2014)))  
Reference code: LM14966  
My role in this article was to perform the computer simulations, analyze the data, prepare the figures/tables, and help in the editing of the manuscript.
1. Title : Molecular Dynamics of linear-cyclic polymer blends in the presence of a low-energy interface  
Authors : M. Megnidio Tchoukouegno, G. Pellicane, and M. Tsigé  
Status : In preparation  
My role in this article is to perform the computer simulations, analyze the data, prepare the figures/tables, and helping in the editing of the manuscript.
1. Title : The effect of solvent preparation additives in P3HT-PCBM blends  
Authors : M. Megnidio Tchoukouegno, G. Pellicane, and G. T. Mola  
Status : In preparation  
My role in this article is to perform the experiments, analyze the data and helping in the editing of the manuscript.

Signed: \_\_\_\_\_

Date: \_\_\_\_\_

## Abstract

Quantification of the effect of architecture in the surface segregation of polymer blends is of extreme importance in the area of adhesion, friction, and wetting. In the area of biomaterials, the near-surface composition controls the binding affinity of proteins, as well as focal and bacterial adhesion. For blends of linear and cyclic polymers, results from recent experiments using polystyrene polymers provided evidence on the enrichment of linear chains at the surface, contradicting the once accepted conclusion from theory that cyclic polymers should be in excess at the surface independently of molecular weight of the polymers. In order to resolve this discrepancy between theory and experiment, we have used extensive molecular dynamics simulations to systematically examine the surface segregation behavior of a coarse-grained model for a blend of linear and cyclic polymer chains possessing the same monomer chemistry. We have investigated the role of enthalpic and entropic factors in determining which of the two chain architectures enrich the surface at a given molecular weight. The findings of the present research are significant and prompted us to submit a preliminary report of our investigation to the renowned journal *Physical Review Letters*, where our results may find a proper venue and attract the broad interest of researchers working in the area of surface science, biomaterials, and surface chemistry.

A number of experiments were conducted in the fabrication and characterization of thin film organic solar cells with the view to understand the relation between device performance and the homogeneity of the blend in the photoactive medium. We employed solvent additive in an effort to improve the miscibility of P3HT and PCBM molecules. We have chosen highly effective additive solvents such as 1,8-diodooctane (DIO), 1-chloronaphthalene (CN) and dimethyl sulfoxide (DMSO) in the preparation of P3HT:PCBM active layer. The addition of these solvent additives is expected to create better crystalline domains of the polymer films, and hence, improve the nanoscale morphology of the active layer as well as the charge transport properties in organic thin film medium. The effect of these solvent additives was thoroughly examined and discussed in terms of optical, electrical and structural properties of the polymer blend.

# Contents

<b>List of Figures</b>	<b>iv</b>
<b>List of Tables</b>	<b>xi</b>
<b>1 Introduction</b>	<b>1</b>
1.1 Rationale for Research . . . . .	1
1.2 Aims and Objectives . . . . .	3
1.3 Overview . . . . .	4
<b>2 Literature Review</b>	<b>7</b>
2.1 Computational models for topologically-different polymer blends . . . . .	7
2.2 Computational models for conducting polymer blends . . . . .	10
2.3 Experimental approach . . . . .	13
2.3.1 Optical properties of organic photovoltaic materials . . . . .	13
2.3.2 Device parameters of a solar cell . . . . .	14
2.3.3 Equivalent electrical circuit models for OTFSC devices . . . . .	15
2.3.4 Effect of morphology on the performance of the cell . . . . .	16
<b>3 Tuning the Computational approach to the Model</b>	<b>18</b>
3.1 Introduction . . . . .	18
3.2 Model and Methods . . . . .	19
3.3 Linear Polymers . . . . .	27
3.4 Cyclic Polymers . . . . .	34
3.5 Linear-Cyclic mixtures . . . . .	40
3.6 Conclusions . . . . .	47
<b>4 Free-standing Linear-Cyclic Polymer Blends</b>	<b>48</b>
4.1 Introduction . . . . .	48
4.2 Model and Methods . . . . .	49
4.3 The Low Cyclic Composition Regime . . . . .	52
4.3.1 Density and Local Composition Profiles . . . . .	52

4.3.2	Radius of Gyration . . . . .	57
4.3.3	Instantaneous Interface . . . . .	63
4.3.4	Diffusion coefficients . . . . .	67
4.3.5	Interaction Energies of polymer species . . . . .	72
4.3.6	Percolation . . . . .	76
4.4	The equimolar regime . . . . .	80
4.4.1	Density and Local Composition Profiles . . . . .	80
4.4.2	Radius of Gyration . . . . .	81
4.4.3	Instantaneous Interface . . . . .	83
4.4.4	Diffusion coefficients . . . . .	86
4.4.5	Interaction Energies of polymer species . . . . .	86
4.4.6	Percolation . . . . .	88
<b>5</b>	<b>Experimental study of polymer blends</b>	<b>90</b>
5.1	Introduction . . . . .	90
5.2	Material and Methods . . . . .	91
5.3	Solar cell parameters . . . . .	92
5.3.1	Space Charge limited current . . . . .	94
5.4	Results and Discussion . . . . .	95
5.4.1	Optical absorption properties of the devices . . . . .	95
5.4.2	Electrical properties of the devices . . . . .	96
5.4.3	Comparison on the effect of various additives on performance of OTFSC . .	102
5.4.4	Charge transport properties on solvent mixtures . . . . .	103
5.5	Surface Morphologies of the Photoactive layers . . . . .	104
<b>6</b>	<b>Conclusions</b>	<b>107</b>
<b>7</b>	<b>Bibliography</b>	<b>110</b>

# List of Figures

1.1	Chemical structures of P3HT monomers and PCBM molecules. . . . .	2
2.1	Chemical structures of P3HT and C <sub>60</sub> with CG sites depicted and labeled. . . . .	11
2.2	Chemical structures of P3HT and PCBM with CG sites depicted. The intramolecular degrees of freedom between the CG particles of P3HT monomers are highlighted. . . . .	13
2.3	Schematic current-voltage characteristics of bulk heterojunction solar cells in (a) linear and (b) semilogarithmic representation. . . . .	14
2.4	Equivalent circuit diagram of ideal solar cells. . . . .	15
2.5	Equivalent circuit diagram of real solar cells. . . . .	16
3.1	FENE and Lennard-Jones Potentials. . . . .	21
3.2	Plot of reduced pressure versus time (top) and reduced temperature versus time (bottom) for MD simulations of linear polymers. . . . .	30
3.3	Wall 9-3 Lennard-Jones potential shifted at distance $z = 47.67\sigma$ . . . . .	30
3.4	Number density distribution, $\rho(z)/\rho_0$ versus distance $z$ from the wall of linear polymers coms for $t = 0$ (top) and $t = 5 \times 10^7 \Delta t$ (bottom). The interval between vertical bar on the $z$ -axis is the range of distances where the wall-bead potential is active. For consistency, the same bin size was used for both configurations. This bin size is given by $2\bar{R}_g = 7.16\sigma$ where $\bar{R}_g$ is the average radius of gyration. . . . .	31
3.5	Percentage difference of the distribution density as a function of distance $z$ from the wall for linear polymers. . . . .	32
3.6	Percentage distribution of linear polymers ( $\Theta$ ) as a function of radius of gyration ( $R_g$ ) for $t = 0$ (top) and $t = 5 \times 10^7 \Delta t$ (bottom). . . . .	32
3.7	Plot of reduced pressure versus time (top) and reduced temperature versus time (bottom) for MD simulations of cyclic polymers. . . . .	34
3.8	Wall 9-3 Lennard-Jones potential shifted at distance $z = 47.72\sigma$ . . . . .	37

3.9	Number density distribution, $\rho(z)/\rho_0$ versus distance $z$ from the wall of cyclic polymers for MD simulations $t = 0$ (top) and $t = 5 \times 10^7 \Delta t$ (bottom). The interval between vertical bar on the $z$ -axis is the range of distances where the wall-bead potential is active. For both configurations, the bin size of $2\bar{R}_g = 5.10\sigma$ were used.	38
3.10	Percentage difference of distribution density as a function of distance $z$ from the wall for cyclic polymers. . . . .	39
3.11	Percentage distribution of cyclic polymers ( $\Theta$ ) as a function of radius of gyration ( $Rg$ ) for $t = 0$ (top) and $t = 5 \times 10^7 \Delta t$ (bottom). . . . .	39
3.12	Plot of reduced pressure versus time (top) and reduced temperature versus time (bottom) for MD simulations of linear-cyclic polymers in melt. . . . .	43
3.13	Wall 9-3 Lennard-Jones potential shifted at distance $z = 47.35\sigma$ . . . . .	43
3.14	Number density distribution, $\rho(z)/\rho_0$ versus distance $z$ from the wall for linear and cyclic polymers blend for $t = 0$ (top) and $t = 5 \times 10^7 \Delta t$ (bottom). The interval between vertical bar on the $z$ -axis is the range of distances where the wall-bead potential is active. For both configurations, the bin size of $2\bar{R}_g = 6.80\sigma$ for linear and $2\bar{R}_g = 5.20\sigma$ for cyclic polymers were used. . . . .	44
3.15	Percentage difference of the distribution density as a function of distance $z$ from the wall for linear-cyclic polymers. . . . .	45
3.16	Percentage distribution of linear-cyclic polymers blend ( $\Theta$ ) as a function of radius of gyration ( $Rg$ ) for $t = 0$ (top) and $t = 5 \times 10^7 \Delta t$ (bottom). . . . .	45
4.1	Sketch of the construction of the histogram for the number of crosses resulting from the instantaneous interface for a two-dimensional system of crosses and circles. . .	52
4.2	Local density profiles of free-standing films made of 7-mers (leftmost panels), 10-mers (middle panels), and 20-mers (rightmost panels) chains at low cyclic concentrations: $c^0 = 0.8$ (top panels) and 0.7 (bottom panels). . . . .	54
4.3	Local density profiles of free-standing films made of 30-mers (leftmost panels), 50-mers (middle panels), and 100-mers (rightmost panels) chains at low cyclic concentrations: $c^0 = 0.8$ (top panels) and 0.7 (bottom panels). . . . .	54
4.4	Local Composition profile of free-standing films made of 7-mers (leftmost panels), 10-mers (middle panels), and 20-mers (rightmost panels) chains at low cyclic concentrations: $c^0 = 0.8$ (top panels) and 0.7 (bottom panels). . . . .	55
4.5	Local Composition profile of free-standing films made of 30-mers (leftmost panels), 50-mers (middle panels), and 100-mers (rightmost panels) chains at low cyclic concentrations: $c^0 = 0.8$ (top panels) and 0.7 (bottom panels). . . . .	55

4.6	Top panel: particle density histogram as a function of the distance from the interface for $c = 0.7$ . The pair of bottom curves are for cyclic chains; upper ones for linear chains. Error bars smaller than the size of the symbol are not reported. Inset: zoom of the region nearby the interface. Bottom panel: local composition plot for linear polymers as a function of the distance from the interface. Data are scaled by the <i>bulk</i> composition $c_0 = 0.7$ . Error bars smaller than the size of the symbol are not reported. . . . .	56
4.7	Average perpendicular component radius of gyration of free-standing films made of 7-mers (leftmost panels), 10-mers (middle panels), and 20-mers (rightmost panels) chains at low cyclic concentrations: $c^0 = 0.8$ (top panels) and 0.7 (bottom panels).	58
4.8	Average perpendicular component radius of gyration of free-standing films made of 30-mers (leftmost panels), 50-mers (middle panels), and 100-mers (rightmost panels) chains at low cyclic concentrations: $c^0 = 0.8$ (top panels) and 0.7 (bottom panels).	58
4.9	Left panel: Parallel component of the radius of gyration $R_g^P$ as a function of the distance from the interface for linear (full line) and cyclic polymers (dashed line). $R_g^P$ is scaled by its <i>bulk</i> value $R_{g,b}^P$ . Pair of curves starting at $z^* = 0.5$ are for $N_b = 10$ ; pair of curves starting at $z^* = 2.5$ are for $N_b = 100$ . Right panel: same as in the left panel for the transverse component $R_g^T$ as a function of the distance from the interface. . . . .	60
4.10	Average parallel component of the radius of gyration of free-standing films made of 7-mers (leftmost panels), 10-mers (middle panels), and 20-mers (rightmost panels) chains at low cyclic concentrations: $c^0 = 0.8$ (top panels) and 0.7 (bottom panels).	62
4.11	Average parallel component radius of gyration of free-standing films made of 30-mers (leftmost panels), 50-mers (middle panels), and 100-mers (rightmost panels) chains at low cyclic concentrations: $c^0 = 0.8$ (top panels) and 0.7 (bottom panels).	62
4.12	Left panel: Exponent of the mean square radius of gyration $R_g^P$ as a function of the distance from the interface for cyclic polymers at composition $c_0 = 0.7$ . Left panel corresponds to the estimate performed by using all the chain lengths. Right panel corresponds to the case where at $z^* = 2.5$ , the case $N_b = 100$ was excluded. . . . .	64
4.13	Average percentage number of polymer species made of 7-mers (leftmost panels), 10-mers (middle panels), and 20-mers (rightmost panels) chains at low cyclic concentrations: $c^0 = 0.8$ (top panels) and 0.7 (bottom panels). . . . .	65
4.14	Average percentage number of polymer species made of 30-mers (leftmost panels), 50-mers (middle panels), and 100-mers (rightmost panels) chains at low cyclic concentrations: $c^0 = 0.8$ (top panels) and 0.7 (bottom panels). . . . .	65

4.15	Left panel: histogram of the percentage of chain-ends of linear polymers as a function of the distance from the interface. Right panel: same as in the left panel for the percentage of middle-beads of linear polymers. . . . .	66
4.16	(a): Sketch of a configuration for a linear polymer with chain-ends attached to the interface and middle bead close to the interface. (b): same as in (a) for the case in which the middle bead is far away from the interface. . . . .	67
4.17	Average percentage number of chain-ends and middle points of linear polymers made of 7-mers (leftmost panels), 10-mers (middle panels), and 20-mers (rightmost panels) chains at low cyclic concentrations: $c^0 = 0.8$ (top panels) and 0.7 (bottom panels). . . . .	68
4.18	Average percentage number of chain-ends and middle points of linear polymers made of 30-mers (leftmost panels), 50-mers (middle panels), and 100-mers (rightmost panels) chains at low cyclic concentrations: $c^0 = 0.8$ (top panels) and 0.7 (bottom panels). . . . .	68
4.19	Transverse component of the diffusion coefficient as a function of distance from the surface for polymer species made of 30-mers (leftmost panels), 50-mers (middle panels), and 100-mers (rightmost panels) chains at low cyclic concentrations: $c^0 = 0.8$ (top panels) and 0.7 (bottom panels). . . . .	71
4.20	Transverse component of the diffusion coefficient as a function of distance from the surface for polymer species made of 7-mers (leftmost panels), 10-mers (middle panels), and 20-mers (rightmost panels) chains at low cyclic concentrations: $c^0 = 0.8$ (top panels) and 0.7 (bottom panels). . . . .	72
4.21	Time-averaged components of the mean square displacement of cyclic (top) and linear (bottom) chains as a function of time for different blend regions as reported in the legend. Thickness of the selected region is $\sigma$ . Results are shown for $N_b = 10$ (left panels), 30 (middle panels) and 100 (right panels) at $c^0 = 0.7$ . <i>Time</i> is in units of $10^4$ timesteps. . . . .	72
4.22	Parallel component of the diffusion coefficient as a function of distance from the surface for polymer species made of 7-mers (leftmost panels), 10-mers (middle panels), and 20-mers (rightmost panels) chains at low cyclic concentrations: $c^0 = 0.8$ (top panels) and 0.7 (bottom panels). . . . .	73
4.23	Parallel component of the diffusion coefficient as a function of distance from the surface for polymer species made of 30-mers (leftmost panels), 50-mers (middle panels), and 100-mers (rightmost panels) chains at low cyclic concentrations: $c^0 = 0.8$ (top panels) and 0.7 (bottom panels). . . . .	73

4.24	Energy per bead of different polymer species as a function of distance from the surface for polymer species made of 7-mers (leftmost panels), 10-mers (middle panels), and 20-mers (rightmost panels) chains at low cyclic concentrations: $c^0 = 0.8$ (top panels) and 0.7 (bottom panels). ALL refers to the energy per bead as calculated regardless of the nature of the bead. SELF refers to the energy per bead as calculated by considering beads belonging to the same polymer species only. . . . .	74
4.25	Transverse component of the diffusion coefficient as a function of distance from the surface for polymer species made of 30-mers (leftmost panels), 50-mers (middle panels), and 100-mers (rightmost panels) chains at low cyclic concentrations: $c^0 = 0.8$ (top panels) and 0.7 (bottom panels). ALL refers to the energy per bead as calculated regardless of the nature of the bead. SELF refers to the energy per bead as calculated by considering beads belonging to the same polymer species only. . .	77
4.26	Energy per bead as a function of the distance from the interface. . . . .	78
4.27	Percentage of percolating clusters starting from the interface as a function of the distance from it for polymer species made of 7-mers (leftmost panels), 10-mers (middle panels), and 20-mers (rightmost panels) chains at low cyclic composition: $c^0 = 0.7$ . Upper panels are the results for linear chains. Bottom panels for cyclic chains. Insets report the average number of polymers per cluster as a function of the distance from the interface. . . . .	79
4.28	Percentage of percolating clusters starting from the interface as a function of the distance from it for polymer species made of 30-mers (leftmost panels), 50-mers (middle panels), and 100-mers (rightmost panels) chains at low cyclic composition: $c^0 = 0.7$ . Upper panels are the results for linear chains. Bottom panels for cyclic chains. Insets report the average number of polymers per cluster as a function of the distance from the interface. . . . .	80
4.29	Local density profiles of free-standing films made of 7-mers, 10-mers, 20-mers (top panel: from left to right), 30-mers, 50-mers, and 100-mers (bottom panel: from left to right) at equimolar composition. . . . .	81
4.30	Local Composition profile of free-standing films made of 7-mers, 10-mers, 20-mers (top panel: from left to right), 30-mers, 50-mers, and 100-mers (bottom panel: from left to right) at equimolar composition. . . . .	82
4.31	Average perpendicular component radius of gyration of 7-mers, 10-mers, 20-mers (top panel: from left to right), 30-mers, 50-mers, and 100-mers (bottom panel: from left to right) at equimolar composition. . . . .	83
4.32	Average parallel component of the radius of gyration of free-standing films of 7-mers, 10-mers, 20-mers (top panel: from left to right), 30-mers, 50-mers, and 100-mers (bottom panel: from left to right) at equimolar composition. . . . .	84

4.33	Average percentage number of polymer species made of 7-mers, 10-mers, 20-mers (top panel: from left to right), 30-mers, 50-mers, and 100-mers (bottom panel: from left to right) at equimolar composition. . . . .	85
4.34	Average percentage number of chain-ends and middle points of linear polymers made of 7-mers, 10-mers, 20-mers (top panel: from left to right), 30-mers, 50-mers, and 100-mers (bottom panel: from left to right) at equimolar composition. . . . .	86
4.35	Parallel component of the diffusion coefficient as a function of distance from the surface for polymer species made of 7-mers, 10-mers, 20-mers (top panel: from left to right), 30-mers, 50-mers, and 100-mers (bottom panel: from left to right) at equimolar composition. . . . .	87
4.36	Transverse component of the diffusion coefficient as a function of distance from the surface for polymer species made of 7-mers, 10-mers, 20-mers (top panel: from left to right), 30-mers, 50-mers, and 100-mers (bottom panel: from left to right) at equimolar composition. . . . .	87
4.37	Energy per bead of different polymer species as a function of distance from the surface for polymer species made of 7-mers, 10-mers, 20-mers (top panel: from left to right), 30-mers, 50-mers, and 100-mers (bottom panel: from left to right) at equimolar composition. ALL refers to the energy per bead as calculated regardless of the nature of the bead. SELF refers to the energy per bead as calculated by considering beads belonging to the same polymer species only. . . . .	89
4.38	Percentage of percolating clusters starting from the interface as a function of the distance from it for polymer species made of 10-mers (leftmost panels), 30-mers (middle panels), and 50-mers (rightmost panels) at equimolar composition. Upper panels are the results for linear chains. Bottom panels for cyclic chains. Insets report the average number of polymers per cluster as a function of the distance from the interface. . . . .	89
5.1	Equivalent circuit diagram of ideal solar cells. . . . .	93
5.2	J vs V graph of organic thin film based solar cell under dark conditions. . . . .	94
5.3	Optical absorption spectra of four different organic active layers of P3HT:PCBM blend fabricated with and without different solvent additive. . . . .	95
5.4	J-V characteristics of organic thin film solar cell devices based on the blend of P3HT:PCBM active layer prepared without additive under illumination and dark conditions. . . . .	97
5.5	J-V characteristics of organic thin film solar cell devices based on the blend of P3HT:PCBM active layer prepared with DIO under illumination (top) and dark conditions (bottom). . . . .	99

5.6	J-V characteristics of organic thin film solar cell devices based on the blend of P3HT:PCBM active layer prepared with CN under illumination and dark conditions.	100
5.7	J-V characteristics of organic thin film solar cell devices based on the blend of P3HT:PCBM active layer prepared with DMSO under illumination and dark conditions. . . . .	101
5.8	J-V characteristics of the four different organic thin film solar cell devices based on blended active layer of P3HT:PCBM prepared with different organic solvent mixture.	102
5.9	J vs V graph for a hole only diode of P3HT:PCBM prepared without and with solvent additives of OTFSC. The solid lines are computer fits according to Eq. (5.8) occurring at high forward biases, while the black squares are experimental data. . . .	104
5.10	Scanning electron microscopy images of P3HT:PCBM blend films OTFSC spin coated from chloroform and mixed solvent: (top) without additive (a) with DIO; (b) with CN; and (c) with DMSO. . . . .	106

# List of Tables

2.1	Temperatures and Mixture Ratios of Atomistic Systems (pressure = 1 atm in all cases). . . . .	11
3.1	Some physical quantities and model parameters of interest expressed in LJ units. .	26
3.2	Properties of linear polymers near a flat wall: $z$ is the distance from the wall, $\overline{R}_g^{lin}$ the average radius of gyration and $\sigma^{lin}$ stands for variance. . . . .	33
3.3	Properties of cyclic polymers near a flat wall: $z$ is the distance from the wall, $R_g^{cyc}$ average radius of gyration and $\sigma^{cyc}$ stands for variance. . . . .	37
3.4	Properties of linear polymers near a flat wall in melt state: $z$ is the distance from the wall, $\overline{R}_g^{lin}$ average radius of gyration and $\sigma^{lin}$ stands for variance. . . . .	46
3.5	Properties of cyclic polymers near a flat wall in melt state: $z$ is the distance from the wall, $R_g^{cyc}$ average radius of gyration and $\sigma^{cyc}$ stands for variance. . . . .	46
4.1	Local compositions (linear polymers) vs chain length . . . . .	57
4.2	Values of radii of gyration $Rg$ of linear and cyclic com chains. . . . .	61
4.3	Values of radii of gyration $Rg$ of linear and cyclic com chains. . . . .	63
4.4	Values of diffusion coefficient in the bulk of linear and cyclic com chains computed from the slope of MSD in the linear regime using Einstein relation. . . . .	69
4.5	Values of diffusion coefficient in the bulk of linear and cyclic com chains computed from the slope of MSD in the linear regime using Einstein relation. . . . .	70
5.1	Photovoltaic parameters of best performed diodes of organic thin film solar cell devices based on the blend of P3HT:PCBM active layer prepared without additive. . . . .	96
5.2	Photovoltaic parameters of best performed diodes of organic thin film solar cell devices based on the blend of P3HT:PCBM active layer prepared with DIO processing solvent additive. . . . .	98
5.3	Photovoltaic parameters of best performed diodes of organic thin film solar cell devices based on the blend of P3HT:PCBM active layer prepared with CN processing solvent additive. . . . .	99

5.4	Photovoltaic parameters of best performed diodes of organic thin film solar cell devices based on the blend of P3HT:PCBM active layer prepared with DMSO processing solvent additive. . . . .	101
5.5	Photovoltaic parameters of the four different organic thin film solar cell devices based on the blend of P3HT:PCBM active layer prepared with different organic solvent mixture. . . . .	103
5.6	Summary of the transport parameters. . . . .	104

# Acknowledgments

Firstly I would like to give thanks to Dr Giuseppe Pellicane who give this chance. Dr Giuseppe Pellicane (supervisor), has been exceptional in grooming me to be a better post graduate student as well as highly knowledgeable in this field statistical physics and thermodynamics. Without his constant efforts towards superior guidance, the work represented in this thesis would have not being completed on time or be off the same high quality. I would also like to acknowledge Prof Gennene Mola and Prof Tsige for their support and guidance during the scientific collaboration with us. All the academic and support staff here in UKZN Pietermaritzburg have contributed considerably to my personal development and have been most helpful whenever they are called upon for assistance or advice. Last but not least, I give the utmost thanks to the College of Agriculture, Engineering and Science for financial support throughout my PhD research work.

I am thankful to members of staffs at Microscopy and Microanalysis Unit (MMU) in the School of Life Sciences, UKZN.

I owe much to my colleagues at the School of Chemistry and Physics of the University of KwaZulu-Natal, Pietermaritzburg for their support during this period of hard work. Special thanks goes to Elhadi, Saheed, Bezuneh and Francis.

I am very grateful to my loving husband Medard for his love and support during my PhD research work. I am also thankful to him for proofreading parts of my thesis and made useful comments that helpt improve the quality of my thesis.

I am very grateful to my lovely children for their love and for been part of my life.

I am so grateful to my friends and sisters Yinka, Pemba, Verithas, Vera, Harmony for their support in diverse situations. Special thanks to Chantal, Sylvester and Joanne. My sincere appreciation to the members of the Cameroonian Community in Pietermaritzburg. Thanks to you guys, on many occasions I felt at home far from home.

Finally, I am thankful to my whole family in Cameroon and abroad, including my second mother Chantal Lapnet, my father, my brothers and sisters, uncles and aunts.

# Chapter 1

## Introduction

### 1.1 Rationale for Research

One of the biggest challenges facing developing/developed countries is the society's growing demand for energy from renewable, sustainable and non-polluting sources. In fact, industrial development and population growth are the main factors which call for a decreasing dependency on fossil fuels, and a progressive phasing out of the use of them at least ten to twenty years before the peak oil is reached, according to the Hirsch report created on request by the US Department of Energy in 2005 [1]. The imperative of looking for alternative energy sources, as dictated by the rapidly approaching energy shortfall, has boosted research in solar cells. Solar power based on crystalline Silicon technology is not economically competitive with fossil fuels. Therefore, the search for cheaper renewable sources of energy has motivated organic electronics research based on conducting polymers, which have been intensively investigated in the last few years because of the relatively abundant and inexpensive materials needed and the low manufacturing costs [2]. However, the fast degradation of the organic molecule under ambient environmental conditions is a major challenge slowing the realization of organic photovoltaics in the energy market. Moreover, a power conversion efficiency (PCE) of 10% or more is regarded as an important threshold for practical implementation and large-scale commercial usage of polymer solar cells. Theoretical predictions suggest that the power conversion efficiency of organic thin film solar cells (OTFSC) solar cells can rise as high as 15% [3]. So far, most of the best performing organic photovoltaic cells were fabricated using the bulk heterojunction active layer [3]. This design consists of a photoactive layer realized by blending electron-donor polymers with electron-acceptor ones, as for instance poly(3-hexylthiophene) (P3HT), that is a semiconductor conjugated polymer acting as a electron-donor material, and a small-nanoparticle compound named phenyl-C<sub>61</sub>-butyric acid methyl ester (PCBM) that is an electron-acceptor polymer which is introduced to make the dissociations of the excitons more effective. The P3HT polymer chain is made up of monomers consisting of a thiophene ring and the lateral chain of two methyl groups. The thiophene ring consists of carbon,

hydrogen and sulphur atoms. The PCBM is the modification of  $C_{60}$  (which resembles a soccer ball) with an additional molecular group attached to two carbons of the fullerene cage. The function of this additional molecular group is to make the molecule soluble in organic solvents. A schematic illustration of the two molecules can be seen in figure 1.1. Photoexcitation in an organic semiconductor does not result in free charges, but in the formation of an exciton (bound electron-hole pair). Then, dissociation of the exciton at the interface of the two polymers domains generates charges contributing to conduction. Despite it was suggested that nearly 80% external quantum efficiency can be achieved in conjugated polymers active layers[4], the power conversion efficiency of the devices still remain below 10%. Reason for that is related to the exciton diffusion

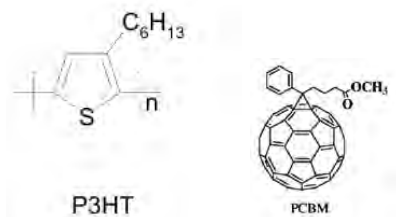


Figure 1.1: Chemical structures of P3HT monomers and PCBM molecules.

length at room temperature, which is of the order of 5-10 nm whereas the typical layer thickness is  $< 200$  nm. Then, the only possibility for the excitons to contribute to conduction by dissociation is that donor and acceptor materials are mixed together to form the bicontinuous network called bulk heterojunction (BHJ), otherwise the exciton will not reach the interface between the two polymers and will not dissociate. Ideally, the generated excitons are distant from the donor-acceptor interface less than a diffusion length. This can be achieved by creating an homogeneous blend of the two materials, where the interface-to-volume ratio is maximized. Then, it appears evident that whereas the excitons generated close to the electrodes (within the average diffusion exciton length) clearly contribute to conduction, the ones generated far from the electrodes can contribute to conduction only if a percolating path of the two polymers exists from the cathode to the anode. Then, low power conversion efficiencies are due to the fact that the photogenerated charge carriers are not collected by the electrodes because of the short diffusion length of the excitons and of recombination processes preventing them from reaching the electrodes [5]. However, the optimal morphology conditions of the blend, which are able to enhance the power conversion efficiency (PCE) of the solar cell remain elusive, also due to the difficulty to observe the molecular-scale structure of the blend by using standard experimental techniques as X-ray diffraction [6, 7], atomic force microscopy [8, 9], optical spectroscopy [7], and near-edge X-ray absorption fine structure spectroscopy [10]. A basic understanding of the structural of arrangement of molecules in OTFSC is crucial to continuously enhance the efficiency of solar energy harvesting. But, our knowledge of these properties is limited due to lack of a clear, microscopic understanding of the behaviour of these materials.

A more general problem, whose interest goes beyond semiconductor conjugated polymers is the

fundamental understanding of the role of the polymer molecular topology on surface adsorption. This type of research is typically conducted by mixing two polymers having the same repeat-chemistry but different chain architecture, so that surface enrichment occurs by virtue of architectural differences. For instance, in OTFSC polymers blends, one of the polymers possesses an elongated shape (e.g. P3HT), and the other one is a nanoparticle with a more compact shape (e.g. PCBM). The surface is generated by the presence of the electrode. The role of polymer topology in determining polymer percolation starting from the surface is not properly understood, as well as the polymer blend structure near the electrode. Another important feature to improve the photovoltaic conversion efficiency in bulk heterojunction OTFSC, as it is emerging from the discussion reported above, is the formation of an interpenetrating network of electron donor/acceptor domains compatible with the exciton diffusion length, and ensuring the percolation path in order to facilitate the charge transfer.

The interest in studying coarse-grained models of topologically-different polymer blends is also due to the fact that self-organization and rheology of polymer blends at the interface are of both fundamental and industrial interest [11, 12, 13], and the topology of polymers is expected to strongly influence the dynamical properties of the system, especially when the packing fraction is high. A number of studies analyzed the way the different repeat chemistry of chains affects polymer diffusion [11, 14, 15, 16, 17], however, the role of chain architecture and molecular mass in determining the species that preferentially adsorbs at the interface is not yet well understood. The interest in these investigations is also related to the possibility to control surface segregation of materials with polymers of chosen topology [12]. Experiments to resolve the matter are typically conducted by mixing up polymers possessing the same repeat chemistry, and different molecular architecture, e.g. branched or ring and linear polymers [18, 19, 20, 21, 22].

Besides, highlighting the role of molecular architecture and the entropy in determining surface behaviour in polymer blends, the study of polymers with different chain topology is also relevant for biological systems [23, 24].

## 1.2 Aims and Objectives

By the computational side, our aim will be to understand the effect of polymer topology in determining surface enrichment in a blend of two polymers, when the system is forced to generate an interface. We will consider a basic model capturing the most essential differences between polymers with an elongated and compact shape, i.e. a binary mixture of linear-cyclic polymers. We will adopt a versatile model, whose results can be easily extrapolated to experimental systems, namely the bead-spring model by Kremer and Grest [25, 26]. Then, we will perform extensive molecular dynamics computer simulations of this model at different compositions and by varying the molecular mass of the polymers. Our objective will be to correlate a number of dynamic and structural properties of the system to the chain length adopted for the polymers, including structural (density

and composition distribution, radii of gyration, percolation), thermodynamic (energy distribution) and dynamical properties (diffusion).

By the experimental research point of view, we will focus on polymer-fullerene BHJ solar cells which contain blends of P3HT and PCBM. Since the performance of these devices is critically dependent on the morphology of the donor and acceptor blend active layer, our aim in this study is to generate different types of morphologies in the P3HT:PCBM active layer by exploiting different processing solvent additives. These additives possess different boiling points, i.e. we used 1,8-diodooctane (DIO), 1-chloronaphthalene (CN), and dimethyl sulfoxide (DMSO), whose boiling points are respectively, 168°C, 250°C and 189°C. Since we used as a reference solvent chloroform (CF) and the boiling point of these additives are higher than that of CF (61.2°C). The devices are expected to increase the nanoscale phase separation in the blend. Our objective will be the one of studying the mechanisms and the effectiveness of the device stability under these conditions. The connection between the power conversion efficiency (PCE) of the device and the different nanomorphologies induced by the additives will also be investigated, as well as the transport properties of the device.

### 1.3 Overview

As for the computational part of the thesis, we firstly achieved a clear understanding of the time-scales involved in the equilibration of bead-spring models of linear-cyclic polymer blends by performing molecular dynamics studies of the system. The results of this preliminary investigation are reported in the next Chapter (Chapter 3), and were particularly useful in order to further investigate the system in depth, and collect information about the relevant *bulk* and interface properties of it. At the same time, we could observe some expected and peculiar structural features as emerging from those calculations, as for instance, the higher flexibility of linear chains as compared to cyclic ones. That was particularly evident in the higher values assumed by the radius of gyration of linear polymers, and also by the higher dispersivity of this quantity. In this first part of the computational study we also considered two different types of interfaces and we generated the systems accordingly: a flat wall-blend and an empty space-blend ones.

Then, in Chapter 4 we focused on vacuum-blend interfaces and we initially considered the low-cyclic composition regime in order to find the signature of any linear polymer preferential enrichment at the interface. The motivation of this research was to confirm some experimental evidence reported in the literature for polystyrene polymer blends that linear chains are preferentially adsorbed at the interface, unlike the theoretical prediction based on a Gaussian Field Theory that cyclic chains should be enhanced regardless of the molecular mass of polymers. Our numerical results for both the polymer density and composition profiles as a function of the distance from the interface provided unambiguous evidence of linear chain enrichment at the interface when short chains (degree of polymerization below 20 beads per polymer) were used, and of cyclic chain

enrichment when the case of long chains was considered (degree of polymerization above 50 beads per polymer). Our subsequent analysis of the microscopic origins of this behaviour was able to explain it in terms of the competition between the enthalpic and entropic contributions to the free energy of the system. We observed a collapse of the effective sizes of the two polymer species as measured by their radius of gyration, when the interface was approached. This was a clear evidence of loss of conformational entropy, that was more marked for the linear chains when the case of long chains was considered. We also monitored the location of chain-ends of linear polymers, and we could detect that they always get preferentially exposed to the empty space. This feature provided evidence that linear chains have an entropic advantage in getting enriched at the interface since it was reported in the scientific literature that this configuration of the system originates some surface potentials of entropic origin. The energy of the two polymer species close to the interface indicated that in the case of short chains, cyclic chains are less favoured energetically to reach the interface because of the topological constraint of the loop geometry. The analysis of the percolation of the two polymer species starting from the interface showed that cyclic chains are on the average percolating through a smaller distance into the *bulk* of the material than the linear chains. Finally the study of the diffusion of the two polymer species provided evidence of a dramatic drop of the mobility of the two species when the interface is approached, with a tendency of cyclic chains to slightly increase their diffusion coefficient with respect to the *bulk* value when the distance to the interface is decreased.

In summary, in the small chain case the fact that cyclic polymers are way less flexible than linear polymers at small degrees of polymerization makes them pack less efficiently and achieve a less than optimal number of pair interactions among their beads. This evidence shed new light on the severe constraint imposed on the flexibility of cyclic polymers by the loop topology when their chain length is small. Then, linear polymers could achieve a lower interfacial free energy than cyclic polymers because they minimize their surface energy more than cyclic chains, while at the same time maximizing their entropy by exposing their chain-ends to the surface. In this scenario, linear enhancement at the interface at short chain lengths is the result of an entropy-mediated process, where also the enthalpy is playing an important role. In the long chain case, we noted that the total energy per bead of the two polymer species becomes now very similar regardless of the distance from the interface, which demonstrates that when chain length is long enough, the loop constraint becomes less important in undermining the flexibility of polymer chains. Cyclic polymers in the long chains case are then likely to achieve a lower interfacial free energy than linear polymers because they possess an higher conformational entropy, while their surface energy is not that different than the one of linear chains. This evidence explains cyclic enhancement at long chain lengths as a genuine entropic process, driven once again by the loop geometry which prevents cyclic chains to fold at the interface as efficiently as linear chains.

When we considered the case of the equimolar mixture (50% – 50% linear-cyclic blend), we

could confirm the main findings emerging from the study of the lower cyclic composition. However, the analysis of the energy of the two polymer species as a function of the distance from the interface was particularly useful in this regime. In fact, the absence of any bias originated by a disproportion of one of the two polymer species allowed us to genuinely provide some neat conclusions about the way the different geometry of the two polymers affects their interfacial energy.

As for the experimental part of this thesis, we investigate P3HT:PCBM OTFSC processed with and without processing solvent additives with different boiling points. This was done in order to optimize the nanomorphology of the OTFSC active layer by creating different morphologies and study the segregation of the films at the surface. The blend without additive was dissolved in chloroform (CF), a host solvent where P3HT and PCBM are both soluble. As processing solvent additives, we used 1,8-diiodooctane (DIO), 1-chloronaphthalene (CN) and dimethyl sulfoxide (DMSO). We expect the addition of these solvent additives to create better ordering domains of polymer film. The nanoscale morphology of the active layer and the charge transport properties of the blend film, play an important role in determining the performance of the OTFSC. This important issues should be aimed for the improvement of the performance. In this chapter, we investigate processing solvent additives effect on the OTFSC blend by examining the optical, electrical and structural properties of the P3HT:PCBM blend prepared with and without solvent additives.

## Chapter 2

# Literature Review

This chapter first gives a brief overview on the literature relevant to get an insight on coarse-grained models of polymer blends. Initially we will consider some models which have been recently adopted to preserve the characteristics of the polymer blends typically found in the BHJ layer. Then, we will focus more on the problem of surface segregation and we will look at the different factors influencing surface segregation of one of the two species when polymer topology is used as a way to achieve this effect. Finally, the past research relevant to understanding of OTFSC technology, the introduction of important details about the history of OTFSC technology, and strategies to improve the performance is reviewed.

### 2.1 Computational models for topologically-different polymer blends

Over a long period of time, the conformational and dynamic properties of both linear and cyclic polymers have created appreciable interest in polymer science due to their topological constraints: lack of chain-ends has a dramatic impact on many physical properties, such as diffusion and the radius of gyration, to name just but a few. Most experimental studies have taken care of the dilute solution behavior of linear and nonlinear polymers [27, 28, 29, 30, 31, 32], and also some theoretical and computational work has been carried out in the *bulk* and at the surface [33, 34, 35, 36, 37]. Similarly, much attention has been paid to the understanding of the effect of structure of cyclic topology in the melt. In their study, Cates and Deutsch [38] suggested that the rings are nearly Gaussian in the short chain regime, while for longer chains the non-connected rings dominate the conformational statistics. These properties are related to the power law the square of the radius of gyration scales with the chain length. In fact, they found that the exponent in the mean-square radius of gyration,  $\langle R_g^2 \rangle \sim N^{2\nu}$ , should be greater 1/3 but less than 1/2 (A Gaussian chain possesses an exponent equal to one). In the long chain regime of the rings, a value of  $\langle R_g^2 \rangle \sim N^{2/3}$  has been

reported [14]. It turned out that the general scaling of the ring polymer sizes mostly depends on the simulation models [39], which stimulated many theoreticians to look deeper in this issue for better understanding these scaling properties. Another interesting point, from the literature focused on the effect of the topological constraint imposed by a ring, is that a modified Flory argument also replicated the asymptotic behavior of the ring size and the crossover behavior between an ideal and a compact polymer statistics [40, 41]. In these studies, topological constraints impose some specific, effective excluded volume interactions on the system. It is also fascinating that a simulation snapshot of ring polymers in a melt allows one to recall the image of segregated chromosomes in a nucleus. Motivated by the above studies, showing knot-free, unentangled conformations similar to the interphase chromosome structures, the study of the physics of rings in a melt has recently come into the spotlight. The general conclusion is that the conformation of rings in the melt differs significantly from that in the solution, as a result of topological constraints active in concentrated systems but not in the dilute solution. In addition to all the studies about the conformational and dynamical properties of the linear and nonlinear polymers blends, it has also been noted that their surface behavior have generated considerable interest in many practical applications such as adhesion, lubrication, and polymer processing. For instance, in multicomponent polymer mixture systems, one of the two components is often preferred at the surface for entropic or enthalpic reasons, therefore making the physical properties of the surface significantly different from the corresponding properties in the *bulk*. In some cases, this is an unwanted effect, and in general it is difficult to estimate the surface composition of the species. Wu and Friedrickson [42] provided another point of view about the surface enrichment of one of the species at the surface by using some qualitative arguments based on a scaled theory. We briefly revise this theory here because of its ability to provide some indications on which of the two polymer species is going to be preferentially adsorbed at the interface in terms of some simple considerations. The thermodynamic quantity playing the driving role in determining which component is enriched at the interface is the surface free energy  $\gamma_k$ , or interfacial tension, of the single components of the blend, and one may expect that the surface will be enriched with the component possessing the smaller surface free energy. It is possible to write the following approximation for the interfacial energy per unit area  $\Phi$  of the total system in terms of the surface tensions of the two polymer species  $\gamma_k$ , where  $\phi_k$  is the volume fraction of species  $k$  in a layer near the surface:

$$\Phi = \gamma_A \phi_A + \gamma_B (1 - \phi_A) \approx \phi_A (\gamma_A - \gamma_B).$$

Then, by using Helfand-Tagami theory:

$$\xi_k \sim \frac{\beta_k}{\sqrt{\alpha_k}}$$

with

$$\beta_k^2 = \frac{b_k^2}{6v_k} = \frac{R_k^2}{V_k}$$

and

$$\gamma_k \sim \alpha_k \xi_k \sim \beta_k \sqrt{\alpha_k},$$

it is possible to show that:

$$\gamma_A - \gamma_B \sim \beta_A \sqrt{\alpha_A} - \beta_B \sqrt{\alpha_B}.$$

According to this equation, the polymer species with the lowest value of  $\beta_k \alpha_k^{1/2}$  is enriched at the surface. Here  $\beta_k$  is a parameter that is directly linked to the polymer flexibility and it is proportional to the square of its radius of gyration, while  $\alpha_k$  is the interaction density of species  $k$  with the poor solvent. If the two polymers have a similar energy density:

$$\alpha_A \simeq \alpha_B \equiv \alpha \rightarrow \gamma_A - \gamma_B \sim \sqrt{\alpha}(\beta_A - \beta_B) \sim \frac{\beta_k}{\xi_k}(\beta_A - \beta_B),$$

then, entropy dominates and the surface is enriched with the more flexible polymer species (smaller  $\beta_k$ ). When the two polymers have a similar flexibility instead:

$$\beta_A \simeq \beta_B \equiv \beta \xrightarrow{\text{regular solution theory}} \alpha_k \sim (\delta_k - \delta_{solv})^2 \delta_{solv} \ll \delta_k$$

$$\gamma_A - \gamma_B \sim \beta_A \delta_A - \beta_B \delta_B \approx \beta(\delta_A - \delta_B),$$

Now, enthalpy dominates and the surface is enriched with the polymer species having the smaller cohesive energy (smaller  $\delta_k$ ).

In general, polymer segregation can result from small differences between the components of the blend. For example, in blends of hydrocarbon polymers containing deuterated and hydrogenated components, the weaker component (deuterated) usually segregates at the surface [43, 44]. Large segregation effects are also observed in blends of polyolefins [19, 45, 46, 47] in the short-chain regime. In this particular case the best example is a blend of polyethylethylene and polyethylene where the former segregates better when in contact to different types of surfaces [19, 45]. It is also obvious that segregation is energetic in nature, meaning that the component with weaker van der Waals interactions dominates at the surface, while the one able to have more intermolecular contacts stays in the *bulk* [48].

It has also been reported that it is possible to have an entropic segregation from polymer blends [42, 49, 50, 51, 52, 53]. There are two types of entropy in a system containing polymers with different architecture: conformational entropy and packing entropy [54]. As a single polymer molecule comes closer to the surface it loses conformational entropy, so that the polymer density near the surface will be depleted. In contrast, in denser systems, packing of molecules close to the surface causes an increase in the available volume in the rest of the fluid, consequently the overall entropy of the fluid increases. In homopolymers the conformational entropic effect is dominant at low densities (dilute solutions) and the packing entropic effect is dominant at liquid-like densities. In a polymer blend containing both linear and branched polymers where the volume occupied by both species is the same, linear species get closer to each other at the surface than the branched ones because they are more flexible. On the other hand, branched polymers being smaller molecules

lose less conformational entropy. Therefore, the entropic force driving segregation will depend on which of the two entropic effects is the dominant one. In general, packing entropic effects dominate when the blend components have minor structural differences, such as different stiffness, or when one of them has short branches. In these cases, the linear component should segregate to the surface because of entropic considerations [42, 50, 51, 52] but the situation becomes unclear for the case where the structural differences are large, such as when for example linear polymers are mixed with star or comb polymers. For the latter, self-consistent field theory [42, 53] predicts the existence of a net entropic attraction to the surface for chain-ends, and a net repulsion for junction points: consequently, comb and star polymers should segregate to the surface.

Surface segregation of polymer blends in confined geometry is frequently studied by using molecular dynamics computer simulation as applied to the bead-spring model [26, 55]. In these models, the dynamics of the polymer chain is obtained by summing the external and the frictional drag forces acting on the beads. The Brownian force is also used to represent the frequent random collisions between the bead and the implicit solvent molecules at a temperature  $T$ .

## 2.2 Computational models for conducting polymer blends

In recent literature, coarse-grained (CG) models based on the knowledge gained from atomistic (all-atom) molecular dynamics simulations of small-sized systems have been constructed with the aim to elucidate the morphology of the photoactive layer [5, 56, 57]. In these approaches [56, 57], several atoms are grouped together by considering them as single “superatoms”. For instance, Huang *et al* [56] developed a CG model of P3HT- $C_{60}$  mixtures, in which the P3HT monomers are represented using tree sites: the center-of-mass of the thiophene ring, the center-of-mass of the carbon atoms of the first three side-chain methyl groups, and the center-of-mass of the carbons of the last three side-chain methyl groups (three beads per monomer). The coarse-grained model of  $C_{60}$  consisted of a single bead located on its center-of-mass. The chemical structures of P3HT and  $C_{60}$  within the coarse-grained scheme are illustrated in Figure 2.1.

This coarse-grained model [56] was parameterised starting from an accurate atomistic model of P3HT at temperatures high enough ( $\approx 600K$ ), so that the system was in a fluid state in order to avoid solidification of  $C_{60}$  molecules at low temperature. The interactions between the CG sites were optimised to reproduce the atomistic structure of the system: radial distribution functions of nonbonded sites of P3HT- $C_{60}$  particles, bond, angle, and dihedral distributions of P3HT; using the iterative Boltzmann inversion method. Atomistic systems studied at ambient pressure but still at high temperature consisted of P3HT 12-mers, and were considered at the weight ratios reported in Table 2.1. The coarse-grained interactions of P3HT polymers were optimised in simulations of (pure) 60 P3HT 12-mers at  $T=550K$ . Then, the P3HT- $C_{60}$ , and  $C_{60}$ - $C_{60}$  CG interactions were optimised in simulations of 1.85 : 1 w/w P3HT: $C_{60}$  at the same temperature. The choice of using 12-mers for optimisation was based on previous literature [58, 59], showing that oligomers of this

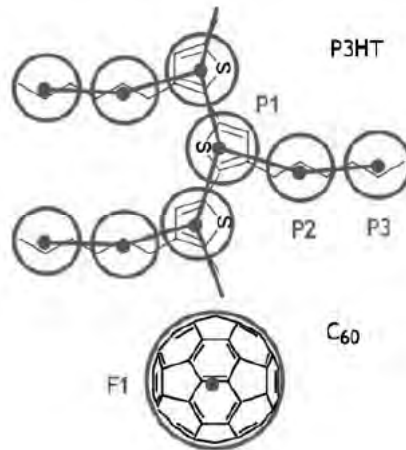


Figure 2.1: Chemical structures of P3HT and  $C_{60}$  with CG sites depicted and labeled [56].

Table 2.1: Temperatures and Mixture Ratios of Atomistic Systems  
(pressure = 1 atm in all cases) [56]

P3HT:PCBM			
$n(3HT12)/nC_{60}$	$P3HT : C_{60}(W/W)$	equiv <sup>b</sup> (W/W)	temperature (K)
60/0	1.00:0	1.0:0	500, 550, 650
50/55	2.52:1	2.0:1	500
48/72	1.85:1	1.5:1	550, 650
42/92	1.27:1	1.0:1	550, 650

<sup>a</sup>Regioregular P3HT (rr-P3HT) was used in all cases.

<sup>b</sup>P3HT:PCBM mixture with same mole ratio as P3HT: $C_{60}$  mixture

length behave sufficiently like long-chain polymers to be used in the CG procedure. The coarse-grained model was simulated by using 768 P3HT 48-mers and 4608  $C_{60}$  molecules in a cubic box of volume  $\approx 25 \text{ nm}^3$ , corresponding to 1.85 : 1 w/w P3HT: $C_{60}$  with approximately 115200 particles. The system was equilibrated for 1 ns at 550K, and then cooled down to 490K (at constant rate) over a period of 10 ns. The simulation took approximately 24h on 256 2.3 GHz AMD Opteron processors. The aim of that study was to develop a CG model that could be used to examine the structural and dynamic evolution of the BHJ microstructure of polymer and fullerene mixtures for a system approaching the device scale. In a subsequent study [57], the same CG model was used, and simulations of P3HT: $C_{60}$  mixtures with 12, 24, 48, and 96-mers were performed. Among the considered properties, the authors studied the radius of gyration of P3HT polymers, and their shape anisotropy (computer simulations of  $\approx 100,000$  CG sites in a cubic simulation box of volume  $\approx 25 \text{ nm}^3$ ). They also studied the clustering of the system by visual means only (since the simulation time-scale is too short to study the complete process of phase separation) over a time scale of a

few tens of nanoseconds.

Lee *et al* [5] developed an even more simplified CG model for the P3HT and PCBM blend. They replaced a full monomer chain of P3HT with a single site (bead) at the center-of-mass of the monomer, and the PCBM molecule with a single bead. The Chemical structures of P3HT and PCBM with the CG sites scheme are illustrated in Figure 2.2. Apparently, the atomistic model adopted in order to optimise the CG interactions was less refined with respect to the one used by Huang *et al*, and based on the DREIDING force field. Also in this case, the distributions of the CG particle bond length, bond angle, planar angle, and the radial distribution functions for non-bonded beads were used within the Boltzmann inversion procedure to obtain the CG interactions. In order to retrieve atomistic details from configurations generated from CGMD simulation, a smaller system with a thinner simulation cell along the  $z$ -axis was used. The reason is related to the fact that with a thinner simulation cell along the  $z$ -axis, it was possible to use reverse-mapping (from the CG model back to the atomistic one) to visualize the nanoscale structural evolution of the blend with a atomistic detail. They studied a bulk system of  $\approx 22238$  CG sites estimated assuming that the number density of the system is the same as in the article by Huang *et al* [57] which correspond to 1870 P3HT 10-mers and 3536 PCBM CG molecules (1:1 w/w P3HT:PCBM) in a cubic simulation box of volume  $\approx 33.16 \times 33.16 \times 3.16 \text{ nm}^3$ . The same authors also performed CG simulations for a larger system of 14532 P3HT 10-mers and 27480 PCBM CG molecules in a cubic volume of  $\approx 30 \times 30 \times 30 \text{ nm}^3$ , and a spatial-discretisation approach was adopted subsequently in order to study the mesoscopic properties of the P3HT:PCBM blend [5]. In this scheme, the entire simulation cell was divided into equal-sized cubes having dimensions close to those of PCBM particles. The following quantity was defined to know whether a cube belonged to either the P3HT or PCBM domain:

$$\lambda = \left( \frac{N_{P3HT}}{N_{PCBM}} \right) \left( \frac{\sigma_{P3HT}}{\sigma_{PCBM}} \right)^3 \quad (2.1)$$

where  $N_{P3HT}$  and  $N_{PCBM}$  are the numbers of CG molecules of P3HT and PCBM molecules respectively, and  $\sigma_{P3HT}$  and  $\sigma_{PCBM}$  are the CG particle sizes of P3HT monomers and PCBM molecules respectively. With such a spatial-discretisation scheme, three morphological quantities that influence the performance of BHJ cells were estimated, namely the average domain size, the interface-to-volume ratio, and the percolation ratio of the blend film. They were also able to reproduce some relevant structural quantities, such as radial distribution function of P3HT monomers, PCBM monomers, and the mixture of the two monomers. Thus, CGMD simulations can allow domains the size of the diffusion length to be studied while retaining significant information about the molecular structure, thereby providing useful insights into understanding the morphology of the BHJ [56]. Obviously, one of the limitations of CG simulations is related to the possibility to reliably estimate dynamical quantities, e.g. diffusion, since the dynamics of CGMD simulations is obviously faster as compared with the one of all-atom molecular dynamics.

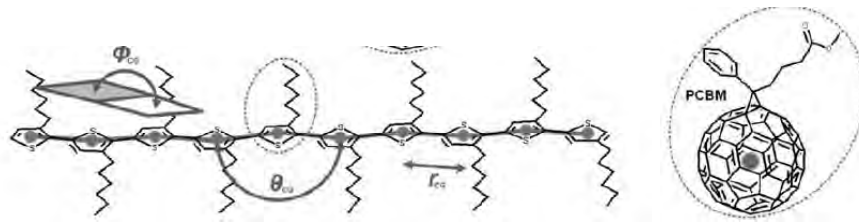


Figure 2.2: Chemical structures of P3HT and PCBM with CG sites depicted. The intramolecular degrees of freedom between the CG particles of P3HT monomers are highlighted [5].

## 2.3 Experimental approach

The experimental approach is intended to provide insight about the relationship between the arrangement of the constituent molecules in the medium and the performance of organic solar cell. Organic solar cells are fabricated based on organic semiconductor molecules or conjugated polymers. We employed poly (3-hexythyophene) (P3HT) and [6-6] phenyl-C61-butuyric acid methyl ester (PCBM) to create the photoactive medium to harvest photons during illumination. These molecules often known as p-type and n-type organic semiconductors, respectively. In terms of device architecture, the most efficient type of device architecture to date is the bulk heterojunction design in which both p-type and n-type molecules are blended in an organic solvent. The photoactive medium is then formed from the solution of the blend by way of spin coating, doctor blending etc. A number of physical processes take place in the conversion of solar radiation into electricity by OTFSC devices. These are photon absorption, exciton generation, exciton dissociation into free carriers and charge transport to the electrodes. The excitons are separated into free holes and electrons by the electric field produced at the interfaces. Due to the limitation of the exciton diffusion length of organic materials in the order of (5-10nm), only absorption of light within a very thin layer around the interfaces contributes to the photovoltaic effect. This in turn influences the performance of the device, since there is no possibility of such thin layer absorbing all the light. The BHJ design introduced, by Yu *et al.* [60] in 1995, constitutes molecular level donor/acceptor interfaces which are spread over the medium, enhanced significantly the efficiency of exciton dissociation. This device architecture become popular in organic solar cell fabrication and has been extensively used since its introduction. Another important factor in the preparation of OTFSC devices is the solvent used in wet processing. One such study was done by Shaheen *et al.* [61] who reached an important discovery in terms of power conversion efficiency and demonstrated that the solvent used has a profound impact on the morphology and performance of BHJ solar cells.

### 2.3.1 Optical properties of organic photovoltaic materials

It is well known that, the working principle of organic photovoltaic devices can be described in seven important processes namely; in-coupling of photon, photon absorption, exciton formation,

exciton migration, exciton dissociation, charge transport, and charge collection at the electrodes. In-coupling of photon and photon absorption constitute optical mechanisms, while all the rest constitute electrical mechanisms of the device. The optical mechanism plays an important role on the performance of the device since incident photons and absorbed photons are the basic factors needed. Base on this, Park *et al.* [4] reported that it is possible to attain 100% internal quantum efficiency (IQE) of organic bulk heterojunction solar cells. Therefore, the external quantum efficiency (EQE) can be described as;

$$EQE \approx IQE \frac{\text{number of absorbed photons in active layer}}{\text{number of incoming photons}}.$$

Tessema [62] in his work measured the optical absorption spectra of APFO-Green 6:PCBM blend and found out that the EQE is about 58% over the wavelength range 350 – 450nm. Further in their research, base on ternary molecules blend distinct optical band of the donors (P3HT and PTB7) were observed. The optical absorption band of P3HT fell in the range 400 – 650nm, whereas that of PTB7 was in the range 400 – 750nm. It was further noted that the PTB7 has an additional optical absorption spectral range from 650 – 750nm which could contribute to an enhancement of photon harvesting in medium, therefore improve the device performance [63].

### 2.3.2 Device parameters of a solar cell

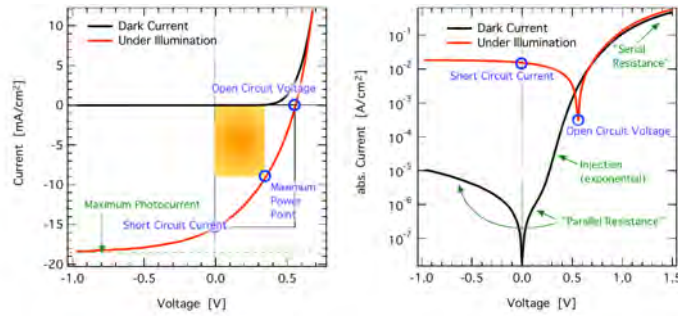


Figure 2.3: Schematic current-voltage characteristics of bulk heterojunction solar cells in (a) linear and (b) semilogarithmic representation [64].

J-V characterization is the most common way to illustrate the performance and electrical properties of solar cells. This technique measures current as a function of voltage in both the dark and light. Under dark conditions, the J-V curve passes through the origin with no potential, no current flows. But, when the device is exposed to light, the current flows in the opposite direction to the injected currents. Due to this reason, the J-V curve shifts downward as illustrate in fig 2.3 and therefore, the performance of an organic solar cell (OSC) can be evaluated by three important parameters, namely short-circuit current density ( $J_{SC}$ ), open-circuit voltage ( $V_{OC}$ ) and fill factor (FF). A short-circuit current density is the current that flows through an illuminated solar cell when the voltage across the solar cell is zero, i.e. when the electrodes of the device are directly

connected together. It is the largest current that the device is able to produce. Meanwhile, the open-circuit voltage is the largest possible voltage across the cell in sunlight when no current is flowing. In the four quadrant of the curve, the largest power output is the product of current and voltage ( $P_{max} = J_{max}V_{max}$ ), then the power conversion efficiency (PCE) can be evaluated as:

$$\eta = \frac{P_{out}}{P_{in}} = \frac{J_{max}V_{max}}{P_{in}} = \frac{J_{sc}V_{oc}FF}{P_{in}} \quad (2.2)$$

where  $P_{in}$  is the light power incident on the device generated when solar simulators are used, and the key quantity used to measure OSC performance known as FF is given by:

$$FF = \frac{J_{max}V_{max}}{J_{sc}V_{oc}}. \quad (2.3)$$

Among all the physical parameters listed above, which ones affected the performance of the organic solar cell? This issue has been addressed by several publications which state that,  $J_{sc}$  can be affected by light absorption, recombination, electrodes charge collection and so on;  $V_{oc}$  can be affected by the energy level of the materials, recombination, current leaking and so on and so fort; while the FF can be affected by internal resistance of the cell, electrodes charge collection, recombination and so fort. In order to understand the electrical properties of OTFSC and improve their parameters listed above, the characteristics of solar cells have been interpreted by examining the equivalent circuit model of solar cells.

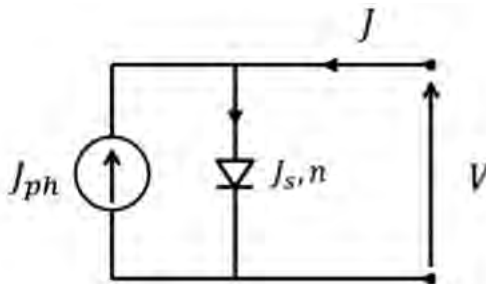


Figure 2.4: Equivalent circuit diagram of ideal solar cells [65].

### 2.3.3 Equivalent electrical circuit models for OTFSC devices

One approach to aid a better understanding of the electrical behaviour of OTFSCs, is by accurately modelling them with an equivalent electrical circuit. The most common equivalent electrical circuits used to model OTFSCs are the one-diode model (ODM) or two-diode model (TDM) [66, 67, 68, 69]. These models have been deduced from inorganic p-n junction solar cells where they worked perfectly in explaining inorganic photovoltaic cells electrical behaviour as a p-n junction [70]. Under illumination, a photovoltaic solar cell can be represented by an equivalent circuit of an ideal solar cell, based on a single-diode model, depicted in Fig 2.4. The output current from the device can be

described by an equation

$$J = J_s \left[ \exp\left(\frac{qV}{k_B T}\right) - 1 \right] - J_{ph}, \quad (2.4)$$

where  $J_s$  is the reverse saturation current density of the diode in the dark,  $q$  is the elementary charge,  $V$  is the applied voltage,  $k_B$  is the Boltzmann constant,  $T$  the temperature and  $J_{ph}$  the photo-generated current density. Under dark conditions, the cell can be thought of as a current source where  $J_{ph}$  is a reverse current proportional to the incident light in parallel with a diode which delivers the J-V relation given by [66]

$$J = J_s \left[ \exp\left(\frac{qV}{k_B T}\right) - 1 \right]. \quad (2.5)$$

Nevertheless, in a practical solar cells, there exist some unavoidable factors that Eq (2.4) does

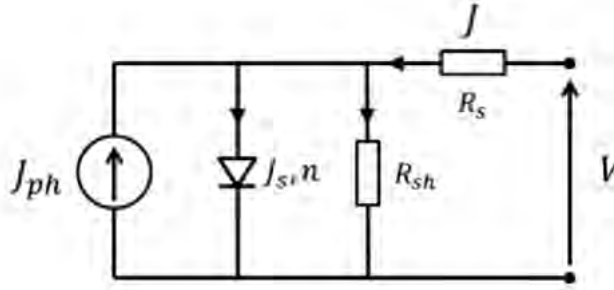


Figure 2.5: Equivalent circuit diagram of real solar cells [65].

not take into account, which affect the external behaviour of the cell. Therefore, two of this extrinsic factors are added to the equivalent model, namely series resistance and shunt resistance as shown in Fig 2.5. In these equivalent circuit models, the series resistance ( $R_s$ ) correspond to the contact resistances and the ohmic losses between the active layer and electrodes. The shunt resistance ( $R_{sh}$ ) is due to the loss of current through any type of charge recombination and trapping inside the photovoltaic cells. Once  $R_s$  and  $R_{sh}$  are taking into consideration, the equation for the equivalent circuit under illumination can be written:

$$J = J_s \left[ \exp\left(\frac{e(V - JR_s)}{nk_B T}\right) - 1 \right] + \frac{V - JR_s}{R_{sh}} - J_{ph}, \quad (2.6)$$

### 2.3.4 Effect of morphology on the performance of the cell

The performance of OTFSC cell has been found to be very much dependant on the nonomorphology of the photoactive medium of the devices [71, 72]. The preferred morphology in bulk heterojunction has to present a bicontinuous interpenetration network of donor and acceptor domains in the range of the exciton dissociation length, around 10nm [73, 74]. This would allows excitons to diffuse into the donor-acceptor interface and thus achieves efficient charge dissociation. In addition, holes and electrons must travel to the positive and negative electrodes through donor and acceptor networks respectively, after charge separation at the interface. In order to be able

to understand the Nanomorphology of the BHJ films of our devices; we employed Zeiss EVO LS 15 ultra plus FESEM (Field Emission Scanning Electron Microscopy) fitted with Oxford EDAX (Energy Dispersive Analysis of X-ray) detector (INCA Point ID software for quant optimization). The information derived from the surface scanning of the films will provide us with information about the distribution the constituents of the film as well as the formation of different artifacts on the surface.

Many researchers have extensively employed these techniques to characterize the morphology of the active layer of OTFSC. Martens *et al.* employed TEM to investigate nanoscale morphology of the MDMO-PPV:PCBM active layer and observed an enhancement of the domain size of the PCBM-rich phase with the increase PCBM concentration [75]. Hoppe *et al.* used a high-resolution SEM to investigate the morphology of the cross sections of toluene and of MDMO-PPV:PCBM blends mixed with chlorobenzene [76]. They found out that, from the sample prepared with toluene processing solvent, large PCBM aggregates at the surface and consequently reduced the charge carrier generation efficiency. The other sample prepared with chlorobenzene processing solvent shows reduced PCBM clusters. This particular techniques was used in the study to understanding the relationship between the nanomorphology and the device performance.

The use of processing solvent additives are known for improving device performance because of the role they played in reorganizing the arrangement of molecules in the photoactive layer of OTFSC devices. The effect of additive solvents can be observed even on the surface morphology of the films which is strongly correlated with device performance. In this thesis, we have investigated the effect of three different additive solvents such as additive 1,8-diiodooctane (DIO), 1-chloronaphthalene (CN) and dimethyl sulfoxide (DMSO) on the morphology of P3HT:PCBM blend, in the preparation of P3HT:PCBM based devices.

## Chapter 3

# Tuning the Computational approach to the Model

### 3.1 Introduction

This chapter discusses the main computational method, molecular dynamics (MD) Simulation, that we used to study our model for a polymer blend. The model that we adopted is a very popular one in polymer physics, and was developed originally by Grest and Kremer [25, 26]. The need of this model arises from our attempt to simulate melt densities. At these densities the motion of polymers is subject to tight constraints determined by their topology. The main issue is that since monomer beads are connected to other ones along the polymer chain, "entangled" polymer chains have some peculiar types of motion, which are not detected in atomic or molecular systems. The existence of this characteristic dynamics of polymer blends requests we use a combination of Brownian and molecular dynamics, and it makes the bead-spring model by Grest and Kremer a fundamental one in computational polymer physics, since it can be mapped on many real polymer melts considered in experiments. A number of properties are accessible to this model, including fluctuations, mechanical properties, as well as the kinetics of reactions involving degradation and polymerisation of monomers, respectively [77]. This model is then essential in our research to understand how the packing constraints imposed by the different topology of the two polymer species determine the adsorption and structural properties of the system at the interface. To this aim, we will consider a basic model of a polymer blend, where the two main topologies also found in organic polymer blends relevant to photovoltaic applications are considered, namely chains with an elongated structure (P3HT) and a closed or compact one (PCBM). This chapter continues with a brief summary of our computational model and the simulation methodology. Then we will discuss the first preliminary attempts on a model that was slightly biased (for a reason that we will explain later we considered here a bead-spring model in the presence of a wall potential) in

order to understand the equilibration. Finally, we will draw some conclusions which will be useful to introduce the main chapter following this one, where the most important results of this research study will be presented and discussed in a thorough and exhaustive manner.

## 3.2 Model and Methods

The structure of linear-cyclic polymer blend at interface has been analysed by performing Molecular Dynamics (MD) simulations of bead-spring models [26]. Cyclic and linear polymers are modeled as a number of contiguous monomers of equal mass  $m$  connected to form either an open or closed chain (loop) via springs. While the beads operate as interaction points with the solvent, the springs symbolise entropic effects due to the internal degrees of freedom which have been lost during the process of coarse-graining. In the bead-spring model, the dynamics of the polymer chain is obtained by summing the external forces acting on the beads according to the following equation,

$$F = F_f + F_B + F_E \quad (3.1)$$

where  $F_f$ ,  $F_B$ ,  $F_E$  are the frictional drag force (Stokes's drag), the Brownian force and the effective spring force, respectively. The frictional drag force acting on the bead which is given by;

$$F_f = -\left(\frac{m}{\zeta}\right)V \quad (3.2)$$

where  $m$  is the mass of the bead,  $\zeta = 0.5$  is the damping factor and  $V$  is the velocity of the bead. The Brownian force is used to represent the frequent random collisions between the bead and the implicit solvent molecules at a temperature  $T$ . As derived from the fluctuation-dissipation theorem, its magnitude is chosen such that;

$$F_B = \sqrt{\frac{k_B T m}{\Delta t \zeta}}, \quad (3.3)$$

where  $k_B$  is the Boltzmann's constant,  $T$  the temperature,  $m$  the mass of the bead,  $\Delta t$  the time-step size, and  $\zeta$  is the damping factor.

The frictional drag and the Brownian force are used to mimic the presence of solvent in terms of viscous damping and of the frequent random collisions between the bead and the solvent molecules at a temperature  $T$ . The physical quantities used during MD simulations are not reported directly in the international system of units (SI). Their numerical values would be either very small or very large and thus can lead to overflow or underflow as a result of floating-point operations. It is therefore advisable to represent all quantities in units such that their numerical values are number of the order of unity. The Lennard-Jones parameters  $\sigma$  and  $\epsilon$  used in simulations are the most appropriate units of length and energy. The time unit is  $\tau = \sigma\sqrt{m/\epsilon}$ . Temperature, the friction coefficient, and the integration time step were set respectively, to  $\epsilon/k_B$ ,  $2\tau$ , and  $0.01\tau^{-1}$ .

The effective spring force used to model our spring, is the nonlinear spring force, namely the finite extensible nonlinear elastic (FENE) potential [26]. The beads interact with a purely repulsive

Lennard-Jones (LJ) potential to account for the excluded volume interaction, and the attractive FENE potential to keep the consecutive beads along the chain bonded together. The combination of two terms is used to define the total potential between pairs of bonded beads which is given by [26]

$$E(r) = \begin{cases} -\frac{1}{2}Kr_0^2\ln\left[1 - \left(\frac{r}{r_0}\right)^2\right] + 4\epsilon\left[\left(\frac{\sigma}{r}\right)^{12} - \left(\frac{\sigma}{r}\right)^6 + \frac{1}{4}\right], & r \leq r_c \\ -\frac{1}{2}Kr_0^2\ln\left[1 - \left(\frac{r}{r_0}\right)^2\right] & r > r_c \end{cases}$$

where  $K = 30\epsilon/\sigma^2$ ,  $\sigma$  and  $\epsilon$  are LJ parameters,  $r_0 = 1.5\sigma$  the maximum distance of the bond, and  $r$  is the distance between monomers. The parameters  $r_0$  and  $k$  have to be chosen such that the possibility of bond crossing becomes so unlikely that it never occurs. The Lennard-Jones term is shifted at  $2^{1/6}\sigma$  so that the energy at the minimum is zero. As it can be seen in Figure 3.1, these two potentials restrict the bond length between adjacent beads (monomers) to be in a range of  $0.752\sigma \leq r < 1.452\sigma$ , which was estimated by considering the extremely high value for the thermal energy equal to  $100\epsilon$ . The Lennard-Jones potential restricts the lower limit and FENE potential restricts the upper limit.

The angle interaction between consecutive triplets of beads ( $\theta$ ) is determined by the cosine angle potential,

$$E(r) = K[1 + \cos(\theta)]. \quad (3.4)$$

During our simulations, the coefficient  $K$  associated with the angle potential has been taken to be zero, which implies that there were no forces to stabilise any angle between adjacent beads. The interactions between non-bonded beads are modeled by the truncated and shifted LJ potential, such that the potential vanishes at the cut-off distance  $r_{c,nb} = 2.5\sigma$ , so that the potential vanishes at  $r_{c,nb}$ :

$$E(r) = \begin{cases} 4\epsilon\left[\left(\frac{\sigma}{r}\right)^{12} - \left(\frac{\sigma}{r}\right)^6 + \frac{1}{4}\right], & r \leq r_{c,nb} \\ 0 & r > r_{c,nb} \end{cases}$$

where  $r$  is the distance between the two beads,  $\sigma$  the diameter of the bead,  $\epsilon$  the interaction strength, and  $r_{c,nb} = 2.5\sigma$  is the cut-off distance. The reason for introducing a cut-off distance  $r_{c,nb}$  is to avoid computing the energy of non-bonded beads so distant from each other that the pair interaction energy is close to zero, and provides a negligible contribution to the equilibrium properties of the system. Truncation makes the energy jumps whenever a particle pair crosses the cut-off distance. A huge number of such events is likely to spoil energy conservation in a simulation. To prevent this type of problem, a constant energy term ( $1/4$ ) is added to each pairwise interaction in order to make it vanish at the cut-off distance, so that the underlying pair forces are unchanged and no bias is introduced for the trajectories of the particles.

A pseudo-Monte Carlo simulation was used to prepare the initial configurations for the Brownian dynamics simulations. Firstly, an open or closed chain of ideal-gas particles was generated, and the randomly inserted inside the simulation box. The distance between subsequent ideal-gas

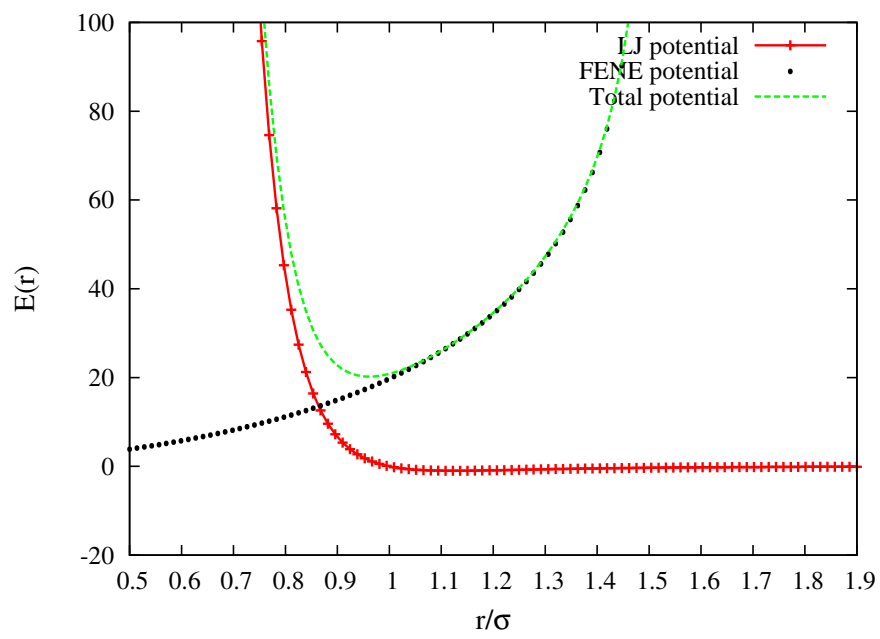


Figure 3.1: FENE and Lennard-Jones Potentials.

particles has been initially taken as the minimum of the FENE potential. In order to generate the initial conformation of a linear polymer as an open chain of ideal-gas particles we proceeded as follows:

1. Starting from an initial point in space, we selected a random direction in terms of a unit vector, and we allocated a ghost particle to a distance equal to the minimum of the FENE potential.
2. We allocated the subsequent particle by using as a starting point the new ghost particle allocated in 1, and we iterated the procedure reported in 1 again. We stopped when we reached a number of ghost particles equal to the degree of polymerization.

In order to generate an initial conformation of a cyclic polymer as a closed chain (loop) of ideal-gas particles, we proceeded as follows:

1. Starting from an initial point in space, we selected a random direction in terms of a unit vector, and we allocate a ghost particle to a distance equal to the minimum of the FENE potential ( $\Psi$ ).
2. Starting from the allocated ghost particle, we allocated another particle by iterating just once the procedure reported in item 1.
3. Starting from the ghost particle allocated in item 2, we allocated the subsequent ghost particle by choosing the direction along which allocating the next particle according to the probability reported below:
  - A unit vector with components given by uniformly-generated random numbers in the interval  $[0,1]$  with probability  $p = 1 - \frac{N}{N_p}$ , where  $N$  is the total number of particles of the growing cyclic polymer and  $N_p$  is the degree of polymerization.
  - With probability  $p = \frac{N}{N_p}$ , we generate a unit vector with direction parameters taken from the line connecting the last particle of the growing cyclic polymer with the first one. For this case, special care must be taken because there are two events which could possibly spoil the algorithm. Let us analyze them in detail:
    1. We come closer to the initial particle before reaching the degree of polymerization of the cyclic polymer. In this case, the algorithm will always add the subsequent particle by placing it at a distance  $\Psi=dFENE$  along a random unit vector (see procedure described before for the random direction).
    2. We do not come close enough to the initial particle (i.e. it is distant from the initial particle more than  $2\Psi$ ). However this event is very unlikely because we continuously bias the choice of the unit vector so that the probability that we place the next particle along the direction

connecting it to the initial one, increases with the total number of particles of the growing cyclic polymer.

3. When particle  $N_b - 1$  is added to the growing polymer, we need to place the subsequent one so that it is located at a distance equal to  $\Psi$  from both the initial particle and particle number  $N_b - 1$ . In this case, we close the loop by adding particle number  $N_b$  with coordinates given analytically in terms of the coordinates of the first particle, particle number  $N_b - 1$ , and the parameters (a,b,c,d) of the plane passing through the first particle, particle number  $N_b - 1$ , and the center-of-mass of the cyclic polymer. Then, since we get two possible solutions to this problem [78], we select the one that places particle number more far apart from the center-of-mass of the cyclic polymer.

Periodic boundary conditions are applied in the  $x$ - and  $y$ -directions, and the simulation box is sealed on its low- $z$  edge with a flat wall at a fixed position  $z^*$ . The wall interacts with polymers by generating a force on the bead in the direction perpendicular to the wall. It is important to note that there is just a single wall along the  $z$ -direction and particles are not confined towards the upper edge of the box. However, we shall verify that they will never explore that part of the box on the time-scale of our simulations. Throughout our preliminary calculations, the integrated 9-3 LJ potential was used to simulate wall-bead interactions. The wall potential energy is given as,

$$E_{LJ}(z) = \epsilon \left[ \frac{2}{15} \left( \frac{\sigma}{z} \right)^9 - \left( \frac{\sigma}{z} \right)^3 \right] \quad z < z_c \quad (3.5)$$

where  $z$  is the distance from the bead to the wall, and  $z_c = 2.2\sigma$  is the cut-off distance at which the bead and wall no longer interact. The energy of the wall potential is shifted so that the wall-bead interaction energy is zero at the cut-off distance. We would like to point out that we used a fluid-wall potential only in our preliminary calculations with the aim to study the equilibration properties of the system. In our preliminary study, we examined static and dynamical properties of pure linear, pure cyclic, and linear-cyclic mixtures.

In summary, we used the Langevin thermostat to model the interaction of the polymer beads with implicit solvent, and the microcanonical ensemble to perform constant NVE integration to update positions and velocities for particles in the system. Practically, the simulation studies as related to our initial test of the system were carried out according to the following steps; firstly, the system was run in the NPT ensemble with full periodic boundary conditions (along the  $x$ -,  $y$ - and  $z$ -directions) at the pressure of 1 atm. The systems were further equilibrated in the NVT ensemble for some time at the desired temperature. Once equilibrium in the NVT ensemble was established, films with surfaces in the  $xy$ -plane were created by removing the periodicity along the  $z$ -direction. To ensure that periodic images of the resulting films did not interact in the  $z$ -direction, polymer molecules were rebuilt and the simulation box length in the  $z$ -direction was significantly increased. The simulations of these films were then run again in the NVT ensemble. All simulations were performed using the Large-scale Atomic/Molecular Massively Parallel Simulator (LAMMPS)

molecular dynamics package [79] on a Dell Precision T7600 workstation (equipped with two 8-core Intel E5-2687 3.1 GHz processors) for the linear polymers, Dell PowerEdge R810 server (four 8-core Intel processors Xeon-E7-8837 2.67 GHz) for the cyclic polymers, and the High Performance computing (HPC) cluster (www.chpc.ac.za) for the linear-cyclic polymers blend. All the final simulations (as related to the last equilibration step) were performed for  $10 \times 10^7 \Delta t$ , which was deemed long enough for the polymer chains to reach their equilibrium structure. Some physical quantities and parameters of interest of our MD simulations are given in Table 3.1 in LJ units.

During the simulations, we monitored the pressure and temperature equilibration of the system, see Figs. 3.2, 3.7, 3.12. Structural properties of each polymer type in the blend have been investigated by describing the position of a single polymer using its center-of-mass defined as

$$\vec{r}_{com} = \frac{\sum_{i=1}^{N_b} \vec{r}_i}{\sum_{i=1}^{N_b} m_i}, \quad (3.6)$$

where  $m_i$  is the mass of atom  $i$ ,  $N_b$  is the number of monomers in a single polymer chain, and  $\vec{r}_i = [x_i, y_i, z_i]$  is the atom position. Changing the notation  $\vec{r}_{com}$  to  $\bar{z}_i$  in Eq. (3.6) gives the center-of-mass along the  $z$ -axis,  $\bar{z}_{com}$ , which is useful measure of the position of the polymer relative to liquid/vacuum interface. The position of the center-of-mass can be used afterwards, to determine the effective size of the single polymer which is described using its square radius of gyration defined as:

$$R_g^2 = \frac{1}{N_b} \sum_i (\vec{r}_i - \vec{r}_{com})^2, \quad (3.7)$$

By averaging out, also as a function of time, the radii of gyration of all the polymers in the system, we calculated the average radius of gyration  $\overline{R_g}$  of the total number of polymers. Then, sometimes  $\overline{R_g}$  was used as bin size of the histogram and the  $z$ -direction was subdivided in  $N_{tot}$  bins of size  $\overline{R_g}$ . Because of the boundary conditions along the  $x$ - and  $y$ -directions, we had to perform this calculation carefully in order to take into account the broken molecules and in case re-build them again.

The analysis of the systems was performed by looking at the number density of the center-of-masses (coms) of polymers as a function of distance  $z$  from the wall. The histogram was built by counting the number of coms in each bin, and by calculating the ratio  $T(z)$  of  $\rho(z)$ , which is the number density of polymers coms at a distance  $z$  from the wall and  $\rho_0$ , which is the bulk density of the system:

$$T(z) = \frac{\rho(z)}{\rho_0}. \quad (3.8)$$

In addition to the adsorption of polymer chains, we examined the magnitude of folding of different polymers by building an histogram of the radii of gyration. The histogram was built by counting the number of polymers coms with a radius of gyration in a given interval (bin), the bin size being calculated by arbitrarily dividing the overall range of radii of gyration in twenty bins. Then, by

evaluating the number of polymers coms having a radius of gyration in that bin, we could show the polydispersivity in the radius of gyration for the whole system as the percentage of polymers in each bin.

Tables 3.2, 3.3, 3.4, 3.5 provide the average radii of gyration and the variance of linear, cyclic and linear-cyclic polymers at different distances from the wall and inside an interval (bin) coincident with the average radius of gyration of different types of polymers. The purpose of evaluating the average radius of gyration in each bin was twofold: 1) we wanted to understand whether the average size of polymers is affected by the presence of the interface (wall). 2) We also wanted to understand whether the polymers closer to the wall were interacting with it or not. The calculation of the variance of the radius of gyration in each bin was done in order to see whether the distribution of sizes of polymers is affected by the presence of the wall.

The main results of this thesis will be discussed in the next chapter and will concern free-standing polymer mixtures, i.e. the interface will be generated without the presence of a wall-fluid potential. The main reason for considering a wall-fluid potential in these preliminary calculations was to verify the equilibration of the system following the removal of the periodicity along the  $z$ -direction. In fact, the presence of the wall was aimed to allow the adsorption of the equilibrated blend: when the polymer film was observed to move away from the wall despite the attraction to it triggered by the LJ 9-6 potential, we could unambiguously determine the need of extending the equilibration of the system to longer times.

Table 3.1: Some physical quantities and model parameters of interest expressed in LJ units.

Names	Label	Linear	Cyclic	Blend
number of atoms	$N$	75000	75000	100000
number of molecules	$N_m$	1500	1500	2000
box length( $x$ -dir)	$L_x$	49.0000	49.0000	48.8258
box length( $y$ -dir)	$L_y$	49.0000	49.0000	49.2710
box length( $z$ -dir)	$L_z$	163.3410	159.4522	164.7144
number of beads in a chain	$N_b$	50	50	50
bead-bead LJ parameter	$\sigma$	1.0	1.0	1.0
bead-bead LJ parameter	$\epsilon$	1.0	1.0	1.0
reduced temperature ( $T^* = k_B T / \epsilon$ )	$T^*$	1.0	1.0	1.0
time step	$\Delta t$	0.005	0.005	0.005

### 3.3 Linear Polymers

The simulated system consists of linear polymer chains (see Table 3.1 for physical quantities and parameters). It can be seen from Figure 3.2 that the pressure and the temperature reach almost constant values during the simulation after a few MD steps, which provide evidence of both stability of the algorithm of the MD simulations code, and that conditions of thermodynamics equilibrium are reached quite soon. The plot of the attractive 9-3 LJ potential reported in Figure 3.3 is shifted at a distance  $z = 47.67\sigma$  according to Table 3.1. It illustrates that there is a minimum potential energy at a distance  $z \approx 0.8\sigma$  from the wall.

The adsorption properties are evaluated by analysing the MD initial configuration and the final one following an equilibration time  $t = 5 \times 10^7 \Delta t$ . In Figure 3.4, we present the normalized linear polymers coms histogram  $T^{lin}(z)$  as a function of distance  $z$  from the wall for  $t = 0$ . From a distance  $z = 0$  to  $z = 54.9\sigma$  and  $z = 113.4\sigma$  to  $z = 180\sigma$ , there are no particles. Particles start to be present from  $z \approx 54.9\sigma$ , and  $T^{lin}(z)$  quickly rises to reach a maximum of 3.5 times the bulk value ( $3.5\rho_0$ ). Now, we note for the first time (and this problem will persist in all these preliminary tests of the code), that apparently far from the wall-fluid and fluid-empty space interfaces, we achieve a density significantly higher than the *bulk* value  $\rho_0$ . The trivial reason for this happenstance is that we are considering the  $\rho_0 = N_0/V_0$  as the ratio between all the particles in the simulation box divided by its volume  $V$ . However, particles do not occupy the whole box uniformly but they are concentrated beyond the wall at low- $z$  values and before the empty space at high- $z$  values. When performing the calculations in the next chapter we will take this fact into account and rescale the densities accordingly. The plot also shows that linear polymers coms are more concentrated in between  $z = 54.9\sigma$  to  $z = 106.0\sigma$  of the simulation box. At  $t = 5 \times 10^7 \Delta t$ ,  $T^{lin}(z)$  remains zero from  $z = 0$  to  $z = 60.9\sigma$ , and  $z = 100\sigma$  to  $z = 160\sigma$ , then rapidly increases at  $z = 60.9\sigma$  up to 5.5 times the bulk density value ( $5.5\rho_0$ ) of linear polymers. As compared to the initial configuration, linear polymers coms seem going more distant from the wall, but definitely shrinking towards the middle of the box (between  $z = 60.9\sigma$  to  $z = 100\sigma$ ), i.e. notwithstanding there is no wall in the top part of the simulation box, polymers are not moving towards that direction.

Apparently, the wall-bead potential energy is not effectively attracting particles near the wall as shown in the bottom panel of Figure 3.4, in which the range of distances where the wall-bead potential is active is reported as an interval on the  $z$ -axis. This effect is due to the fact that the system was not fully relaxed to its final density after the interruption of the periodic boundary conditions along the  $z$ -direction. To compare the initial and the final configurations results, we calculated the percentage difference of the distribution density described as

$$\Psi = \frac{\rho^{final} - \rho^{initial}}{\rho^{initial}} \times 100 \quad (3.9)$$

where  $\rho^{final}$  and  $\rho^{initial}$  are the number density of polymers coms of final and initial configurations of the system. This calculation was performed in order to determine the level of condensation and

depletion of particles in each bin. Condensation refers to the case where there is an increase in the number of polymers coms with respect to the initial configuration, whereas depletion refers to a decrease. A percentage difference of  $\Psi = -100\%$  corresponds to a full depletion, which is the case where there were no polymers coms in the final configuration bin and a percentage difference of  $\Psi = +100\%$  indicates full condensation where there were no polymers coms in the initial configuration bin. Figure 3.5 provides quantitative evidence of what we anticipated by comparing the top and the bottom panels of Figure 3.4, i.e. most of linear polymers coms tend to be condensed towards the middle of the box and depleted at the edges of the box with respect to the initial configuration. Figure 3.6 shows the percentage distribution of linear polymers having a specific radius of gyration. At  $t = 0$ , the peak has a value of  $\approx 13.5\%$ . At  $t = 5 \times 10^7 \Delta t$ , the value of the peak has decreased to  $\approx 12\%$  indicating that there is an increase of polydispersivity of radius of gyration in the final configuration, which means the distribution of length scales of polymers becomes more uniform (i.e. there are more polymers with effective sizes significantly different from the average radius of gyration in the box). As mentioned in the previous section, we tried to understand the role of the wall in determining the structural properties of the system by calculating the average radius of gyration and the variance of the radius of gyration of linear polymers as a function of the distance from the wall. The results are reported in Table 3.2.

First, we see in Table 3.2 that  $\overline{R}_g^{lin}$  and  $\sigma^{lin}$  seem not to be affected by the distance of polymers from the wall.  $\overline{R}_g^{lin}$  is almost the same for the final configuration as compared to the initial one throughout all the range of distances from the bottom edge of the box. Furthermore, the variance in both configurations is of the order of  $\sigma^{lin} \approx 0.7$ , which tell us how linear polymers sizes are distributed with respect to the average. To verify whether polymers closer to the wall were interacting with it, we estimated the distance of these polymers to the wall for the initial and the final configuration by subtracting their average radius of gyration from the polymers coms position. In the initial configuration, the linear chains coms closer to the wall are in the range between  $z \approx 50.18\sigma$  and  $z \approx 57.34\sigma$  from the bottom edge of the simulation box. If we subtract to these distances the average radius of gyration reported in the first line of Table 3.2, we realise that the average positions of the polymers beads are between  $z \approx 46.52\sigma$  and  $z \approx 53.78\sigma$ . Since the range of distances where the wall potential is active is from  $z = 47.67\sigma$  to  $z = 49.87\sigma$ , it can be argued that in the initial configuration linear polymers were interacting with the wall via the 9-3 LJ potential reported in Figure 3.3. In the final configuration, the linear chains coms closer to the wall are in between  $z \approx 57.35\sigma$  and  $z \approx 64.51\sigma$  from the bottom edge of the simulation box. As it was done before, the average radius of gyration was subtracted from these distances and the average positions of the polymers beads are now between  $z \approx 54.04\sigma$  and  $z \approx 61.20\sigma$ . This implies that in the final configuration, linear polymers closer to the flat wall are not interacting with it. The diffusion of the linear polymers coms into the bulk away from the wall observed previously is then due to polymer-polymer interactions: since the system was not fully equilibrated the latter

bring the polymer beads closer to each other and further decrease the overall density of the blend.

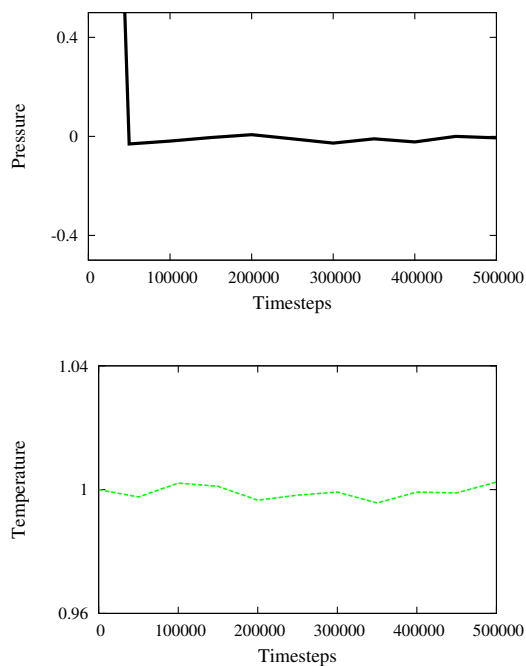


Figure 3.2: Plot of reduced pressure versus time (top) and reduced temperature versus time (bottom) for MD simulations of linear polymers.

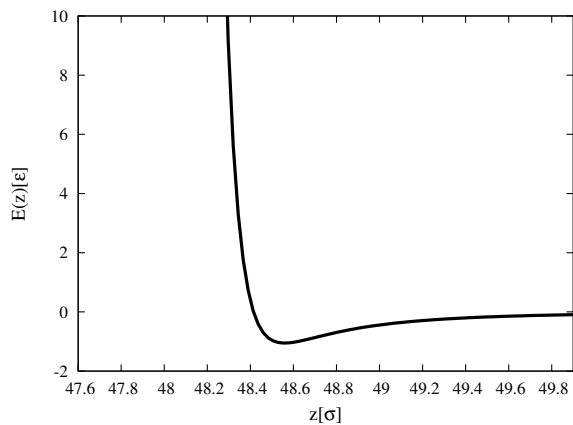


Figure 3.3: Wall 9-3 Lennard-Jones potential shifted at distance  $z = 47.67\sigma$ .

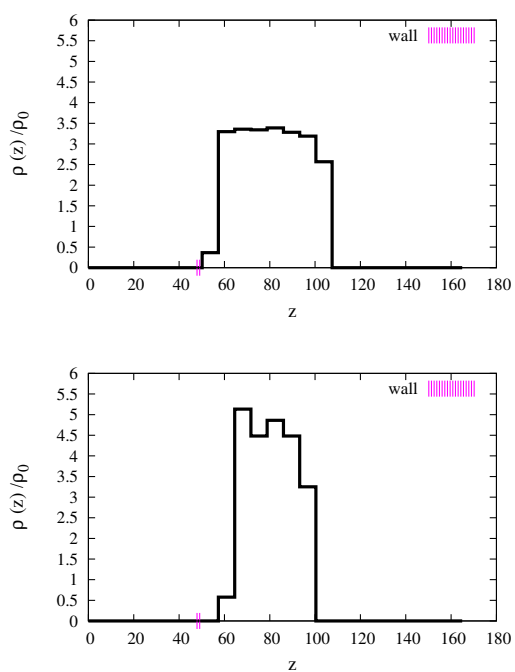


Figure 3.4: Number density distribution,  $\rho(z)/\rho_0$  versus distance  $z$  from the wall of linear polymers coms for  $t = 0$  (top) and  $t = 5 \times 10^7 \Delta t$  (bottom). The interval between vertical bar on the  $z$ -axis is the range of distances where the wall-bead potential is active. For consistency, the same bin size was used for both configurations. This bin size is given by  $2\overline{R}_g = 7.16\sigma$  where  $\overline{R}_g$  is the average radius of gyration.

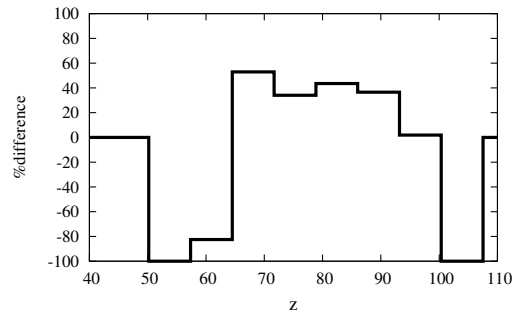


Figure 3.5: Percentage difference of the distribution density as a function of distance  $z$  from the wall for linear polymers.

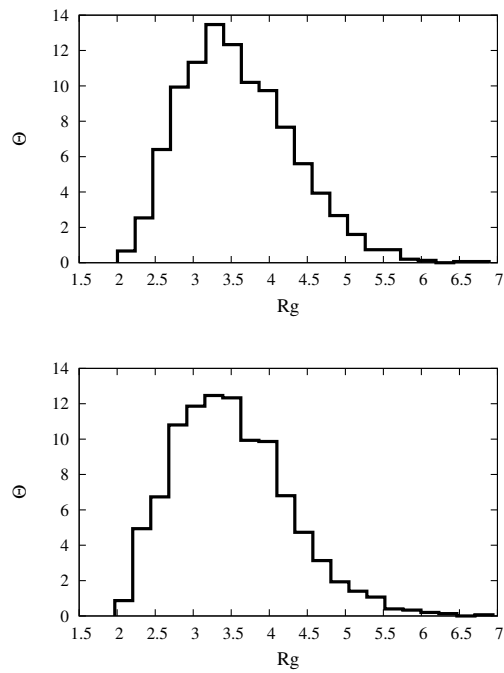


Figure 3.6: Percentage distribution of linear polymers ( $\Theta$ ) as a function of radius of gyration ( $Rg$ ) for  $t = 0$  (top) and  $t = 5 \times 10^7 \Delta t$  (bottom).

Table 3.2: Properties of linear polymers near a flat wall:  $z$  is the distance from the wall,  $\overline{R}_g^{lin}$  the average radius of gyration and  $\sigma^{lin}$  stands for variance.

$z$	$\overline{R}_g^{lin}$	$\sigma^{lin}$	$\overline{R}_g^{lin}$	$\sigma^{lin}$
Initial configuration			Final configuration	
53.76	3.56	0.90		
60.93	3.58	0.72	3.31	0.58
68.10	3.56	0.70	3.50	0.70
75.27	3.61	0.76	3.56	0.79
82.44	3.54	0.69	3.55	0.74
89.60	3.62	0.71	3.54	0.73
96.77	3.61	0.70	3.32	0.77
103.95	3.55	0.71		

### 3.4 Cyclic Polymers

The simulated system consists of cyclic chains (see Table 3.1 for physical quantities and parameters). The equilibration of the system is shown in Figure 3.7. For cyclic polymers, the 9-3 LJ potential is shifted at distance  $z = 47.72\sigma$ .

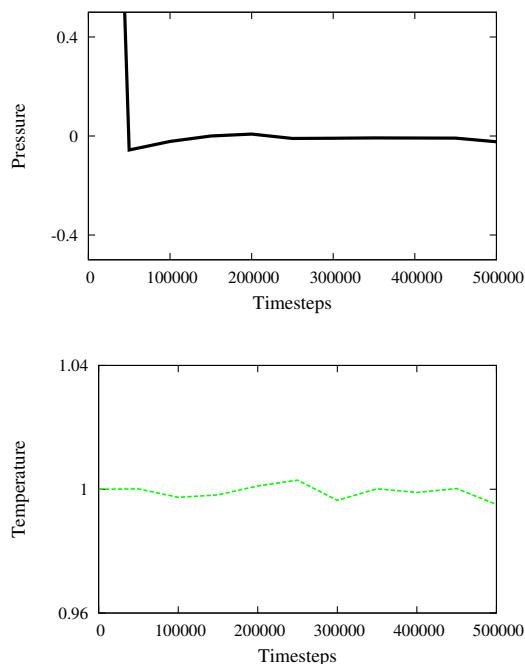


Figure 3.7: Plot of reduced pressure versus time (top) and reduced temperature versus time (bottom) for MD simulations of cyclic polymers.

The adsorption properties are evaluated by analysing the MD simulations initial configuration and the final one following  $5 \times 10^7 \Delta t$ . The top panel of Figure 3.9 shows the normalised histogram of cyclic polymers coms ( $T^{cyc}(z)$ ) as a function of distance  $z$  from the wall at  $t = 0$ . From a distance  $z = 0$  to  $z = 57\sigma$  and  $z = 106\sigma$  to  $z = 160\sigma$ , there are no particles. From  $z = 57\sigma$ ,  $T^{cyc}(z)$  quickly rises to reach a maximum of 3.5 times the bulk value ( $3.5\rho_0$ ). The histogram also shows that cyclic polymers coms are more concentrated in between  $z = 57\sigma$  to  $z = 106\sigma$  of the simulation box. At  $t = 5 \times 10^7 \Delta t$  (see bottom panel of Figure 3.9), the  $T^{cyc}(z)$  remains zero from  $z = 0$  to  $z = 63.8\sigma$  and  $z = 100\sigma$  to  $z = 160\sigma$ , then rapidly increases to a maximum number

of 5.0 times the bulk density value ( $5.0\rho_0$ ) of cyclic polymers. It can be seen from the histogram that cyclic polymers coms are more dense in between  $z = 60\sigma$  to  $z = 100\sigma$ . As reported in the bottom panel of Figure 3.9, in which the range of distances where the wall-bead potential is active is sketched as an interval on the  $z$ -axis, the wall-bead potential seems not to attract cyclic polymers near the flat wall. In the case of cyclic polymers as compared to the linear ones, there is again a 100% depletion at either end of the studied range, with condensation occurring in the middle. The results are reported in Figure 3.10. Figure 5.7 displays the percentage distribution of cyclic polymers having a specific radius of gyration. At  $t = 0$  and  $t = 5 \times 10^7 \Delta t$ , we observe that cyclic polymers histograms seem to have a lower average value of the radius of gyration (near the peak of the histograms) with respect to their linear counterparts (see Figure 3.6), since they possess a more compact shape. Over the same range of radius of gyration, there is again a decrease in the value of the peak indicating an increase of polydispersivity of radius of gyration.

The interval of radii of gyration of linear polymers is bigger compared to the cyclic polymers one, which implies that cyclic polymers assume more compact shapes when compared with linear polymers chains having the same degree of polymerisation, as expected on the basis of the different topology of the two types of polymers. The same calculation of the average radius of gyration and the variance of radius of gyration as a function of the distance from the bottom edge of the simulation box has been done in the case of cyclic polymers. As depicted in Table 3.3, the average radii of gyration of cyclic polymers in the final configuration are approximately the same as compared to the initial ones throughout the  $z$ -range. The distribution of the sizes of cyclic polymers of the two configurations did not vary significantly ( $\sigma^{cyc} \approx 0.3$ ), similarly as it was observed for linear polymers. In the initial configuration, cyclic polymers coms closer to the wall are in the range between  $z \approx 51.04\sigma$  and  $z \approx 56.14\sigma$  from the bottom edge of the simulation box. Then by performing a calculation similar to the one made for linear polymers, we realise that the average positions of the cyclic polymer beads are between  $z \approx 48.36\sigma$  and  $z \approx 53.46\sigma$ . Since the range of distances where the wall potential is active are from  $z \approx 47.72\sigma$  to  $z \approx 49.92\sigma$ , it can be concluded that in the initial configuration cyclic polymers were interacting with the wall via the 9-3 LJ potential depicted in Figure 3.8. For the final configuration, the estimated range of cyclic polymers coms closer to the wall is in between  $z \approx 61.25\sigma$  and  $z \approx 66.35\sigma$  from the bottom edge of the simulation box. The average positions of the cyclic polymer beads are between  $z \approx 58.77\sigma$  and  $z \approx 63.87\sigma$  far from the wall. The average positions range of cyclic polymer beads is greater as compared to the linear one estimated previously, which means that cyclic polymers closer to the wall seem to be moving significantly away from the wall as compared to the linear polymers. That could be visually observed also by comparing the bottom panels of Figs. 3.4 and 3.9. The variance of the radius of gyration of cyclic polymers is  $\approx 0.3\sigma$ , while the linear one is  $\approx 0.7\sigma$  indicating that no matter how far from the wall, cyclic polymers exhibit a smaller size polydispersivity than

linear polymers.

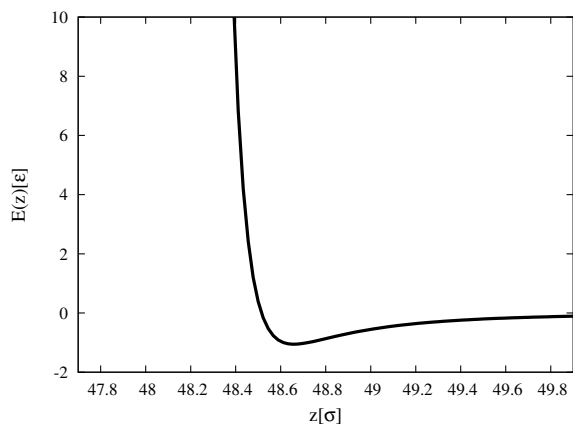


Figure 3.8: Wall 9-3 Lennard-Jones potential shifted at distance  $z = 47.72\sigma$ .

Table 3.3: Properties of cyclic polymers near a flat wall:  $z$  is the distance from the wall,  $R_g^{cyc}$  average radius of gyration and  $\sigma^{cyc}$  stands for variance.

$z$	$\overline{R}_g^{cyc}$	$\sigma^{cyc}$	$\overline{R}_g^{cyc}$	$\sigma^{cyc}$
Initial configuration			Final configuration	
53.59	2.68	0.35		
58.70	2.72	0.31		
63.80	2.72	0.30	2.48	0.30
68.91	2.69	0.30	2.55	0.32
74.01	2.70	0.30	2.53	0.30
79.12	2.67	0.32	2.53	0.30
84.22	2.70	0.34	2.54	0.32
89.33	2.70	0.32	2.54	0.30
94.43	2.64	0.29	2.52	0.32
99.53	2.65	0.31	2.59	0.35
104.64	2.74	0.36		

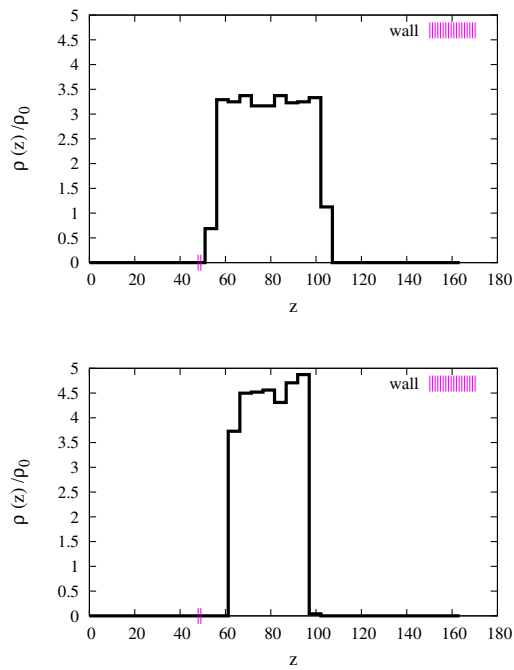


Figure 3.9: Number density distribution,  $\rho(z)/\rho_0$  versus distance  $z$  from the wall of cyclic polymers for MD simulations  $t = 0$  (top) and  $t = 5 \times 10^7 \Delta t$  (bottom). The interval between vertical bar on the  $z$ -axis is the range of distances where the wall-bead potential is active. For both configurations, the bin size of  $2\bar{R}_g = 5.10\sigma$  were used.

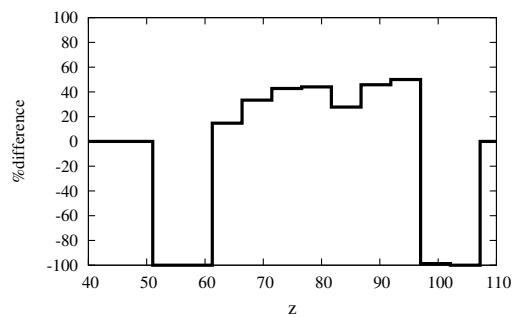


Figure 3.10: Percentage difference of distribution density as a function of distance  $z$  from the wall for cyclic polymers.

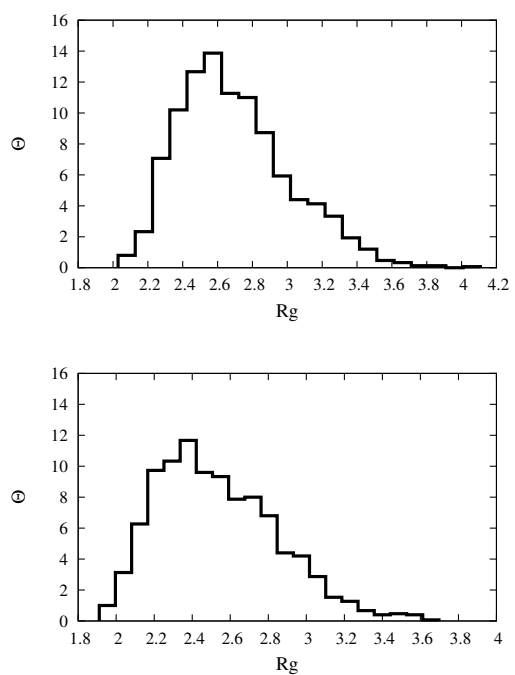


Figure 3.11: Percentage distribution of cyclic polymers ( $\Theta$ ) as a function of radius of gyration ( $Rg$ ) for  $t = 0$  (top) and  $t = 5 \times 10^7 \Delta t$  (bottom).

### 3.5 Linear-Cyclic mixtures

The simulated system consists of linear-cyclic polymers in melt state (see Table 3.1 for physical quantities and parameters). The equilibration of the system is shown in Figure 3.12. The plot of the attractive 9-3 LJ potential reported in Figure 3.13 is shifted at a distance  $z = 47.35\sigma$ .

The adsorption properties are evaluated again by analysing the MD simulations of the initial and the final configurations of the system following  $5 \times 10^7 \Delta t$ . Figure 3.14 shows the normalised histograms  $T^{cyc}(z)$  and  $T^{lin}(z)$  as a function of distance  $z$  from the wall in the blend for  $t = 0$  and  $t = 5 \times 10^7 \Delta t$ . At  $t = 0$ ,  $T^{lin}(z)$  in the blend remains zero from  $z = 0$  to  $z = 58\sigma$  and from  $z = 106\sigma$  to  $z = 180\sigma$ , which imply absence of particles in those ranges. From  $z = 58\sigma$ ,  $T^{lin}(z)$  quickly rises to reach a maximum of 3.7 times the bulk density value ( $3.7\rho_0$ ) of linear polymers in the blend, while  $T^{cyc}(z)$  in the blend also remains zero from  $z = 0$  to  $z = 55\sigma$  and from  $z = 107\sigma$  to  $z = 180\sigma$ , which indicate that no particles are found in those ranges. From  $z = 55\sigma$ ,  $T^{cyc}(z)$  rapidly rises to reach a maximum of 3.5 times the bulk density value ( $3.5\rho_0$ ) of cyclic polymers. Linear and cyclic polymers in the blend are more dense between  $z = 58\sigma$  to  $z = 110\sigma$  of the simulation box. At  $t = 5 \times 10^7 \Delta t$ ,  $T^{lin}(z)$  remains zero from  $z = 0$  to  $z = 59.9\sigma$  and from  $z = 103\sigma$  to  $z = 180\sigma$ , which indicate the absence of particles. From  $z = 59.9\sigma$ ,  $T^{lin}(z)$  rapidly increases to a maximum number of 3.7 times the bulk density value ( $3.7\rho_0$ ), while for cyclic polymers in the blend no particles are found from  $z = 0$  to  $z = 55\sigma$  and from  $z = 102\sigma$  to  $z = 180\sigma$ . From  $z = 55\sigma$ ,  $T^{cyc}(z)$  quickly rises to reach a maximum of 4.0 times the bulk density value ( $4.0\rho_0$ ). For this configuration, linear and cyclic polymers in the blend are more concentrated in between  $z = 55\sigma$  to  $z = 102\sigma$  inside the simulation box.

As it can be deduced by the comparison of top and bottom panels of Figure 3.14, linear polymers in melt do not seem to move significantly distant from the wall after a long time as compared to the case of pure linear polymers studied previously (see Figure 3.4). In melt state, the distribution of the linear polymers along the  $z$ -direction at  $t = 5 \times 10^7 \Delta t$  is almost the same as the initial one, while the distribution of the cyclic polymers seem to condense towards the middle of the box (by visual comparison of the top and the bottom panels of Figure 3.14) as we will see in more detail later. Thus, we need to understand whether linear polymers are prevented from diffusing far from the wall, as we observed in the case of pure linear polymers, because of polymer-wall interactions (the wall-bead potential is effective in attracting linear polymers near the wall) or because of linear-cyclic polymers interactions. Firstly, let us confirm the visual impression gained from Figure 3.14, that there is almost no depletion near the wall for the linear polymers blend and there is some in the case of cyclic polymers. We observe this by building up, similarly as in the pure cases, the percentage difference of the distribution density as a function of distance  $z$  from the wall in Figure 3.15. Figure 3.16 shows the percentage of linear-cyclic blend in melt having a specific radius of gyration. The spreading process of linear-cyclic polymers in melt state remain almost unchanged. At  $t = 0$ , the cyclic peak has a value of approximately 16.5%, whereas the

linear one is approximately 14%. At  $t = 5 \times 10^7 \Delta t$ , the value of the two peaks has decreased to approximately 12%, suggesting an increase of polydispersivity of the radius of gyration in melt state.

As found for pure cyclic polymers studied previously, cyclic polymers in melt state assume more compact conformations as compared to their linear counterparts having the same degree of polymerisation. Now, the structural analysis of the average radius of gyration and related variance as a function of the distance  $z$  from the wall, will be particularly enlightening in order to address the issue whether 1) linear polymers do not diffuse far from the wall because of wall polymers interactions or linear-cyclic interactions 2) cyclic polymers are interacting or not with the wall even though they seem to slightly diffuse towards the middle of the box as shown in Figure 3.15, and can be deduced by reading Table 3.4. Throughout the  $z$ -range, the average radii of gyration and variance of radius of gyration of linear polymers blend are almost the same in both configurations and their values are not significantly different from the pure linear ones studied previously. It can be concluded that whether in melt or not, the average size of linear polymers is not affected by the presence of the wall and both the average size and size polydispersivity of linear polymers are greater than those of cyclic polymers. In the initial configuration, linear polymers coms in melt closer to the wall are in between  $z \approx 54.52\sigma$  and  $z \approx 61.32\sigma$  from the bottom edge of the box. Then by performing the same analysis done for the pure cases, we observe that the average positions of the linear polymers beads in melt are between  $z \approx 51.30\sigma$  and  $z \approx 58.10\sigma$ . Since the range of distances where the wall potential is active is from  $z \approx 47.35\sigma$  to  $z \approx 49.55\sigma$  we can say that the initial configuration ( $t = 0$ ) of linear polymers in the blend was constructed in such a way that linear polymers were not interacting with the wall. In the final configuration, the average positions of linear beads closer to the wall is in the range between  $z \approx 50.98\sigma$  and  $z \approx 57.88\sigma$ . Since the range of average positions is almost the same in both the initial and the final configurations, it can be concluded that also in the final configuration, linear polymers in melt state are not interacting with the flat wall. Then, we can draw the conclusion that linear polymers seem not to diffuse towards the middle of the box (as in the pure case) because of linear-cyclic polymers interactions. As shown in Table 3.5, the distribution of the sizes of cyclic polymers in the final configuration reached by the polymer melt is almost the same as compared to the initial one. The estimated cyclic polymers coms positions closer to the wall are in between  $z \approx 52.02\sigma$  and  $z \approx 57.22$  in the initial configuration and the average positions of the cyclic polymer beads is between  $z \approx 49.33\sigma$  and  $z \approx 54.53\sigma$ . Since the range of distances where the wall potential is active is comprised between  $z \approx 47.35\sigma$  to  $z \approx 49.55\sigma$  it can be concluded that cyclic polymers are only loosely interacting with the wall in the initial configuration via the 9-3 potential reported in Figure 3.13. In the final configuration, the average positions of the cyclic polymer beads becomes in between  $z \approx 49.62\sigma$  and  $z \approx 54.81\sigma$  throughout the  $z$ -range, indicating that most of cyclic polymers in melt are moving away from the wall. Referring also to the result reported in Figure 3.15, it can be deduced that

cyclic polymers in melt state are not interacting with the flat wall and they seem to slightly diffuse towards the middle of the box because of cyclic-cyclic or linear-cyclic polymers interactions.

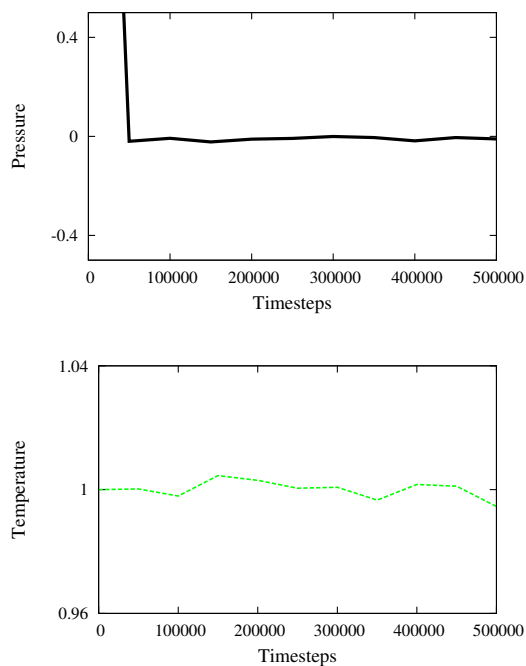


Figure 3.12: Plot of reduced pressure versus time (top) and reduced temperature versus time (bottom) for MD simulations of linear-cyclic polymers in melt.

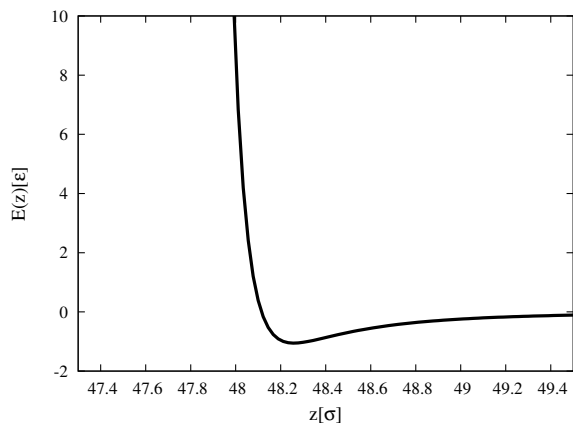


Figure 3.13: Wall 9-3 Lennard-Jones potential shifted at distance  $z = 47.35\sigma$ .

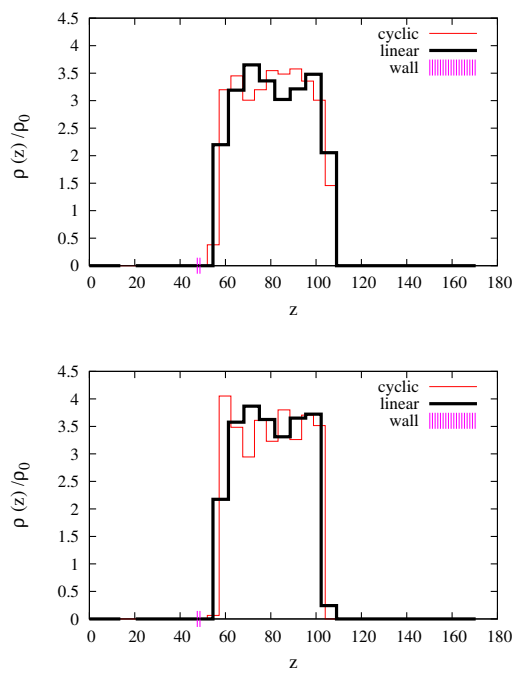


Figure 3.14: Number density distribution,  $\rho(z)/\rho_0$  versus distance  $z$  from the wall for linear and cyclic polymers blend for  $t = 0$  (top) and  $t = 5 \times 10^7 \Delta t$  (bottom). The interval between vertical bar on the  $z$ -axis is the range of distances where the wall-bead potential is active. For both configurations, the bin size of  $2\bar{R}_g = 6.80\sigma$  for linear and  $2\bar{R}_g = 5.20\sigma$  for cyclic polymers were used.

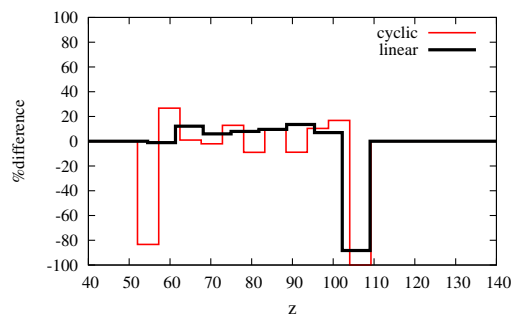


Figure 3.15: Percentage difference of the distribution density as a function of distance  $z$  from the wall for linear-cyclic polymers.

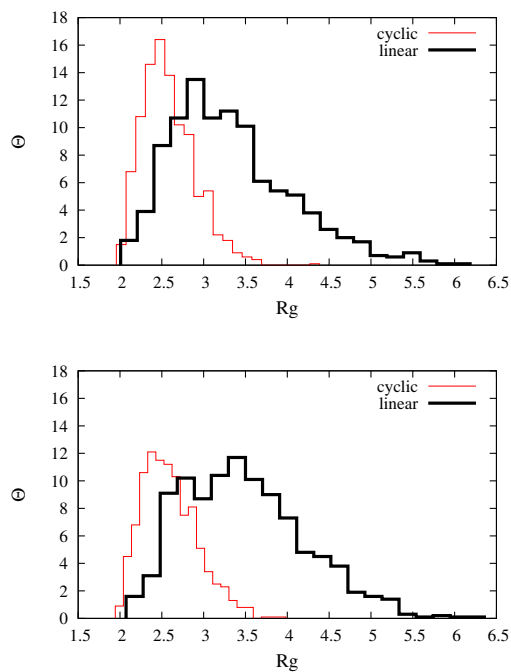


Figure 3.16: Percentage distribution of linear-cyclic polymer blend ( $\Theta$ ) as a function of radius of gyration ( $Rg$ ) for  $t = 0$  (top) and  $t = 5 \times 10^7 \Delta t$  (bottom).

Table 3.4: Properties of linear polymers near a flat wall in melt state:  $z$  is the distance from the wall,  $\overline{R}_g^{lin}$  average radius of gyration and  $\sigma^{lin}$  stands for variance.

$z$	$\overline{R}_g^{lin}$	$\sigma^{lin}$	$\overline{R}_g^{lin}$	$\sigma^{lin}$
Initial configuration			Final configuration	
57.92	3.22	0.61	3.54	0.72
64.74	3.35	0.72	3.42	0.71
71.55	3.36	0.72	3.46	0.72
78.37	3.34	0.72	3.48	0.67
85.18	3.27	0.70	3.48	0.67
92.00	3.38	0.69	3.53	0.75
98.81	3.33	0.80	3.41	0.68
105.63	3.30	0.70	3.19	0.63

Table 3.5: Properties of cyclic polymers near a flat wall in melt state:  $z$  is the distance from the wall,  $\overline{R}_g^{cyc}$  average radius of gyration and  $\sigma^{cyc}$  stands for variance.

$z$	$\overline{R}_g^{cyc}$	$\sigma^{cyc}$	$\overline{R}_g^{cyc}$	$\sigma^{cyc}$
Initial configuration			Final configuration	
54.62	2.69	0.36	2.41	0.11
59.82	2.58	0.29	2.60	0.35
65.03	2.57	0.29	2.60	0.35
70.23	2.57	0.28	2.53	0.30
75.43	2.60	0.29	2.59	0.29
80.63	2.58	0.30	2.59	0.32
85.84	2.55	0.32	2.64	0.32
91.04	2.59	0.32	2.56	0.30
96.24	2.56	0.32	2.64	0.35
101.44	2.57	0.33	2.56	0.30
106.65	2.62	0.41		

## 3.6 Conclusions

We have performed some preliminary numerical simulations of both pure linear and cyclic films and of an equimolar linear-cyclic blend. This study was aimed to reach an understanding of the time and length-scales involved in the computer simulations of the system of interest. The most important information we gained during this preliminary investigation of the system was that it needs to be equilibrated for longer times when the period boundary conditions are interrupted along the  $z$ -direction in order to generate an interface. When we tried to keep the polymers adsorbed onto a wall positioned at a proper distance from the polymer film, we noted that polymer-polymer interactions drove the polymer film far away from the wall and determined further shrinkage of its thickness along the  $z$ -direction.

While the aim of this chapter was not to analyze in any detail the physics of the system, we also observed some expected features. The first one is that when two empty space-polymer system are generated, the system tends to further increase its particle density because polymer beads can minimize their energy by moving far from the empty space and by enhancing the number of interactions with themselves. Another evidence is that whether in melt or not, both the average size and size polydispersivity of linear polymers are greater than those of cyclic polymers. In fact, the absence of the loop constraint present in cyclic chains allows linear chains a greater flexibility. The latter can be successfully used in order to further decrease their interaction energy by better packing against other polymers.

## Chapter 4

# Free-standing Linear-Cyclic Polymer Blends

### 4.1 Introduction

Self-consistent Gaussian Field Theory (GFT) predicts that when considering blends of linear and cyclic polymers, the latter are expected to be preferentially enriched at the interface, and this process is not influenced by the precise value of the molecular weight of the polymers [42]. Recently, Wang and coworkers [12] used a sophisticated surface sensitive spectroscopic technique (SL-MALDI-TOFMS) on polymer blends with polystyrene chemistry, that provided evidence of enrichment of linear chains at the surface in the regime of lower cyclic composition [12]. Neutron reflectivity (NR) experiments on the same systems showed that the degree of surface segregation of cyclic polymers is dependant on the molecular weight of the cyclic chains [80]. The evidence is that when chains possess a low molecular weight ( $\approx 2k$ ), linear polymers enrich the surface and the behavior expected theoretically (cyclic polymers absorbing preferentially to the surface) emerges only in the limit of much longer polymer chains ( $\approx 37k$ ). Numerical studies of linear-ring polymer blends were performed with equilibrium and non-equilibrium molecular dynamics simulations [14, 81, 82] and focused mainly on the low-composition linear regime where the diffusion of cyclic polymers is observed to decrease dramatically in comparison to linear chains [14]. Interfacial and structural properties of polymer melts have also been investigated [83, 84], but not much attention has been given so far to polymer blends in the melt state. A Monte Carlo computer simulation study by Yethiraj [52], conducted on mixtures of linear and branched chains, provided evidence that when fluid-fluid interactions are activated among polymer beads, the branched polymers enrich the surface while linear chains tend to maximize their cohesive energy by staying in the bulk of the mixture because they are more flexible [52]. However, when fluid-fluid interactions are switched off, the linear chains tend to enrich the surface, by providing evidence of a genuine entropy-driven

mechanism. Evidence of an entropic segregation was also reported recently for cyclic polymers in cylindrical confinement [85]. The experimental evidence of the relevance of entropy in determining the surface excess at the air-polymer film interface was recently provided by Lee and coworkers [13] for blends of branched and linear polymer chains. In the case of a low-energy surface, such as air or vacuum, the polymer species with the lower cohesive energy density is expected to be favored at the surface because of its lower surface tension [42, 52].

In this chapter, we keep our description of polymer interactions in terms of the bead-spring model of Grest and Kremer [25, 26], and we initially explore some selected systems where linear polymer are more concentrated, namely  $c_0 = N_l^0 / (N_c^0 + N_l^0) = 0.7, 0.8$ , where  $N_c^0$  and  $N_l^0$  are the total number of cyclic and linear polymers in the simulation box. We generated initial configurations for binary mixtures of linear and cyclic polymers of  $N_b = 7, 10, 20, 30, 50, 100$  beads per polymer and the blend is exposed to empty space at low- and high- $z$  values. Just to anticipate some quantities of interest, the chain length and the concentrations were varied to analyze and to compare the short and the long-chains dynamics in determining surface enrichment. Our aim was to understand the possible microscopic mechanisms underlying polymer enhancement at the interface, and in achieving this goal we wanted to understand the role of entropic factors, such as architecture, molecular weight, and the position of chain-ends of linear polymers, in determining which of the two polymer species will preferentially be absorbed at the interface. While we focus initially just on the compositions where experiments observed an anomalous enhancement of linear polymers in comparison to cyclic ones (anomalous because of the different theoretical predictions by the GFT), in a different section we also explore the whole composition regime.

## 4.2 Model and Methods

The initial configuration was prepared by inserting the centers of mass of linear and cyclic polymers randomly onto the sites of a parallelepiped lattice. The lattice parameters of the parallelepiped box were chosen large enough to avoid the formation of knots between cyclic and linear polymers. Also their beads were occupying random positions in space compatible with the FENE potential, as it is described below. For both the two polymer species, the distance between subsequent beads was initially made equal to the minimum of the FENE potential  $d_{FENE}$ . In order to generate the initial conformation of a linear polymer as an open chain of beads we proceeded as follows:

- Starting from an initial point in space, we selected a random direction (in terms of a unit vector), and we positioned a ghost particle to a distance equal to  $d_{FENE}$ .
- We allocated the subsequent particle along the chain by using as a starting point for the unit vector the new ghost particle allocated before, and we iterated the procedure reported in these two bullet points again. We stopped the iteration when we reached a number of particles equal to the degree of polymerization.

In order to generate an initial conformation of a cyclic polymer as a closed chain (loop) of particles, we proceeded as follows:

- Starting from an initial point in space, we selected a random direction (in terms of a unit vector), and we positioned a particle to a distance equal to  $dFENE$ .
- Starting from that particle, the position of the subsequent one is generated to a distance equal to  $dFENE$  with probability  $p = 1 - \frac{N}{N_b}$  along the direction determined by the unit vector with components given by uniformly-generated random numbers in the interval  $[0, 1]$ . In the formula of the probability  $p$ ,  $N$  is the current number of particles of the growing cyclic polymer and  $N_b$  is the degree of polymerization. Otherwise (this is done with probability  $1 - p$ ), we generate a unit vector with direction parameters corresponding to those of the line connecting the last particle of the growing cyclic polymer with the first one.

There are two events which could possibly spoil the algorithm. Let us analyze them in detail: the first one is when we come closer to the initial particle of the cyclic chain before we complete positioning in space particle number  $N_b - 1$ . In this case, the algorithm will select the position of the subsequent particle by placing it along a random direction (likewise we did for beads of linear polymers). The other possibility is that the particle number  $N_b - 1$  does not come close enough to the initial particle i.e. it is distant from the initial particle more than  $2 \times dFENE$ . However this event is very unlikely because we continuously bias the choice of the unit vector so that the probability that we place the next particle along the direction connecting it to the initial one, it does increase with the total number of particles of the growing cyclic polymer.

When particle number  $N_b - 1$  is added to the growing polymer, we need to place the subsequent one so that it is located at a distance equal to  $dFENE$  from both the initial particle (particle 1) and particle number  $N_b$ . In this case, we close the loop by adding particle number  $N_b$  with coordinates given analytically by the solution of the system of three equations where two equations fix the distance of the first particle, and of particle number  $N_b - 1$  to be equal to  $dFENE$  from  $N_b$ , and the last equation is given by the condition that the first particle, particle number  $N_b - 1$ , and the center of mass of the cyclic polymer belong to the same plane. Then, since there are two possible solutions to this coupled system of equations (the system is a second order one and it has three equations: for the sake of completeness and also to avoid to make the thesis crowded with long formulas, we did not report the solutions of the system in the thesis [78]), we select the one that places particle number  $N_b$  in the position more distant from the center-of-mass of the cyclic polymer. This choice reduces the number of rejections due to the fact that most particles have already been allocated in positions closer to the polymer center-of-mass.

Almost all of the computer simulations were executed in two different clusters: 1) the 920 processor 2.8 GHz AMD Opteron cluster available in the research group of Prof M. Tsige at the University of Akron, USA. 2) The 50 compute nodes, each with dual Xeon e5-2680v2 CPUs (10 core

Ivy Bridge, 2.8 GHz base frequency) and 64 GB of RAM. Once a convenient number of polymers was generated by means of the procedure detailed above, and these polymers were allocated to the lattice sites of the initial parallelepiped box, a LAMMPS MD simulation with the directive `fix/DEFORM` was used to shrink the box isotropically to the desired volume. Initial configurations at the desired density were simulated with full periodic boundary conditions (PBCs) for not less than  $10^7$  MD steps. Then, PBCs were kept along the  $x$ - $y$ -dimensions, while along the  $z$ -dimension the box was elongated so to expose polymers to empty space, and generate two vacuum-blend interfaces at low- and high- $z$  values. However, the discontinuance of the PBCs along the  $z$ -direction means that the polymers localized in proximity of the edge of the box become broken since a part of them will be shifted on the opposite side of the box at a distance exactly equal to  $L_z$ , which is the original length of the box in the  $z$ -direction. Then, the broken polymers nearby the newly-generated polymer-empty space interfaces had to be rebuilt and the configuration so obtained was equilibrated for  $10^8$  MD steps. Quantities of interest were averaged out in the last 2–10 million MD steps. We studied systems with a total number of particles ranging from  $N^0 = N_c^0 + N_l^0 = 10^5$  for systems with smaller degrees of polymerization to  $N^0 = 2 \cdot 10^5$  for systems with higher number of beads per polymer. In studying the properties of the system in the simulation box as a function of the distance from the interface, the polymer blend was subdivided along the direction orthogonal to the interface into slices (bins) of size  $\sigma$ . Several time-dependent properties, including for example time-averaged mean-square displacements and diffusion coefficients were calculated as averages over single layers located at specific distances from the interface.

When we had to eliminate the bias of not having a clear flat, planar interface separating the polymer mixture from the empty space, we constructed a instantaneous interface with the procedure detailed below. In order to build a time-averaged number histogram for the particle (or group of particles) being targeted, we first operated a partition of the simulation in cubic cells of small size ( $\sigma$ ) at a given time-step. An histogram was built by searching inside cells for particles belonging to the targeted type. The cells were analyzed starting from the empty space and moving along the  $z$ -axis inside the blend. In this procedure, the first-occupied cell defines the first bin of the histogram. Once this calculation is iterated for all the cells starting from the empty space, the final histogram is obtained by summing up all of them. Since the histogram reflecting the true exposure of particles to empty space was built at a specific instant of time (corresponding to the configuration of particles in the simulation box dumped at a specific timestep), we refer to these calculations as those related to the 'instantaneous interface'. Obviously, system configurations are being dumped with a certain frequency and the histogram reported in our calculations was always averaged out over a number of frames. We can consider the following example to understand how the procedure works. If we have particles of two types, circles and crosses (as reported in Figure 4.1), and we want to calculate the instantaneous histogram for the number of crosses, the first step is to build the renormalized histograms starting from the first unoccupied cell, as it is

shown in moving from the top to the middle part of Figure 4.1. Empty space is supposed to be located on the left of the figure. Once all these histograms are determined, they are summed up bin by bin (see the bottom part of the figure) to get final histogram for the chosen configuration.

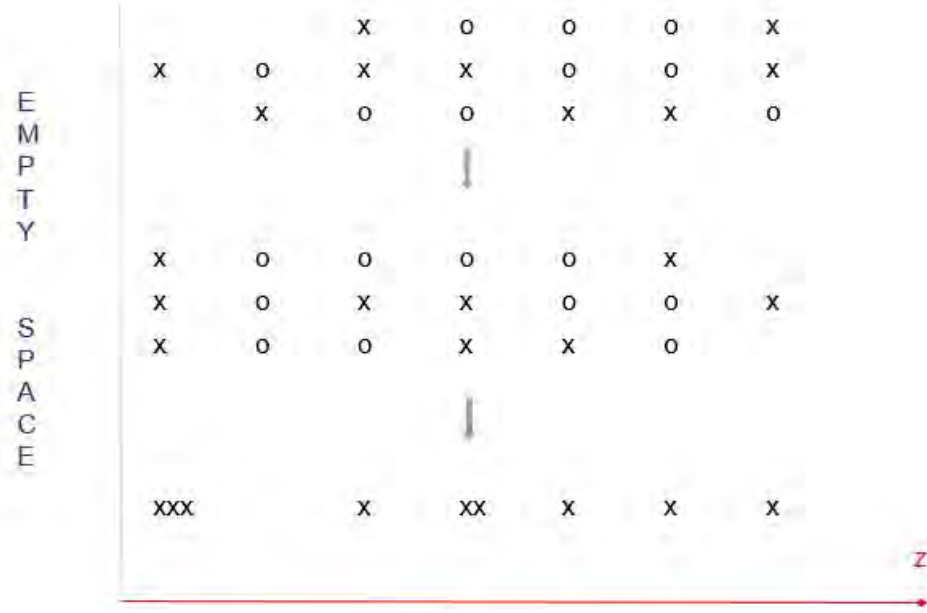


Figure 4.1: Sketch of the construction of the histogram for the number of crosses resulting from the instantaneous interface for a two-dimensional system of crosses and circles.

## 4.3 The Low Cyclic Composition Regime

### 4.3.1 Density and Local Composition Profiles

The adsorption properties of linear-cyclic polymer blends at interface were characterized by calculating the number density profile  $\rho(z^*)$  of the film, i.e. a quantity that is directly linked to the volume fraction of beads and that is also accessible to experiments, as a function of distance  $z^* = z/\sigma$  from the surface, at different composition and chain length. As anticipated before, we divided the simulation box into bins along the  $z$ -direction, with bin size  $\Delta z = \sigma$ . This bin size was chosen in order to get a good statistics (based on the total number of particles used in the computer simulations), while at the same time selecting a length-scale over which analyzing the local density equal to the size of polymer beads. Then, the local density for species  $i$ , where  $i \equiv c, l$  depending on the particle belonging to a cyclic or a linear polymer, is defined as

$$\rho_i = \frac{N_{i,slice}}{V_{slice}}, \quad (4.1)$$

where  $N_{i,slice}$  is the number of particles of polymer species  $i$  contained in a slice perpendicular to

the interface of thickness  $\sigma$ , and  $V_{slice}$  is the volume of that slice. Obviously when the distance from the interface increases, the local density  $\rho_i$  tends to the corresponding *bulk* value  $\rho_i^0 = \frac{N_i^0}{V}$  far from the interface, where  $V$  is now the total volume of the system. A similar consideration applies to the local composition of linear polymers, that is defined as

$$c = \frac{N_{l,slice}}{(N_{c,slice} + N_{l,slice})} \quad (4.2)$$

that should also tend to the corresponding *bulk* value  $c_0 = N_l^0/(N_c^0 + N_l^0)$  far from the interface. However, since the total number of particles in the simulation box is a conserved quantity, we expect  $\rho_i$  and  $c$  to be slightly different from the truly, corresponding *bulk* values: in other words, if there is an enhancement or a depletion of particles at the interface, then the number of particles available in the middle of the simulation box (the two blend-empty space interfaces are taken as starting and ending references to define where the middle of the simulation is located) will be different than the expected *bulk* value. The latter would be found just in the case the system is a homogeneous one, i.e. no interface would exist to perturb the system). When we consider the local composition  $c$ , we decided to still use the *bulk* value  $c_0 = 0.7, 0.8$  (depending on the composition of the system being considered), so the quantity that we report is

$$Ratio = \frac{c}{c_0}. \quad (4.3)$$

Figures 4.2-4.3 show the local density for the two type of chains as a function of the distance from the interface. As expected, if we look at the panels reported in the same line (bottom for  $c_0 = 0.7$  or top panel for  $c_0 = 0.8$ ), we clearly see that the densities achieved by the two polymer species far from the interface are very similar regardless of the degree of polymerization. This is important since we would like to study the effect of polymer mass under the same density conditions. Note again that the top panels of Figures 4.2-4.3 are for the higher linear chain composition ( $c^0 = 0.8$ ), while the bottom ones for the lower one ( $c^0 = 0.7$ ). In fact, the densities of linear polymers far from the interface get depleted in going from  $c^0 = 0.8$  to  $c^0 = 0.7$ , while the opposite behaviour happens for cyclic chains. However, there are subtle differences nearby the interface, which are hardly detected by looking at the densities on the scale of Figures 4.2-4.3. We can start having some idea of these differences by looking at Figures 4.4-4.5, where we report the local compositions of linear and cyclic chains as a function of the distance from the interface. In order to spot any variations from the *bulk* composition, we scaled the local compositions by the corresponding *bulk* value, which is  $c^0 = 0.8$  (0.2 for cyclic polymers) for the top panels and  $c^0 = 0.7$  (0.3 for cyclic polymers) for the bottom ones. As a general feature that emerges from the visualization of these figures, we note that nearby the interface there is an enhancement of the local composition for linear chains at short-intermediate chain lengths, and a corresponding depletion of this quantity for cyclic chains. However, when we reach the degree of polymerization  $N_b = 50$ , we observe that cyclic chains get enhanced and linear chains depleted correspondingly.

Table 4.1 contains the average local composition calculated nearby the two interfaces as a

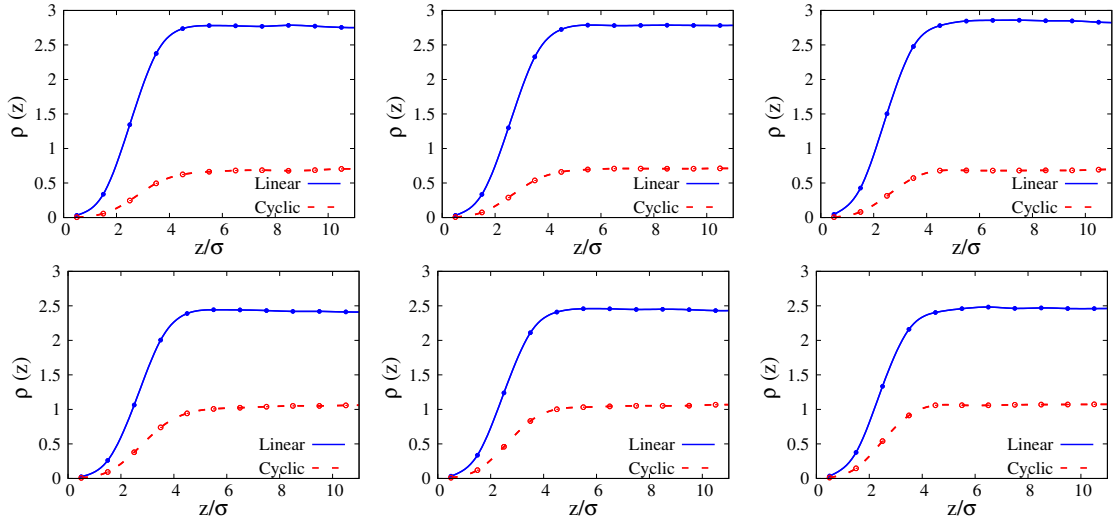


Figure 4.2: Local density profiles of free-standing films made of 7-mers (leftmost panels), 10-mers (middle panels), and 20-mers (rightmost panels) chains at low cyclic concentrations:  $c^0 = 0.8$  (top panels) and 0.7 (bottom panels).

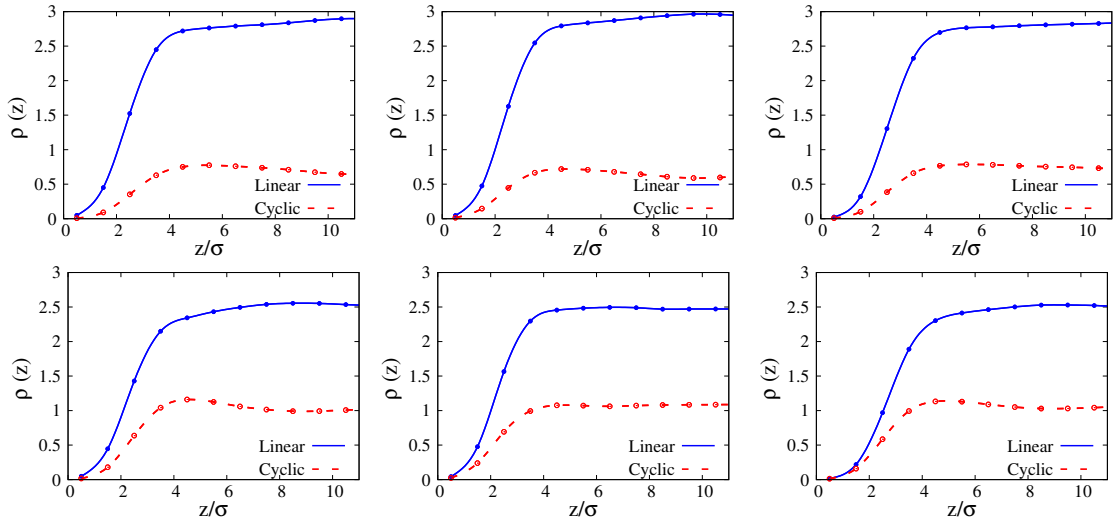


Figure 4.3: Local density profiles of free-standing films made of 30-mers (leftmost panels), 50-mers (middle panels), and 100-mers (rightmost panels) chains at low cyclic concentrations:  $c^0 = 0.8$  (top panels) and 0.7 (bottom panels).

function of chain length, and it summarizes our main finding: linear polymers enrich the surface in the case of short-chain lengths, while the opposite happens in the limit of long-chain lengths.

In order to get a clear understanding of the effect of increasing the chain length for the two polymer species, we focus now on a direct comparison of the results for short-chains against those for long-chains. The top panel of Figure 4.6 shows the average number density histogram  $\rho = N/V$  for  $N_b = 10, 100$  and for the two polymer species as a function of the distance from the interface. We note that in both cases, the onset of the *bulk* conditions takes place at a distance of  $4\sigma - 5\sigma$ .

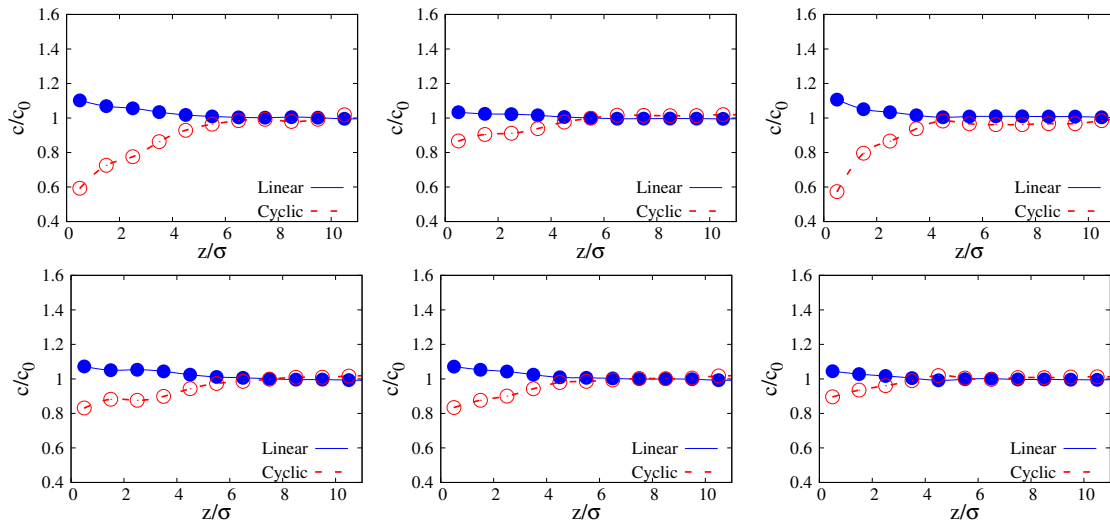


Figure 4.4: Local Composition profile of free-standing films made of 7-mers (leftmost panels), 10-mers (middle panels), and 20-mers (rightmost panels) chains at low cyclic concentrations:  $c^0 = 0.8$  (top panels) and 0.7 (bottom panels).

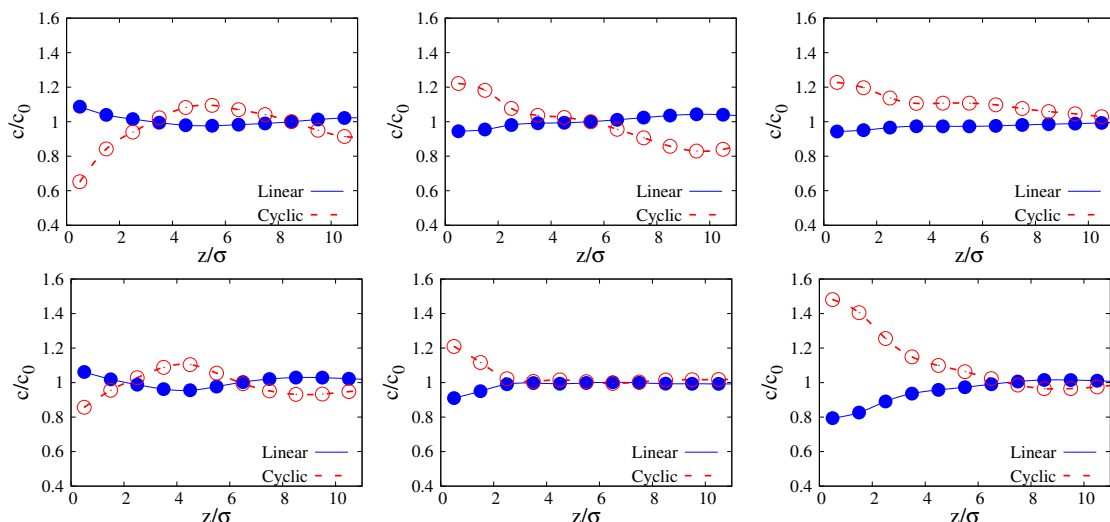


Figure 4.5: Local Composition profile of free-standing films made of 30-mers (leftmost panels), 50-mers (middle panels), and 100-mers (rightmost panels) chains at low cyclic concentrations:  $c^0 = 0.8$  (top panels) and 0.7 (bottom panels).

In the figure, the upper curves are for linear polymers, while the lower ones are for cyclic ones. The densities of the two species far from the interface are in the ratio 30 : 70, as expected for the case  $c = 0.7$ . Let us focus on the upper curves, which are reported both in the main top panel and in the inset, that zooms over the blend very close the interface. We note that the density of short-chain linear polymers ( $N_b = 10$ ) is enhanced with respect to the density of long-chain linear polymers ( $N_b = 100$ ). A different behavior emerges when we look at the pair of lower curves, which represent the densities for cyclic polymers: the density of long-chain cyclic polymers is enhanced

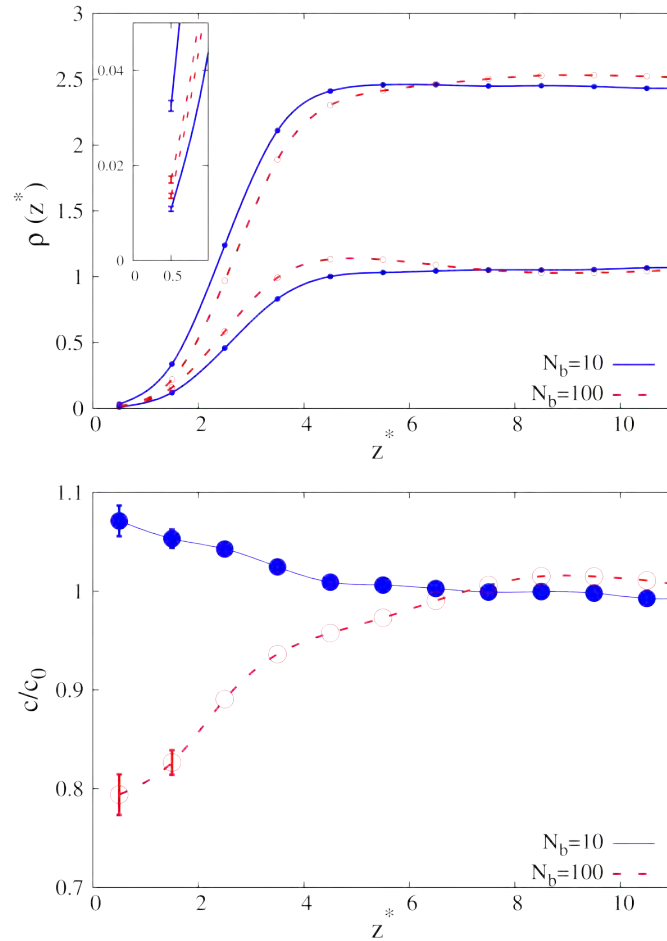


Figure 4.6: Top panel: particle density histogram as a function of the distance from the interface for  $c = 0.7$ . The pair of bottom curves are for cyclic chains; upper ones for linear chains. Error bars smaller than the size of the symbol are not reported. Inset: zoom of the region nearby the interface. Bottom panel: local composition plot for linear polymers as a function of the distance from the interface. Data are scaled by the *bulk* composition  $c_0 = 0.7$ . Error bars smaller than the size of the symbol are not reported.

Table 4.1: Local compositions (linear polymers) vs chain length

Chain length	0.7	error	0.8	error
7-mers	0.7505	0.0116	0.8814	0.0141
10-mers	0.7434	0.0087	0.8704	0.0236
20-mers	0.7253	0.0240	0.8630	0.0170
30-mers	0.7160	0.0064	0.8505	0.0057
50-mers	0.6651	0.0073	0.7679	0.0065
100-mers	0.6032	0.0071	0.7665	0.0051

with respect to the density of short-chain cyclic polymers. The bottom panel of Figure 4.6 shows the effect of these density enhancements. We can see that near the interface the local composition  $c$  of linear polymers becomes enhanced with respect to the *bulk* value in the case of long chains ( $N_b = 100$ ), and depleted for short chains ( $N_b = 10$ ). The evidence for short-chains is compatible with what was reported in SL-MALDI-TOFMS experiments [12] for polystyrene polymers with linear and cyclic architecture. In fact, the molecular mass of h-CPS2k and h-LPS2k polymers used there is 2300/2700 g/mol, which by assuming an entanglement length  $N_e = 78$  instead of  $N_e = 35$  as reported in Ref. [26] (the latter estimate is recognized to be a poor one for polystyrene polymers), and a monomer mass 104, it allows us to map the experimental system on a bead-spring model with  $N_b = 10 - 11$ . Our results for long chains are also in qualitative agreement with the predictions of GFT [86]. Table 4.1 reports the average local composition calculated for a thickness of the surface layer equal to the *bulk* average radius of gyration for different chain lengths, and it summarizes our main finding: linear polymers enrich the surface for short chain lengths, while the opposite happens in the limit of long chain lengths. Our data predict that the threshold between the two regimes is reached between  $N_b = 30 - 50$  beads per polymer, i.e.  $\approx 7000 - 12000$  g/mol.

### 4.3.2 Radius of Gyration

As a first quantity to provide some insight into the behaviour highlighted in the previous section, we looked at the radius of gyration  $R_g$  that is directly linked to polymer flexibility and conformational entropy, and we calculated it as a function of the distance from the interface. We briefly summarize the definition of it as reported in the previous chapter. The position of a polymer at time  $t$  is defined by the position of its center-of-mass ( $\vec{r}_{com}(t)$ ), which is given by

$$\vec{r}_{com}(t) = \frac{1}{N_b} \sum_{i=1}^{N_b} \vec{r}_i(t), \quad (4.4)$$

where  $N_b$  is the number of monomers in a single polymer chain, and  $\vec{r}_i(t)$  is the vector describing the position of the com at time  $t$ . The position of the center-of-mass can be used to determine

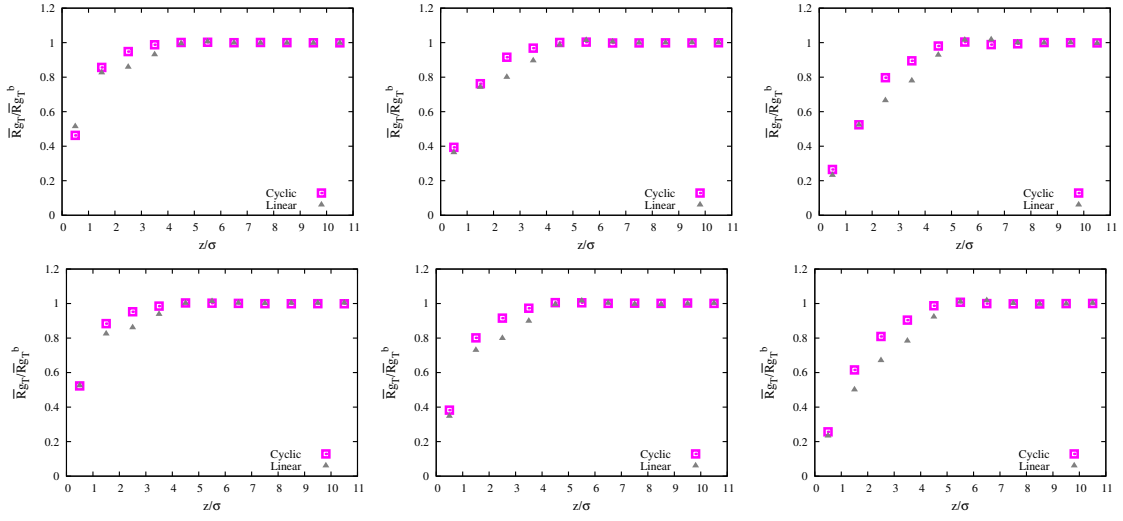


Figure 4.7: Average perpendicular component radius of gyration of free-standing films made of 7-mers (leftmost panels), 10-mers (middle panels), and 20-mers (rightmost panels) chains at low cyclic concentrations:  $c^0 = 0.8$  (top panels) and 0.7 (bottom panels).

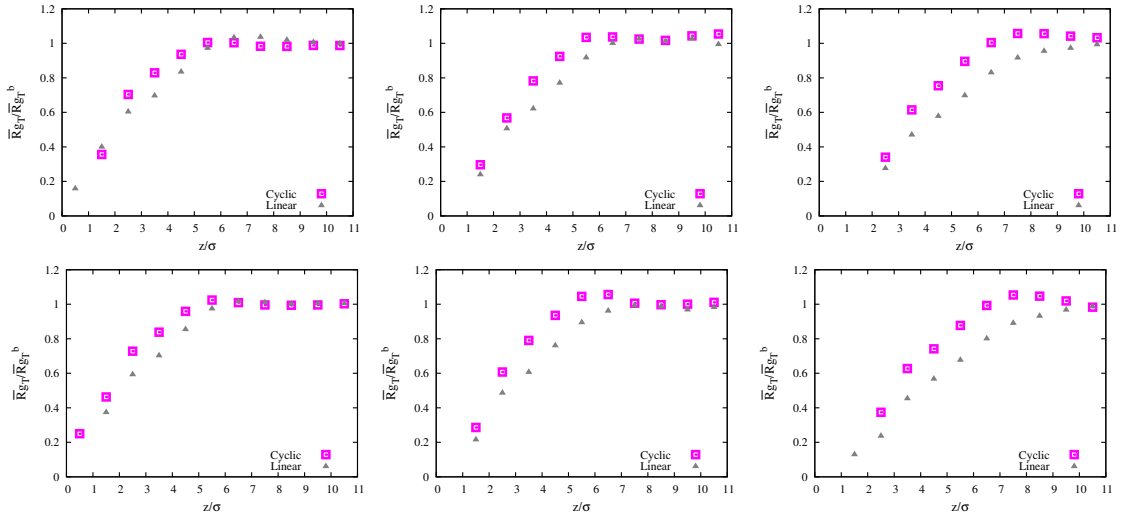


Figure 4.8: Average perpendicular component radius of gyration of free-standing films made of 30-mers (leftmost panels), 50-mers (middle panels), and 100-mers (rightmost panels) chains at low cyclic concentrations:  $c^0 = 0.8$  (top panels) and 0.7 (bottom panels).

the effective size of the single polymer in three dimensions at time  $t$ , which is described using the mean square distance of polymer beads from the com. Then, the mean square distance from the com can be averaged over different timesteps to get the square of the radius of gyration  $\bar{R}_g^2$ :

$$\bar{R}_g^2 = \langle \bar{R}_g^2(t) \rangle = \left\langle \frac{1}{N_b} \sum_{i=1}^{N_b} (\vec{r}_i(t) - \vec{r}_{com}(t))^2 \right\rangle. \quad (4.5)$$

However, since the geometry of our simulation box enhanced the formation of a polymer blend-empty space interface which is parallel to the  $x$ - $y$  plane, we can exploit this feature to study the

structural rearrangement of the polymers near the interface by considering the transverse ( $\perp$ ) and parallel ( $\parallel$ )  $\overline{R}_g^2$  components to the interface:

$$\overline{R}_{g\perp}^2 = \langle \overline{R}_g^2(t) \rangle_{\perp} = \left\langle \frac{1}{N_b} \sum_{i=1}^{N_b} (z_i(t) - z_{com}(t))^2 \right\rangle \quad (4.6)$$

and

$$\overline{R}_{g\parallel}^2 = \langle \overline{R}_g^2(t) \rangle_{\parallel} = \left\langle \frac{1}{N_b} \sum_{i=1}^{N_b} \left[ (x_i(t) - x_{com}(t))^2 + (y_i(t) - y_{com}(t))^2 \right] \right\rangle, \quad (4.7)$$

satisfying the following identity  $\overline{R}_g^2 = \overline{R}_{g\perp}^2 + 2\overline{R}_{g\parallel}^2$ . If we look at the transverse component of  $\overline{R}_g^2$  as a function of the distance from the interface, as reported in Figures (4.7)-(4.8), we note as a general trend that both polymer species tend to become more folded in the direction perpendicular to the interface as they approach it. These two quantities are scaled by their respective *bulk* counterparts, as they are reported in Tables 4.2-4.3, in order to understand how the interface affects both the size and the shape of the two polymer species. For short-chains it appears that regardless of the composition change of the system from  $c = 0.7$  (bottom panels of Figure 4.7 to  $c = 0.8$  (top panels of the same Figure), the values of  $\overline{R}_{g\perp}^2$  are very similar. However, there is a tendency of  $\overline{R}_{g\perp}^2$  to become smaller in the intermediate range of distances from the interface for linear chains, and this is a bit more marked for the composition where cyclic polymers are less diluted ( $c = 0.7$ ). As we consider the longer chains (see Figure 4.8), this is even more evident, and we even see that linear chains end up possessing a smaller value of  $\overline{R}_{g\perp}^2$  at the interface. The evidence that sometimes there are no data for the cyclic chains very close to the interface is due to their com being not detected there across the different blend configurations dumped at different timesteps. The results for the parallel component of  $\overline{R}_g^2$  are reported in Figures 4.10-4.11, and show a similar trend as it was detected for the transverse component. There are a couple of features which come out as interesting ones when looking at these Figures more carefully. On one side, there is a tendency of  $\overline{R}_{g\parallel}^2$  for cyclic chains to exhibit a maximum at intermediate distances or not far from the interface. On the other one, we observe that the trend reported for the transverse component is even more enhanced for  $\overline{R}_{g\parallel}^2$ . The values of the three-dimensional radius of gyration along with its parallel and transverse components far from the interface are shown in Tables 4.2-(4.3. The similarity of the values of  $\overline{R}_{g\parallel}^2$  and  $\overline{R}_{g\perp}^2$  far from the interface demonstrates that when the two polymers are sufficiently far from the interface, their shapes are nearly spherical ones and there is no particular shape they assume. Moreover, we note that linear chains are more unfolded than cyclic chains, as it is expected because the absence of the loop in linear polymers makes them more flexible and able to unfold to a larger extent. Similarly as in the case of the density and local composition histograms, we can try to have a better understanding of the effect of changing the chain length by comparing the radii of gyration for the two cases of short and long chains. In Figure 4.9, we show the transverse  $R_g^T$  and parallel  $R_g^P$  components of  $R_g$  to the interface for the two polymers species when  $N_b = 10, 100$ . The bulk  $\overline{R}_g/\sigma$  for linear and cyclic polymers are, respectively, 1.44(1), 1.14(1) for  $N_b = 10$ , and 5.25(1), 3.72(1) for  $N_b = 100$ , as it is also reported in Table 4.3. We

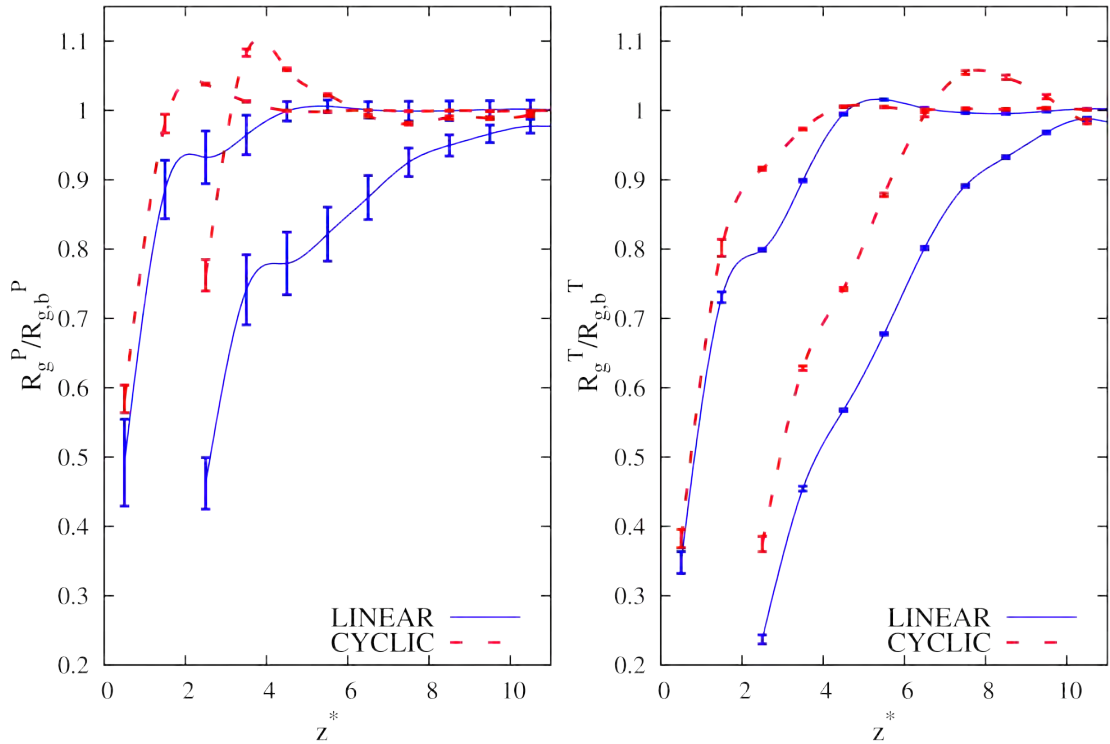


Figure 4.9: Left panel: Parallel component of the radius of gyration  $R_g^P$  as a function of the distance from the interface for linear (full line) and cyclic polymers (dashed line).  $R_g^P$  is scaled by its *bulk* value  $R_{g,b}^P$ . Pair of curves starting at  $z^* = 0.5$  are for  $N_b = 10$ ; pair of curves starting at  $z^* = 2.5$  are for  $N_b = 100$ . Right panel: same as in the left panel for the transverse component  $R_g^T$  as a function of the distance from the interface.

observe again that the polymers always fold as they get closer to the interface. The short-chain case (see the pair of curves in the two panels of Figure (4.9) beginning at  $z^* = 0.5$ ) does not show a significant difference between the two polymer species and the consistent lower values of  $\overline{R_{g\perp}}$  nearby the interface suggest that the two polymers get more folded along the direction transverse to the interface. However, for the long-chain case (see the pair of curves in the two panels of Figure 4.9 beginning at  $z^* = 2.5$ ) the evidence is that linear polymers get more folded than cyclic polymers at the interface, with a bigger squeezing of their shape along the transverse direction than cyclic polymers. In this case, cyclic polymers fail to fold significantly along the directions parallel to the interface. These results provide evidence of a higher loss of conformational entropy of linear polymers at the interface, indirectly supporting the cyclic chain enhancement at the interface for long chains as the result of the likely higher values of conformational entropy achieved by them at the interface in comparison to linear polymers. It is interesting to note that a more swollen shape along the directions parallel to the interface was observed very recently in systems of pure cyclic chains [55], and it was explained in terms of the topological excluded volume interaction

Table 4.2: Values of radii of gyration  $Rg$  of linear and cyclic com chains.

Chain length	Concentration=0.2					
	Linear chain com			Cyclic chain com		
	$Rg_{3D}$	$Rg_{  }$	$Rg_{\perp}$	$Rg_{3D}$	$Rg_{  }$	$Rg_{\perp}$
7-mers	1.169	0.653	0.640	0.930	0.534	0.524
10-mers	1.446	0.807	0.794	1.141	0.654	0.641
20-mers	2.140	1.199	1.182	1.659	0.949	0.936
30-mers	2.678	1.489	1.469	2.037	1.161	1.160
50-mers	3.521	1.971	1.960	2.701	1.570	1.477
100-mers	5.074	2.849	2.762	3.681	2.108	2.080

(repulsion) of blobs in a ring, that prevents other rings to be tangled. We also verified explicitly the existence of such repulsion between cyclic chains at the interface by calculating the average cyclic-cyclic energy per bead and finding a positive value for the energy (see section about energy calculations reported later). Consistently, we observed that this repulsion diminished for longer chains because the more swollen cyclic shape in the directions parallel to the interface favours self interactions among cyclic polymers, eventually contributing to their enhancement nearby the interface. These results show that linear polymers get better squeezed at the interface in the long-chain case, which means that they lose a considerable amount of conformational entropy in this case. On the contrary, in the 10-mers case their loss of conformational entropy is less than the one of cyclic chains, which explain the reason why linear chains get preferentially adsorbed at the interface for short-chains, while cyclic chains get preferentially adsorbed in the long-chain case. Then, our results suggest that the process bringing linear polymers to the interface is driven by the entropy, even though there are evident enthalpic reasons which also play a role in the long-chains case because linear polymers in the bulk possess a larger energy per bead as compared to cyclic polymers due to their higher flexibility (see the section discussing the energy of the two polymer species). For the 10-beads case (left panel of the Figure) we observe a similar drop of the average radius of gyration for both cyclic and linear chains starting from the bulk and going toward the interface. Both the radii of gyrations drop down to nearly half of the bulk radius of gyration nearby the interface. Cyclic polymers seem to have a slightly smaller radius of gyration than linear polymers at the interface. In the 100-mers case (see the right panel of the Figure), we observe that similarly as for 10 beads, the drop becomes evident when we are at a distance of the order of the radius of gyration from the interface. However, the linear polymers exhibit a noticeable bigger drop in the radius of gyration at the interface than the cyclic polymers.

We conclude this section by looking at the way the square of the radius of gyration scales

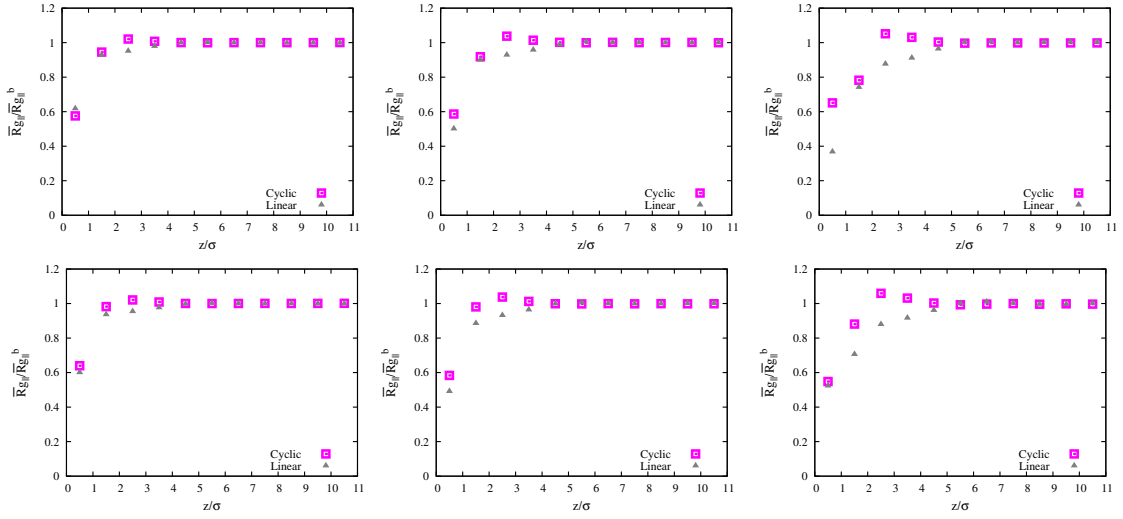


Figure 4.10: Average parallel component of the radius of gyration of free-standing films made of 7-mers (leftmost panels), 10-mers (middle panels), and 20-mers (rightmost panels) chains at low cyclic concentrations:  $c^0 = 0.8$  (top panels) and  $0.7$  (bottom panels).

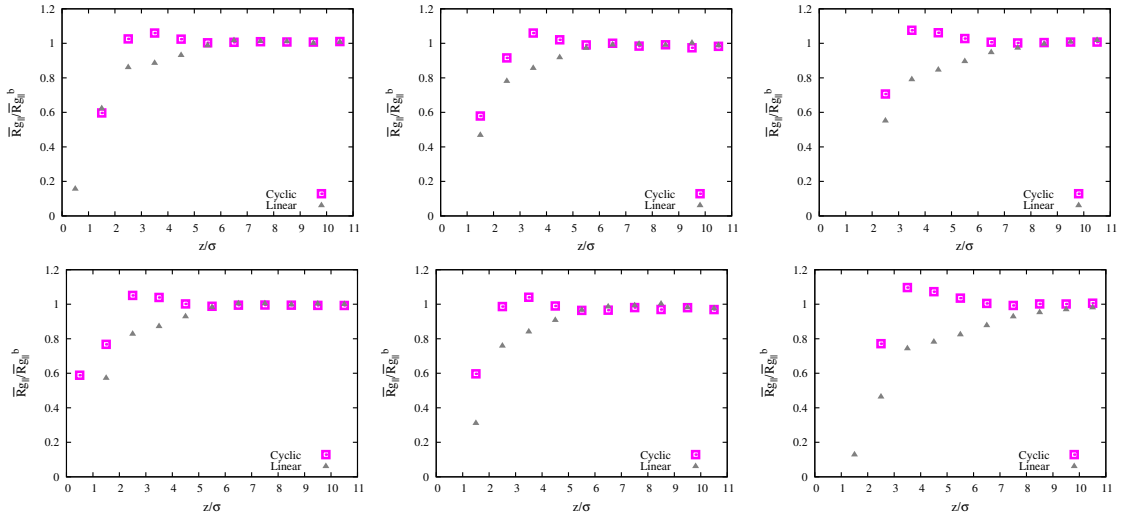


Figure 4.11: Average parallel component radius of gyration of free-standing films made of 30-mers (leftmost panels), 50-mers (middle panels), and 100-mers (rightmost panels) chains at low cyclic concentrations:  $c^0 = 0.8$  (top panels) and  $0.7$  (bottom panels).

with the chain length for cyclic chains. The interest into this feature is due to the fact that it was recently demonstrated [39] that some topological properties of cyclic chains, including non-knotting and nonconcatenation lead to a peculiar way the square of gyration of cyclic polymers scale with the degree of polymerization. At short-chain lengths (like the ones we consider in our thesis, n.b. even if we distinguish between short and long chain cases for the sake of illustration, the range of chain lengths we investigated belongs in general to the short chain regime), rings are found to be approximately Gaussian. This regime is associated with the scaling  $R_g^2 \propto N^{2\nu}$  and  $\nu = 1/2$ . For

Table 4.3: Values of radii of gyration  $Rg$  of linear and cyclic com chains.

Chain length	Concentration=0.3					
	Linear chain com			Cyclic chain com		
	$Rg_{3D}$	$Rg_{  }$	$Rg_{\perp}$	$Rg_{3D}$	$Rg_{  }$	$Rg_{\perp}$
7-mers	1.168	0.653	0.638	0.930	0.533	0.524
10-mers	1.445	0.809	0.794	1.141	0.655	0.641
20-mers	2.133	1.194	1.178	1.651	0.949	0.924
30-mers	2.678	1.498	1.472	2.037	1.171	1.137
50-mers	3.520	1.996	1.977	2.646	1.528	1.462
100-mers	5.238	2.930	2.902	3.662	2.093	2.071

longer chains the value  $\nu = \frac{2}{5}$  is expected instead and found in theoretical [38], numerical [33, 35], and experimental [87] works. A smooth crossover from the Gaussian to the regime with  $\nu = \frac{2}{5}$  was found in Ref. [39], when the length of the rung exceeds a few entanglement lengths. When the chain length is far greater than a few entanglement lengths, a conformational transition bringing the cyclic polymers to assume a globular shape is expected, and  $\nu = \frac{1}{3}$ . In Figure 4.12, we report the way the exponent  $\nu$  varies for the system sizes we have considered as a function of the distance from the interface. We find that in the *bulk* regime, far from the interface, our chains exhibit Gaussian behaviour, in agreement with what was found in the literature [39]. However, when the distance to the interface decreases, we observe a smooth transition to lower values for  $\nu$  (see left panel of Figure 4.12). The value that is going to be for  $\nu$  at the interface is not clear since when we approach the interface the density decreases and the quality of our statistical data deteriorates. On the right panel we demonstrate that by excluding the data for  $Nb = 100$  at  $z^* = 2.5$  in the evaluation of the exponent. A good reason for doing that is because for that chain length you observe the first meaningful result for  $R_g$  exactly at 2.5, that could possibly make its usage unfair.

### 4.3.3 Instantaneous Interface

Now we try to use the approach discussed in the Methods section in order to avoid the bias of not having a flat interface separating the empty space from the polymer blend. The very first thing we would like to understand is whether the approach calculating particle histograms starting from the instantaneous interface is able to provide us with a different evidence as related to linear or cyclic chain enhancement at the interface. For this reason, we started targeting the two different polymer species and we reported the related histograms as a function of the distance from the instantaneous interface in Figures 4.13 - 4.14. At short chains lengths, we clearly saw that linear polymers are still preferentially absorbed at the interface (see Figure 4.13). However, especially at

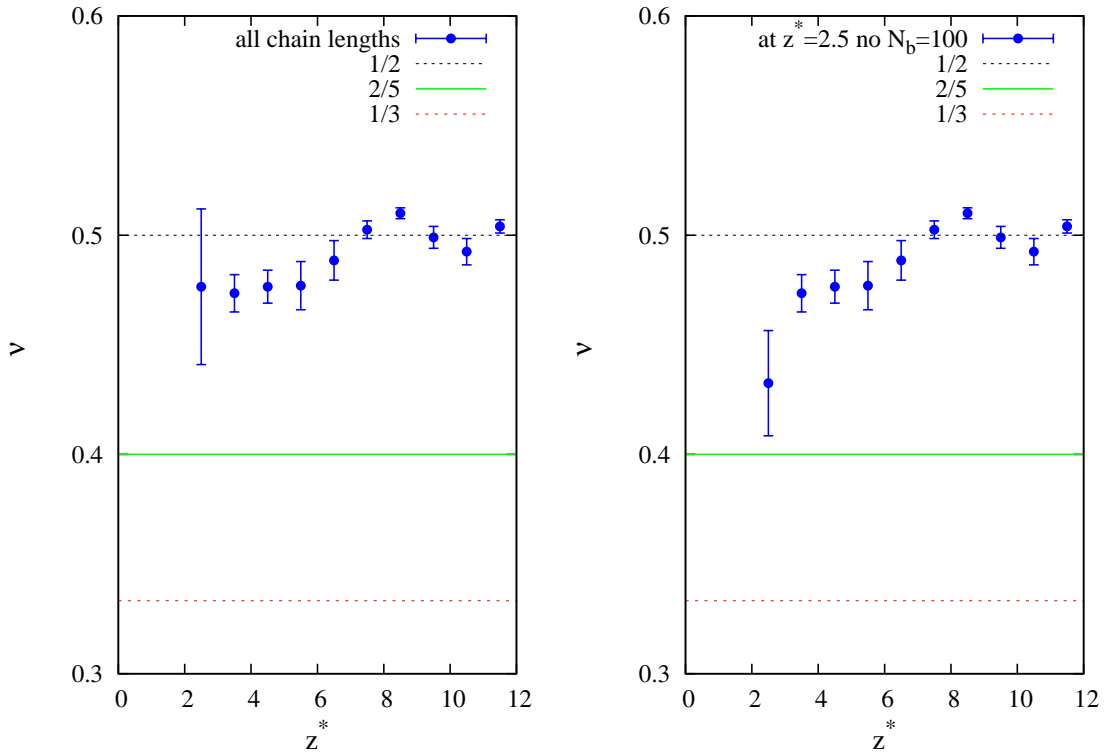


Figure 4.12: Left panel: Exponent of the mean square radius of gyration  $R_g^P$  as a function of the distance from the interface for cyclic polymers at composition  $c_0 = 0.7$ . Left panel corresponds to the estimate performed by using all the chain lengths. Right panel corresponds to the case where at  $z^* = 2.5$ , the case  $N_b = 100$  was excluded.

the composition where cyclic polymers are more dense (see bottom panels), we note that as the chain length increases, the difference between the percentage of the two polymer species becomes very narrow. When we look at the higher chain lengths (see Figure 4.14), this regime of overlap between the percentages of the two polymer species at the interface persists, and eventually when the chain length becomes very high (see right panels), we found that cyclic polymers get more adsorbed at the interface. It is interesting to note that the threshold for passing from the linear enhancement to the cyclic one when using the standard approach was between  $N_b = 30 - 50$  beads per polymer (see Table 4.1), while the one predicted by our calculations based on the instantaneous interface is now between  $N_b = 50 - 100$  beads per polymer. Another aspect emerging from the visualization of the figures is that the concentration of cyclic polymers is generally subject to higher fluctuations as we move far away from the interface in the case of longer chain lengths (see Figure 4.14).

Before understanding the reason why we made the subsequent calculation, we have to consider that we did not provide so far any explanation of the enhancement at the interface of linear polymers for short chains. According to the GFT [42], when the monomer density profile is dominated by

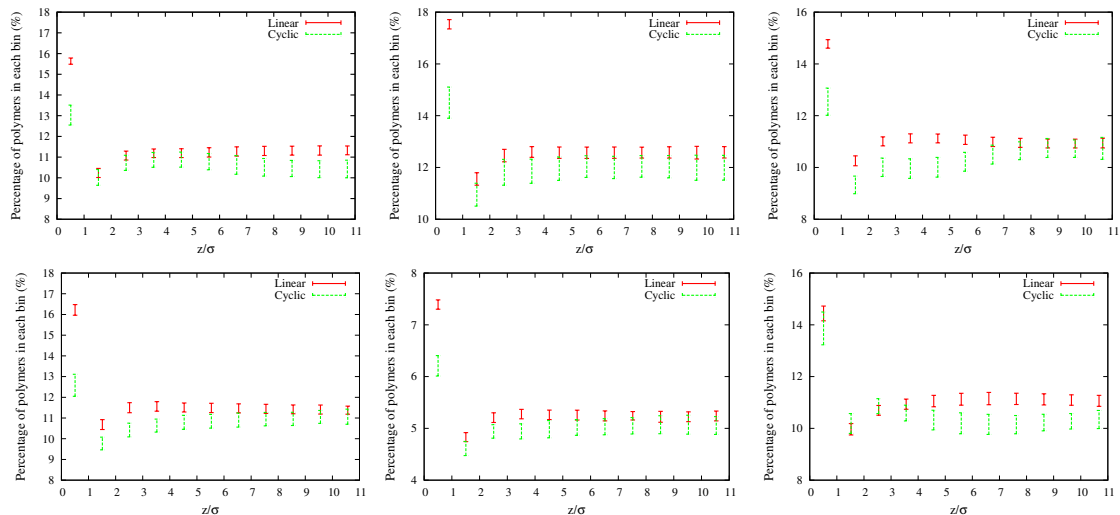


Figure 4.13: Average percentage number of polymer species made of 7-mers (leftmost panels), 10-mers (middle panels), and 20-mers (rightmost panels) chains at low cyclic concentrations:  $c^0 = 0.8$  (top panels) and 0.7 (bottom panels).

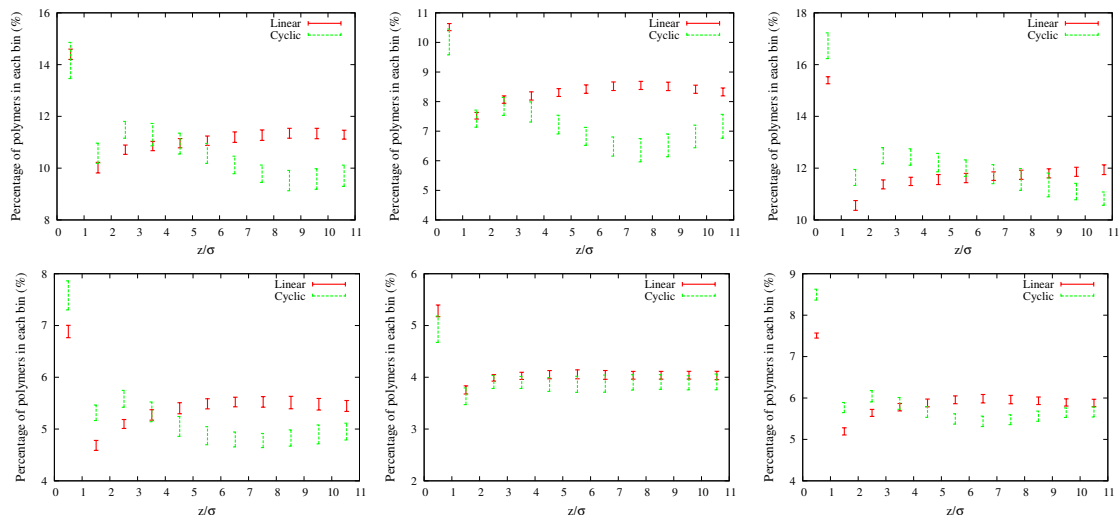


Figure 4.14: Average percentage number of polymer species made of 30-mers (leftmost panels), 50-mers (middle panels), and 100-mers (rightmost panels) chains at low cyclic concentrations:  $c^0 = 0.8$  (top panels) and 0.7 (bottom panels).

linear chains (as in the present case where we consider low compositions of cyclic polymers), it is possible to show within linear response theory that these profiles are precisely produced by attractive surface potentials of entropic origin for chain-ends. The real existence of these potentials of entropic origin was demonstrated very recently by neutron reflectometry and Raman spectroscopy measurements performed on linear and branched polymer blends of PMMA [13]. In order to detect the presence of chain-ends of linear polymers at the interface, we had then to eliminate the bias of not having a clear flat, planar interface separating the polymer mixture from

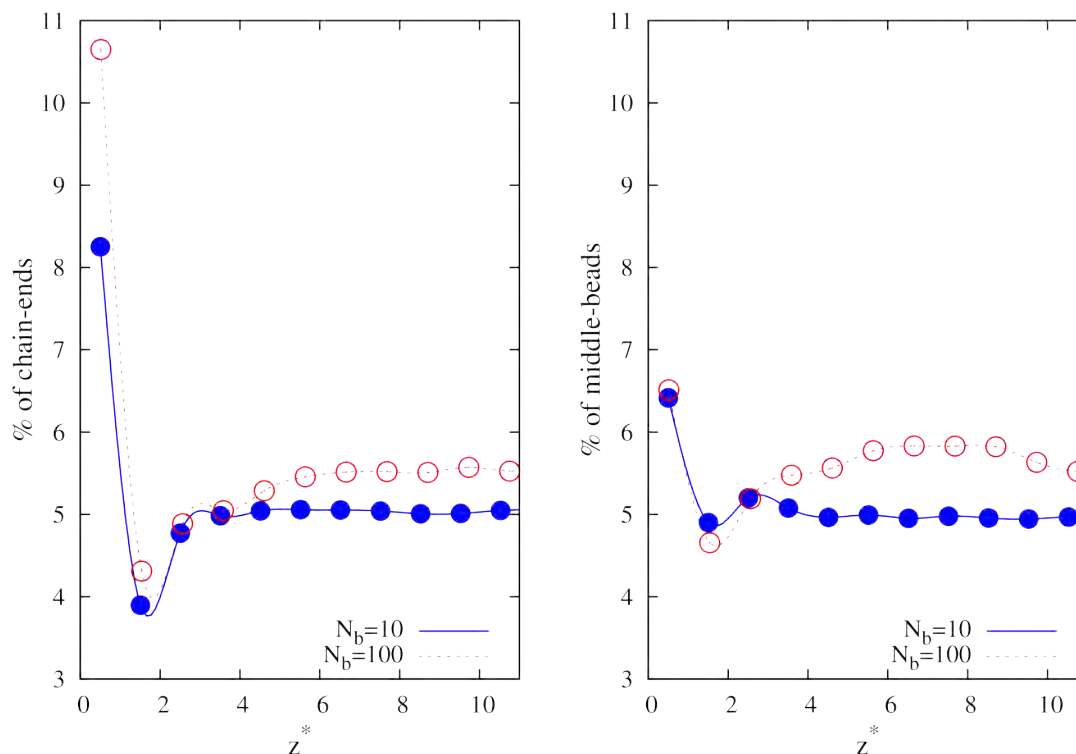


Figure 4.15: Left panel: histogram of the percentage of chain-ends of linear polymers as a function of the distance from the interface. Right panel: same as in the left panel for the percentage of middle-beads of linear polymers.

the empty space. This is the main reason we tried to look at the position of these chain-ends by using the procedure based on the instantaneous interface. Chain-ends as a function of the distance from the instantaneous interface are reported in Figures 4.17 - 4.18. As a general comment, we note that for both the compositions under scrutiny the number of chain-ends at the interface tends to become higher with the chain length, even if the trend does not look as a monotonic one. In the same Figures, we also targeted the middle beads of linear chains in order to have a clear reference for the observed enhancement of chain-ends. The evidence is that the percentage of middle beads at the interface is always smaller than the percentage of chain-ends.

In order to provide the reader with a more clear comparison between the short- and long-chain chases, we reported on the right panel of Figure 4.15 the percentage of chain-ends of linear polymers as a function of the distance from the instantaneous interface for the cases  $N_b = 10, 100$ . The comparison confirms a clear enhancement of the number of chain-ends at the interface with respect to the *bulk*, no matter of the degree of polymerization. Thus, in the short chain case we can explain the previously observed enhancement of the composition of linear polymers in terms of the existence of an entropic mechanism due to the chain-ends getting preferentially adsorbed at the interface. Although the percentage of chain-ends reported in Figure 4.15 is even larger

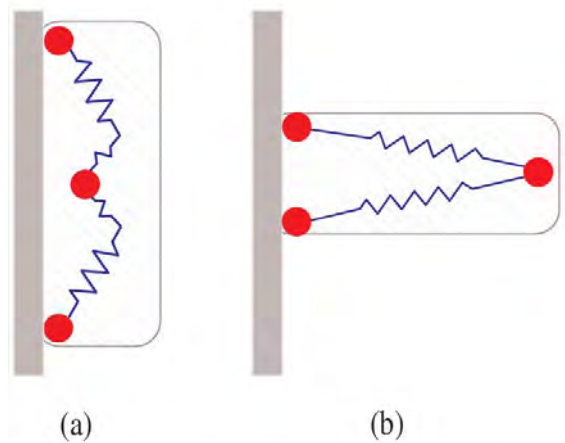


Figure 4.16: (a): Sketch of a configuration for a linear polymer with chain-ends attached to the interface and middle bead close to the interface. (b): same as in (a) for the case in which the middle bead is far away from the interface.

for the long chain case, the entropic contribution originating from their presence does not likely have a sufficient magnitude to overcome the loss of conformational entropy of linear polymers (see the small values achieved by the  $R_g$  components of linear polymers reported in Figure 4.9. In the long chain case, the competition of these two different entropic terms favours cyclic polymers enrichment at the interface. In the right panel of Figure 4.15, we targeted again the middle beads of linear chains and not surprisingly we found that their percentage number is also slightly enhanced. In fact, by looking at Figure 4.9 we note that the parallel component of the radius of gyration of linear polymers nearby the interface is always larger than the transverse component, which is indicative of linear polymers assuming a more swollen shape along the directions parallel to the interface. This configuration is compatible with the geometry sketched on Figure 4.16; (a), where middle beads of linear polymers tend to stay closer to the interface.

#### 4.3.4 Diffusion coefficients

In this section, we analyze the diffusion of the center-of-mass (com) of polymer chains as a function of the distance from the interface. In general, the diffusion coefficient of a homogeneous system is computed as the slope of the mean-square displacement (MSD) of the coms as a function of the time interval. In fact, when sufficiently long time intervals are considered the ballistic regime is avoided and the system is in the linear regime. In this case, the MSD and the diffusion coefficient are linked by the Einstein relation:

$$\langle \Delta r(t)^2 \rangle = dDt, \quad (4.8)$$

where  $d$  is a coefficient whose value depends on the dimensionality of the system:  $d = 6, 4, 2$  for a three-dimensional (3D), a two-dimensional, and a one-dimensional system. We are interested

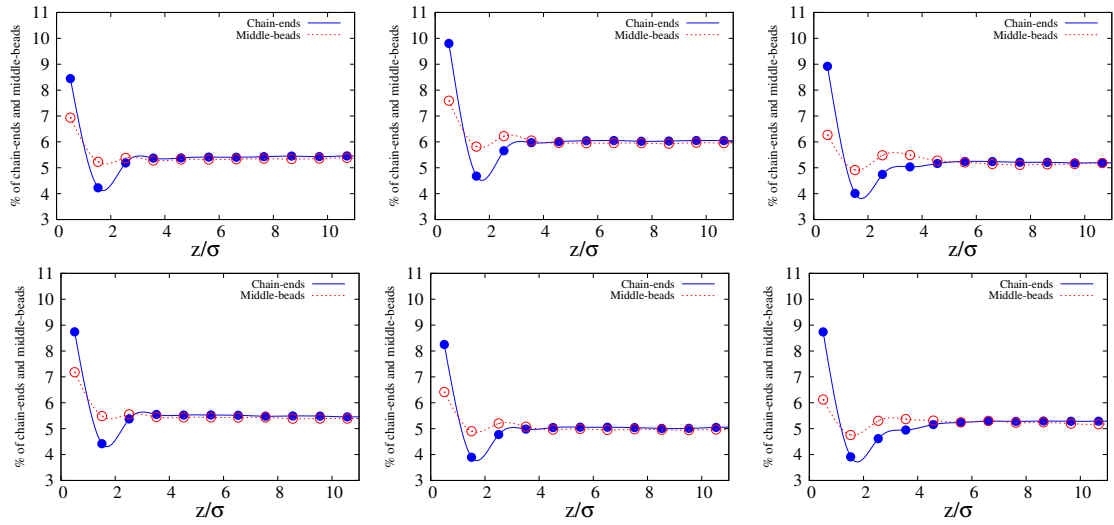


Figure 4.17: Average percentage number of chain-ends and middle points of linear polymers made of 7-mers (leftmost panels), 10-mers (middle panels), and 20-mers (rightmost panels) chains at low cyclic concentrations:  $c^0 = 0.8$  (top panels) and 0.7 (bottom panels).

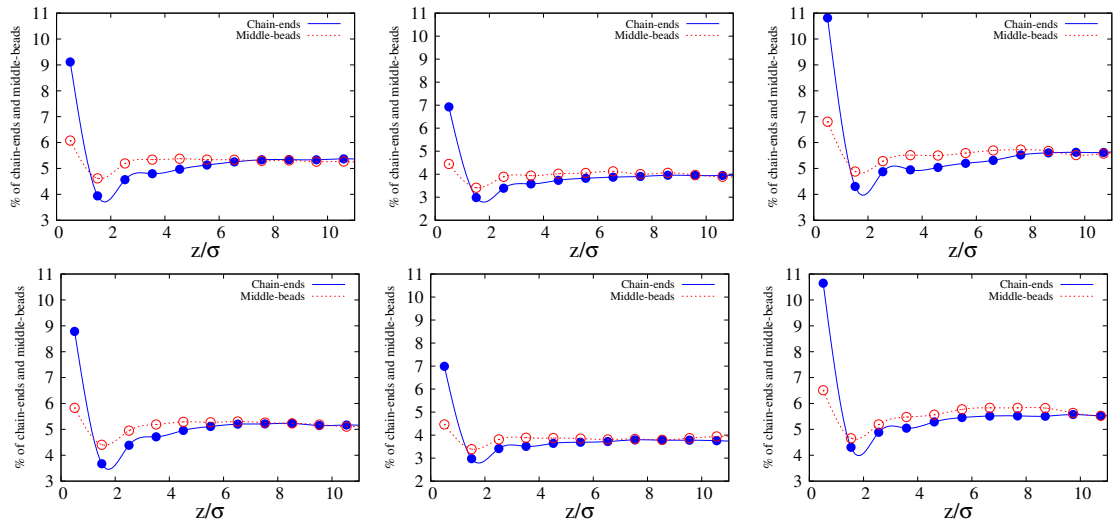


Figure 4.18: Average percentage number of chain-ends and middle points of linear polymers made of 30-mers (leftmost panels), 50-mers (middle panels), and 100-mers (rightmost panels) chains at low cyclic concentrations:  $c^0 = 0.8$  (top panels) and 0.7 (bottom panels).

in looking at the two different components of the 3D diffusion coefficient, which inform us about the mobility of polymer species in the directions perpendicular (transverse) and parallel to the interface. Similarly as for the radius of gyration, these two components are easily defined in terms of the geometry of the parallelepiped simulation box since the interface was generated along the  $x$ - $y$  plane. However, since we are interested in looking at the diffusion coefficient as a function of the distance from the interface, the MSD must be calculated accordingly. Then if we let  $\Gamma(t, t + \tau)$  designate the set of all particles that stay in the layer  $\{a, b\}$  during the time interval between  $t$

Table 4.4: Values of diffusion coefficient in the bulk of linear and cyclic com chains computed from the slope of MSD in the linear regime using Einstein relation.

Concentration=0.3						
Chain length	Linear chain com			Cyclic chain com		
	$D_{\text{bulk}}^{3D}$	$D_{\text{bulk}}^{\parallel}$	$D_{\text{bulk}}^{\perp}$	$D_{\text{bulk}}^{3D}$	$D_{\text{bulk}}^{\parallel}$	$D_{\text{bulk}}^{\perp}$
7-mers	0.310	0.310	0.310	0.157	0.157	0.158
10-mers	0.201	0.201	0.202	0.105	0.105	0.104
20-mers	0.089	0.089	0.089	0.066	0.050	0.098
30-mers	0.056	0.054	0.056	0.042	0.031	0.065
50-mers	0.034	0.035	0.033	0.025	0.018	0.040
100-mers	0.017	0.018	0.016	0.011	0.011	0.010

and  $t + \tau$ , and  $N(t)$  the number of particles in the layer at time  $t$ , the transverse  $\langle \Delta r(\tau)^2 \rangle_{\{a,b\}}^T$  and parallel  $\langle \Delta r(\tau)^2 \rangle_{\{a,b\}}^P$  MSDs in the bin  $\{a, b\}$  (whose size we keep to  $\sigma$ ) along the  $z$ -direction can be calculated as:

$$\langle \Delta r(\tau)^2 \rangle_{\{a,b\}}^T = \frac{1}{T} \sum_{t=1}^T \frac{1}{N(t)} \sum_{i \in \Gamma(t, t+\tau)} (z_i(t+\tau) - z_i(t))^2, \quad (4.9)$$

where  $T$  is the total number of time steps, and

$$\langle \Delta r(\tau)^2 \rangle_{\{a,b\}}^P = \frac{1}{T} \sum_{t=1}^T \frac{1}{N(t)} \sum_{i \in \Gamma(t, t+\tau)} [(x_i(t+\tau) - x_i(t))^2 + (y_i(t+\tau) - y_i(t))^2]. \quad (4.10)$$

In Figure 4.21, we report only a few MSDs for the composition  $c^0 = 0.7$  and for  $N_b = 10, 30, 100$  for demonstrating that a decent linear behaviour is found for them in a reasonably long time interval. The data are reported for both the transverse and parallel MSDs for bins nearby (Surface parallel and transverse) and far from the interface (Bulk parallel and transverse). In general the parallel MSD as calculated nearby the interface (Surface) is the one that grows the quickest and quicker than the corresponding transverse component. The parallel MSD as calculated far from the interface (Bulk) is also generally growing faster than the corresponding transverse component, with the exception of the case  $N_p = 0.3$  where they assume similar values.

The parallel components of the diffusion coefficient as a function of the distance from the interface are reported in Figures 4.22-4.23. Also in this case, the diffusion coefficients are scaled by their *bulk* counterparts as reported in Tables 4.4-4.5. Generally, we see that the diffusion of the two polymer species increases as they get closer to the interface from the *bulk*. This feature is easily understood since our system is exposed to a empty space, and we know that as the interface is approached the density profile tends to drop to zero (see Figures 4.2-4.3). However, when the

Table 4.5: Values of diffusion coefficient in the bulk of linear and cyclic com chains computed from the slope of MSD in the linear regime using Einstein relation.

Concentration=0.2						
Chain length	Linear chain com			Cyclic chain com		
	$D_{\text{bulk}}^{3D}$	$D_{\text{bulk}}^{\parallel}$	$D_{\text{bulk}}^{\perp}$	$D_{\text{bulk}}^{3D}$	$D_{\text{bulk}}^{\parallel}$	$D_{\text{bulk}}^{\perp}$
7-mers	0.313	0.314	0.312	0.161	0.163	0.158
10-mers	0.205	0.214	0.187	0.107	0.112	0.098
20-mers	0.089	0.090	0.089	0.048	0.048	0.048
30-mers	0.056	0.056	0.055	0.030	0.031	0.029
50-mers	0.032	0.032	0.031	0.017	0.018	0.016
100-mers	0.018	0.019	0.016	0.010	0.009	0.010

interface is very close (i.e. different chain length and composition) we observe in most of the cases a dramatic drop of the diffusion coefficient. In some cases, we observe a drop that is not as dramatic with the diffusion coefficients being still higher than the *bulk* value. What emerges is that for the lower degrees of polymerization (see Figure 4.22) the cyclic polymers tend to have a smaller enhancement of their parallel diffusion as the interface is approached, and very close to the interface their parallel mobility is lower or similar to the one of linear polymers. This result is compatible with what we observed in the left panel of Figure 4.9, where for small  $N_b$  the two polymer species exhibit a similar folding of their shape along the interface (the percentage decrease of their parallel component of the radius of gyration with respect to the *bulk* case is similar). Moreover, since cyclic polymers tend to increase their size a bit along the parallel directions to the interface as the interface is approached, the higher growth of the mobility of linear polymers reported in Figure 4.22 is also better understood. When we look at the higher degrees of polymerization (see Figure 4.23), the feature that is worth of note is that when we increase the chain length the parallel mobility drop of linear polymers with respect to the *bulk* near the interface becomes eventually bigger than the one of cyclic chains, although the mobility of both polymer species remains higher than the one far from the interface. This result should be analyzed by also looking at the right panel of Figure 4.9, where we observed that the parallel-to-the-interface dimension of linear polymers shrinks far more than the corresponding one for cyclic polymers nearby the interface. The picture is complete when we also remember that in the case of long chains, the local composition of linear polymers is depleted with respect to the *bulk* value (see Figure 4.5). In other words, at the interface there are now less linear polymers than far from the interface and they are more squeezed along the interface. This local population of linear polymers is then moving less quickly along the same directions it is more folded, and it is mixed with a local population of cyclic polymers that did

not change its shape much in comparison to the *bulk* case. Finally, this local population of cyclic polymers is higher than the one far from the interface (the local composition of cyclic polymers is enhanced with the respect to the expected *bulk* value of  $1 - c^0 = 0.7, 0.7$ ). We note that especially for longer chains it becomes difficult to get enough statistical data closer to the interface since the com of polymers is likely to be found at distances higher than the chosen bin size for the histograms ( $\sigma$ ). This issue also arose when considering the radius of gyration in proximity of the interface for long chains (see Figure 4.11).

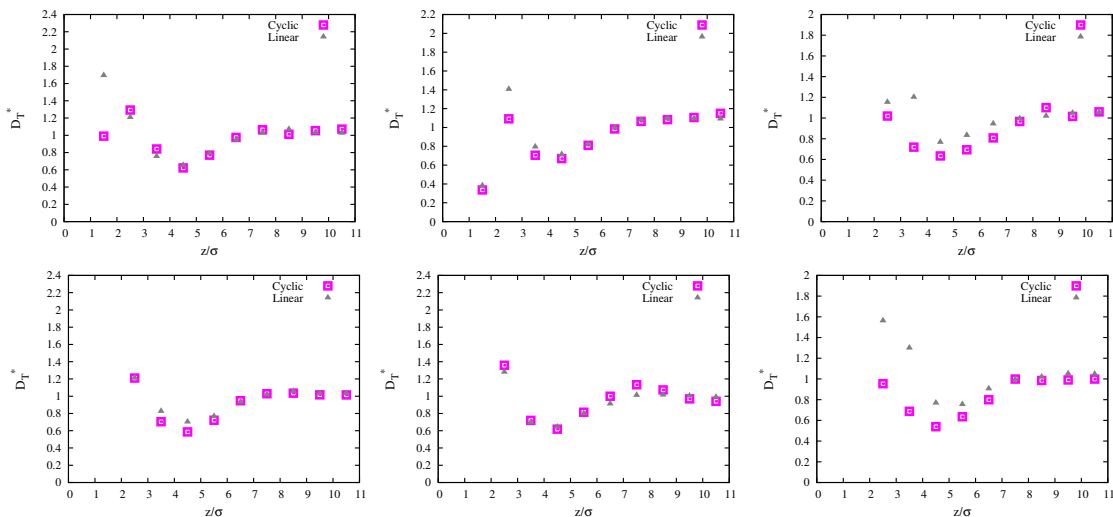


Figure 4.19: Transverse component of the diffusion coefficient as a function of distance from the surface for polymer species made of 30-mers (leftmost panels), 50-mers (middle panels), and 100-mers (rightmost panels) chains at low cyclic concentrations:  $c^0 = 0.8$  (top panels) and  $0.7$  (bottom panels).

When we look at the mobility of polymer species in the direction perpendicular to the interface in Figures 4.20 - 4.19, we observe that in general cyclic polymers tend to have a similar mobility as the linear ones, besides when the interface is approached: in this case cyclic polymers appear to have a similar or a smaller transverse mobility than linear ones. Another feature worth of consideration is the minimum in the transverse diffusion observed for both the two polymer species at a range of distances that seems quite unaltered when different degrees of polymerization are used:  $4\sigma - 6\sigma$ . A possible explanation of this feature can be found in a close observation of Figures 4.4 - 4.5. In fact, we note that the deviation of the local composition from the respective *bulk* values for the two polymer species begins roughly over the same range of distances from the interface. Then, we might argue that the system manages to maintain its *bulk* composition until a distance of  $4\sigma - 6\sigma$  to the interface is reached, *by decreasing the transverse diffusion coefficient with respect to the corresponding bulk value. However, when the distance to the interface becomes eventually very small, the presence of the interface (empty space) cannot be ignored anymore and the diffusivity of both polymer species starts increasing again.*

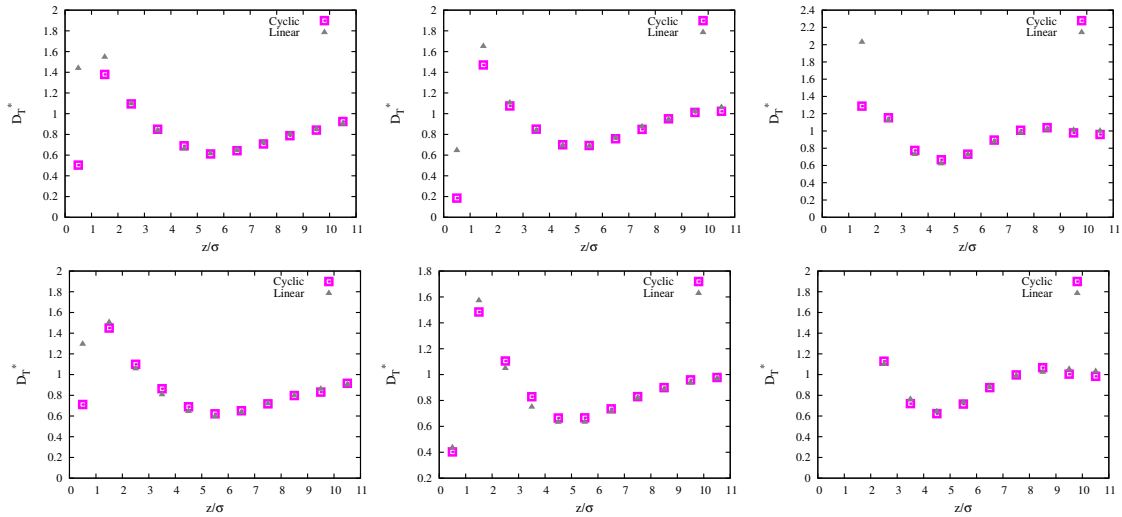


Figure 4.20: Transverse component of the diffusion coefficient as a function of distance from the surface for polymer species made of 7-mers (leftmost panels), 10-mers (middle panels), and 20-mers (rightmost panels) chains at low cyclic concentrations:  $c^0 = 0.8$  (top panels) and  $0.7$  (bottom panels).

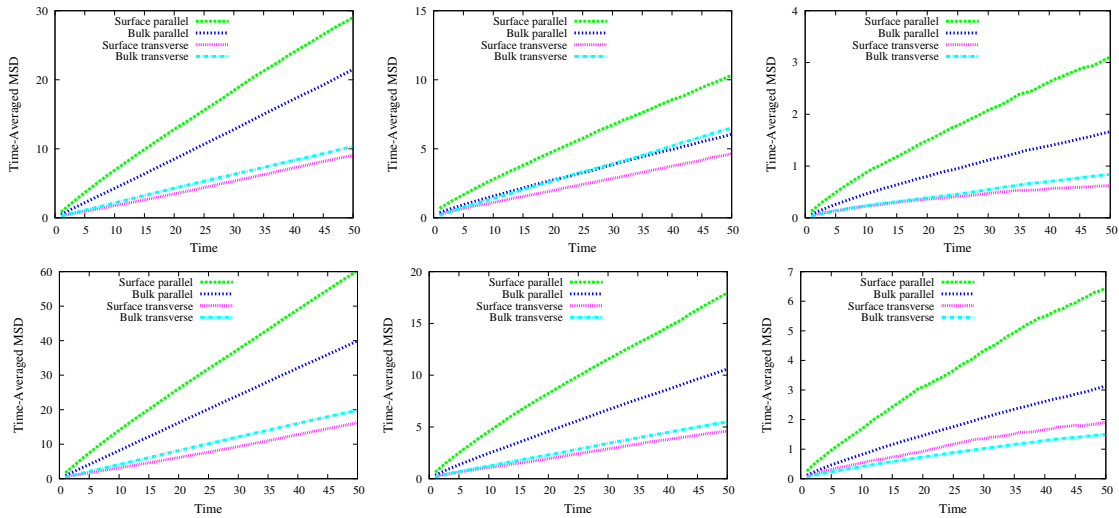


Figure 4.21: Time-averaged components of the mean square displacement of cyclic (top) and linear (bottom) chains as a function of time for different blend regions as reported in the legend. Thickness of the selected region is  $\sigma$ . Results are shown for  $N_b = 10$  (left panels),  $30$  (middle panels) and  $100$  (right panels) at  $c^0 = 0.7$ . *Time* is in units of  $10^4$  timesteps.

### 4.3.5 Interaction Energies of polymer species

In this section we focus on the interaction energy among polymer beads. We remind that in our model polymer beads are interacting via the Lennard-Jones  $12 - 6$  pair potential, and that the energy parameters we selected for the study of this section are the same for both linear and cyclic

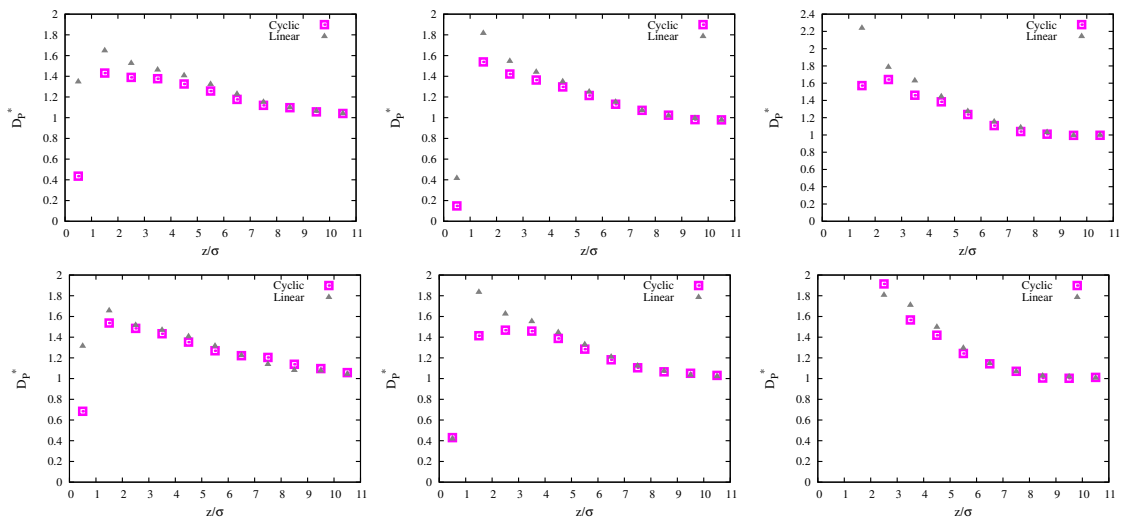


Figure 4.22: Parallel component of the diffusion coefficient as a function of distance from the surface for polymer species made of 7-mers (leftmost panels), 10-mers (middle panels), and 20-mers (rightmost panels) chains at low cyclic concentrations:  $c^0 = 0.8$  (top panels) and 0.7 (bottom panels).

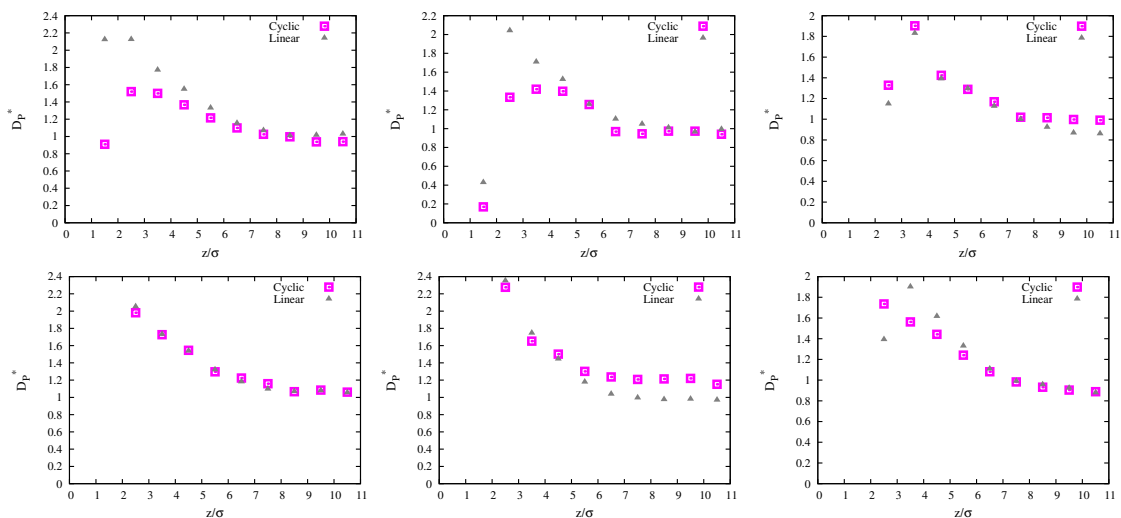


Figure 4.23: Parallel component of the diffusion coefficient as a function of distance from the surface for polymer species made of 30-mers (leftmost panels), 50-mers (middle panels), and 100-mers (rightmost panels) chains at low cyclic concentrations:  $c^0 = 0.8$  (top panels) and 0.7 (bottom panels).

chains. Thus, there is no preferential enthalpic contribution favouring self-interactions between polymer beads belonging to the same species, or crossed interactions between polymer beads belonging to different species. In other words, any effect as related to mixing or separation in the blend is not driven by the energy but if detected, it is genuinely triggered by the different topology of the two polymer species.

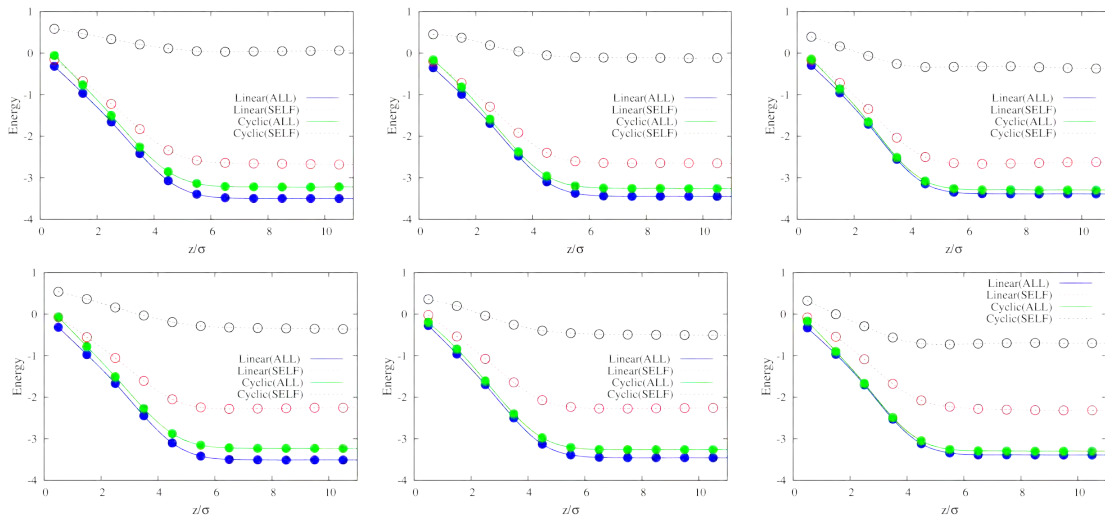


Figure 4.24: Energy per bead of different polymer species as a function of distance from the surface for polymer species made of 7-mers (leftmost panels), 10-mers (middle panels), and 20-mers (rightmost panels) chains at low cyclic concentrations:  $c^0 = 0.8$  (top panels) and 0.7 (bottom panels). ALL refers to the energy per bead as calculated regardless of the nature of the bead. SELF refers to the energy per bead as calculated by considering beads belonging to the same polymer species only.

The energies per bead for the two polymer species are reported in Figures 4.24 - 4.25 as a function of the distance from the interface. In the Figures, we also report both the total energy per bead, that is calculated by considering all of the energy contributions originating from polymer beads of any species surrounding a generic bead of the selected species, and the self-energy per bead, that is calculated by taking into account only the surrounding beads belonging to the same species. Obviously self-energies per bead of cyclic polymers are less negative than those of linear polymers because we are considering the cases where the composition of linear polymers is greater than 0.5, so there are more linear polymers in the simulation box. The first thing we note is that the self-energy of cyclic polymers tends to decrease with the increase of the molecular mass (chain length) of the polymers. However, the self-energy of linear polymers remains almost unaltered with the increase of  $N_b$ . If we look at the total energy per bead, we note that it remains almost unchanged when we increase the degree of polymerization, and that its values are also very similar across the two polymer species. The reason for that is: we expect the local environment of beads (i.e. the number of neighbouring beads and the distribution of their distances from any targeted bead) to be very similar regardless of the targeted polymer species, if the system stays in a homogeneous phase. However, this is not the case when we consider the short-chains, in fact the total energies per bead of the two species tend to be more different as we decrease the chain length (see Figure 4.24), with the total energy per bead of cyclic polymers becoming less and less attractive than the one of linear polymers. This feature is evidently triggered by what we already noted before: cyclic chains tend

to have a more attractive self-energy as we increase the chain length. In other words, as we decrease  $N_b$ , the self-energy of cyclic polymers become less and less attractive, driving the total energy per bead of cyclic polymers to drift far apart the total energy per bead of linear polymers. This effect is clearly driven by the loop topology of cyclic chains, which generates a geometrical constraint on cyclic molecules preventing them from packing against each other effectively as linear chains. In fact, the globular shape of cyclic chains is particularly evident at low degrees of polymerization, and its compactness prevents beads of different cyclic molecules to stay close to each other as effectively as the ones of linear polymers. *More importantly, in this limit a single cyclic chain will have a considerably less chance to fold onto itself as efficiently as a linear polymer so to increase the number of contacts between non-consecutive beads belonging to it, even if the extent they fold is similar to the one of linear chains. We remind that for short chains we noted that linear and cyclic chains at the interface appear to fold similarly, as reported in Figure 4.9. Our findings highlight that the better ability of linear chains to pack onto chains of the same species so to minimize their self-energy is an especially important factor when we consider short chain lengths. This energy gain of cyclic polymers at low degrees of polymerization is a genuine enthalpic effect, and it is also one of the factors which determine cyclic chain depletion at the interface (i.e. linear chain enhancement) for systems with small polymer mass.*

Cyclic polymers tend also to exhibit a minimum of the self-energy at intermediate distances from the interface ( $4\sigma$ - $5\sigma$ ), that becomes more evident when we increase the degree of polymerization. For all the systems, if we extrapolate the energy per bead at any distance from the interface so to take into account the fact we are considering the higher linear composition regime, we find that should cyclic polymers be in the same number as linear polymers they would have always a higher energy than the one of linear polymers. That means linear polymers tend to stay closer to each other than cyclic polymers, which is something intuitively understood if we consider that the linear topology, i.e. the higher flexibility of linear polymers, far from the interface allows linear chains to pack against each other better than cyclic chains. This is another enthalpic effect which tends to favour linear polymers far from the interface, since there they can minimize their self-energy more than cyclic polymers. However, to understand the reason why in the short-chain case this effect is not effective in favouring linear polymers at the interface we need to keep in mind our previous considerations, and take also into account the role of the conformational and chain-end entropy contributions discussed before.

The self-energy of cyclic beads is always repulsive close to the interface, while the one of linear beads is always negative with the exception of the case with the highest molecular mass and the lower linear composition. In general, we emphasize again that the self-energy of cyclic beads tends to become less repulsive near the interface when the molecular mass is increased. Overall, that makes the deviation between the self-energies of linear and cyclic chains at the interface larger for low degrees of polymerization and smaller for higher degrees of polymerization. This behaviour is

compatible with what we observed before, i.e. the composition of linear chains is enhanced with respect to the *bulk* case for short chains and the one of cyclic chains get enhanced instead in the case of long chains.

In order to draw some important conclusions about our analysis of the energy of the system, we focus on the total energy per bead and we make an interesting comparison between the short and long chain cases. In Figure 4.26 we show the total energy per bead of the two polymer species as a function of the distance from the interface for  $N_b = 10$  (left panel) and  $N_b = 100$  (right panel). The total energy per bead is higher for cyclic polymers across the whole range of distances from the interface when we consider the small chain case (see left panel of Figure 4.26). Since cyclic polymers are way less flexible than linear polymers at small degrees of polymerization, they pack less efficiently and achieve a less than optimal number of pair interactions among their beads. This comparison highlights the severe constraint imposed on the flexibility of cyclic polymers by the loop topology when their chain length is small. Then, linear polymers can achieve a lower interfacial free energy than cyclic polymers because they minimize their surface energy more than cyclic chains, while at the same time maximizing their entropy by exposing their chain-ends to the surface. In this scenario, linear enhancement at the interface at short chain lengths is the result of an entropy-mediated process, where also the enthalpy is playing an important role.

If we consider the long chain case, the first thing we observe is that the total energy per bead of the two polymer species becomes now very similar regardless of the distance from the interface (see right panel of Figure 4.26). This comparison clearly shows that when the chain lengths is long enough, the loop constraint becomes less important in undermining the flexibility of polymer chains. Cyclic polymers are now likely to achieve a lower interfacial free energy than linear polymers because they possess an higher conformational entropy (see Figure 4.26), while their surface energy is not that different than the one of linear chains. Then, cyclic enhancement at long chain lengths emerges as a genuine entropic process, driven once again by the loop geometry which prevents cyclic chains to fold at the interface as efficiently as linear chains.

### 4.3.6 Percolation

In this section, we try to analyze the percolation properties of the system. For this reason, we scanned the system configurations at different timesteps in order to spot the formation of clusters formed by the same polymer species. Two chains are considered to belong to the same cluster if the distance of at least two of their beads is less or equal to the distance of the minimum of the FENE potential. In other words, to identify clusters we look at polymers which are closer to each other less than the bonding distance between two consecutive beads belonging to the same chain. The quantity we were interested to calculate was the percentage of clusters starting from the interface and their percolation size into the *bulk* of the blend. We also looked at the average number of polymers these clusters were formed of. The detection of a cluster percolating from the

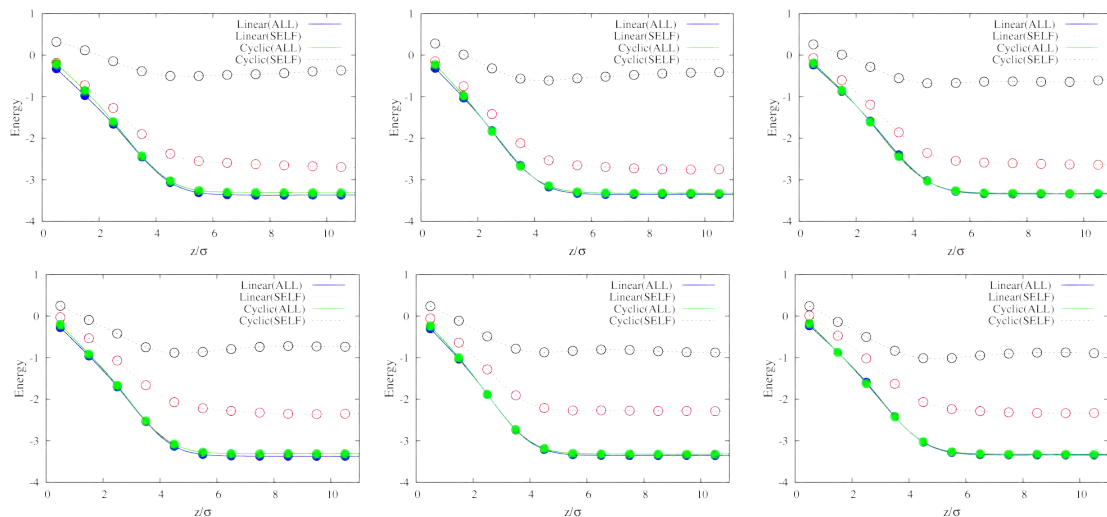


Figure 4.25: Transverse component of the diffusion coefficient as a function of distance from the surface for polymer species made of 30-mers (leftmost panels), 50-mers (middle panels), and 100-mers (rightmost panels) chains at low cyclic concentrations:  $c^0 = 0.8$  (top panels) and 0.7 (bottom panels). ALL refers to the energy per bead as calculated regardless of the nature of the bead. SELF refers to the energy per bead as calculated by considering beads belonging to the same polymer species only.

interface is made by looking at the  $z$ -coordinate of the polymer bead, which is located more distant from the interface. In order to locate unambiguously the clusters percolating from the interface we picked the smallest  $z$ -coordinate of the polymer beads belonging to the cluster, and we checked whether it was found within a distance equal to the radius of gyration from the bead belonging to the polymer with the smallest  $z$ -coordinate in the simulation box.

We start comparing the percolation properties of linear and cyclic polymers for small-intermediate chains in Figure 4.27 - 4.28. In the case of 7 beads per polymer, on the average we do not find clusters of more than one polymer for both the two polymer species. For  $N_b = 7, 20$  and in the case of linear polymers we have, respectively, a bit less than 5% and a bit more than 10% of clusters of at least two polymers which are percolating up to a distance of nearly  $8\sigma$ . In the case of cyclic polymers, the percolating distance is below  $4\sigma$  and for both the two degrees of polymerization  $N_b = 10, 20$  less than 5% of the clusters of nearly two polymers are reaching that distance. The lower percolating distances for clusters of cyclic chains represent a reasonable finding considering the comparatively smaller effective size of cyclic chains as compared to linear ones, as they were reported in the tables of the section of the radii of gyration. The smaller percentage of percolating cluster observed for cyclic chains seems a trivial consequence of the lower cyclic composition considered in Figure 4.27 instead of being an effect truly determined by the different topologies of the two polymers. Another feature emerging from this analysis of small-intermediate degree of polymerization is that we do not observe very large clusters starting from the interface, the biggest

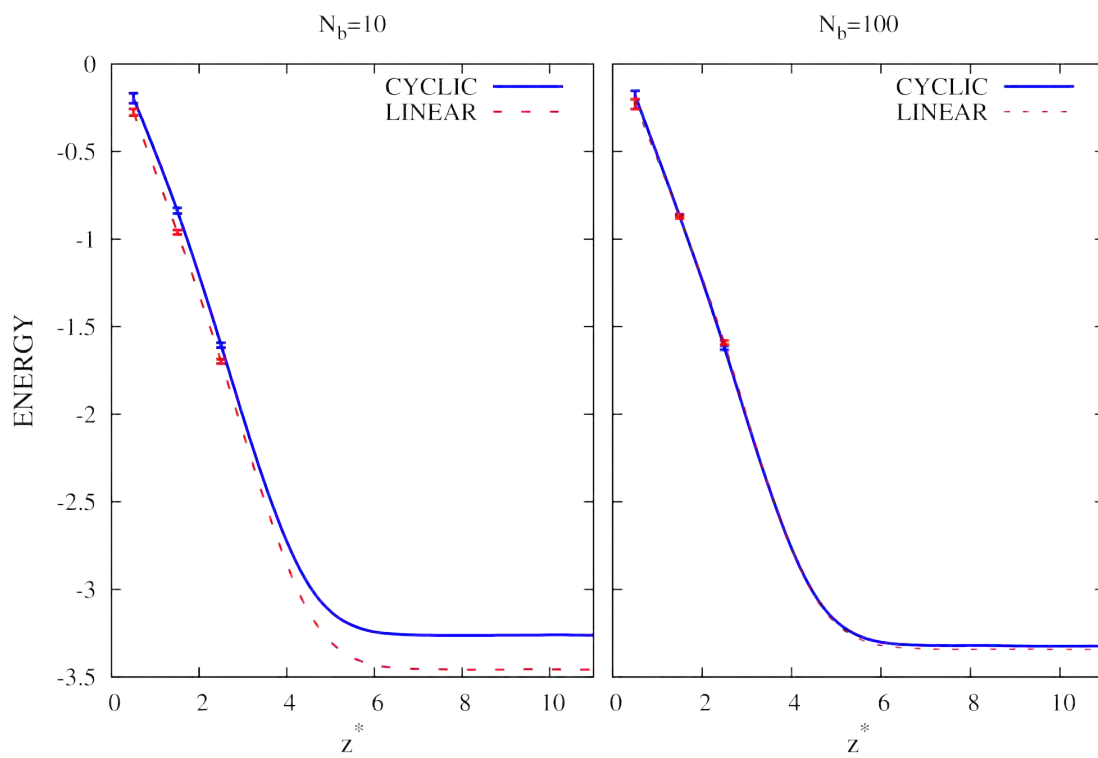


Figure 4.26: Energy per bead as a function of the distance from the interface.

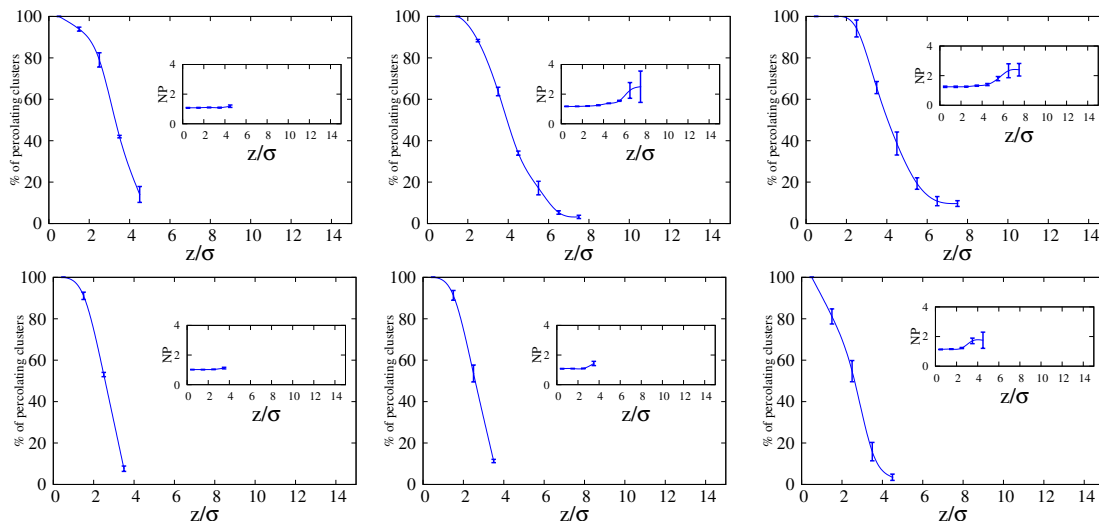


Figure 4.27: Percentage of percolating clusters starting from the interface as a function of the distance from it for polymer species made of 7-mers (leftmost panels), 10-mers (middle panels), and 20-mers (rightmost panels) chains at low cyclic composition:  $c^0 = 0.7$ . Upper panels are the results for linear chains. Bottom panels for cyclic chains. Insets report the average number of polymers per cluster as a function of the distance from the interface.

ones consisting on the average of not more than two polymers.

In Figure 4.28 we report the percentage of percolating clusters for the intermediate-long chains. For  $N_b = 30$  and for linear chains, we see that the percolation length increases up to around  $9\sigma$  with at least nearly 5% of clusters still percolating and an average number of polymers up to 3 – 5 polymers per cluster. For cyclic polymers the percolation distance and the number of clusters per polymer do not substantially increase in comparison to  $N_b = 20$  (see Figure 4.27), however the percentage of percolating clusters does increase to become nearly 5%. For  $N_b = 50$ , we observe a further increase of the percolating distance for linear polymers up to nearly  $11\sigma$ , with a percentage of percolating clusters still of the order of 5% at that distance and a number of average polymers per cluster going down to nearly two again. In the case of cyclic chains the percolation distance slightly increases to nearly  $6\sigma$ , still with an average number of polymers per cluster equal to two. The most striking effect is noted when the degree of polymerization becomes  $N_b = 100$  for linear polymers: while the percolation distance continues to grow up to nearly  $14\sigma$  and nearly 5% of the clusters end up possessing an average number of polymers per cluster of the order of 200. In this case, there are most likely a few clusters only containing most of the polymers. In the case of cyclic polymers, we still observe a monotonic increase of the percolating distance up to  $10\sigma$  and an average number of polymers per cluster equal to 3.

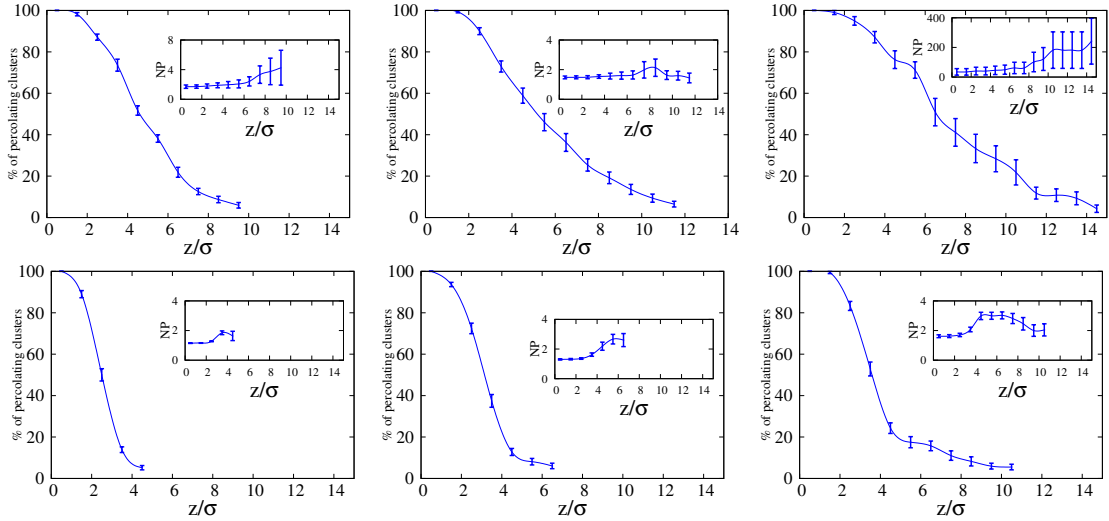


Figure 4.28: Percentage of percolating clusters starting from the interface as a function of the distance from it for polymer species made of 30-mers (leftmost panels), 50-mers (middle panels), and 100-mers (rightmost panels) chains at low cyclic composition:  $c^0 = 0.7$ . Upper panels are the results for linear chains. Bottom panels for cyclic chains. Insets report the average number of polymers per cluster as a function of the distance from the interface.

## 4.4 The equimolar regime

In this subsection, we provide a separate discussion of the results we obtained for the equimolar case, i.e.  $c^0 = 0.5$ . This case is particularly interesting because of the nature of our model system. The two polymer species have similar LJ interactions with both polymers belonging to the same and to different species. Then, any effect observed for this symmetrical composition shall be driven by the different topology of the two chains, and we can also exclude any effect due to the packing opportunities provided by the specific composition we are targeting. It is useful to recall that the composition regime we were interested in is the one where cyclic chains are less concentrated than linear chains, because that is the regime where experiments reveal a discrepancy with the predictions of the GFT, and that is also the regime where the approximations adopted within the GFT are valid.

### 4.4.1 Density and Local Composition Profiles

The density profiles as a function of the distance from the interface have been reported in Figure 4.29 for the chain lengths we considered in this research work, and the associated composition profiles in Figure 4.30. The behaviour very close to the interface is not a monotonous one, at difference than the one we observed for the lower cyclic compositions. In general the density profiles seem to indicate an amassing of cyclic chains which becomes larger as the degree of polymerization is increased from  $N_b = 30$  to 100, i.e. for the longer chains (see bottom panels of Figure 4.29. How-

ever, this amassing is evident in the density profiles over a range of distances from the interface between  $z^* \approx 2$  to  $6 - 8$ , with a clear tendency to become more extended far from the interface as the chain length increases. However, the behaviour very close to the interface is not clear-cut, especially if we look at the local composition profiles carefully (see Figure 4.30). In fact, while the increased density of cyclic chains in the aforementioned range for longer chains is clearly mapped onto the local composition profiles (see bottom panels of Figure 4.30), the observed enhancement of the local composition very close to the interface is not revealing us any trend when the degree of polymerization is increased from low to high values. We will understand this issue better later on, when we shall be considering the results for surface adsorption by the perspective of calculations based on the instantaneous interface.

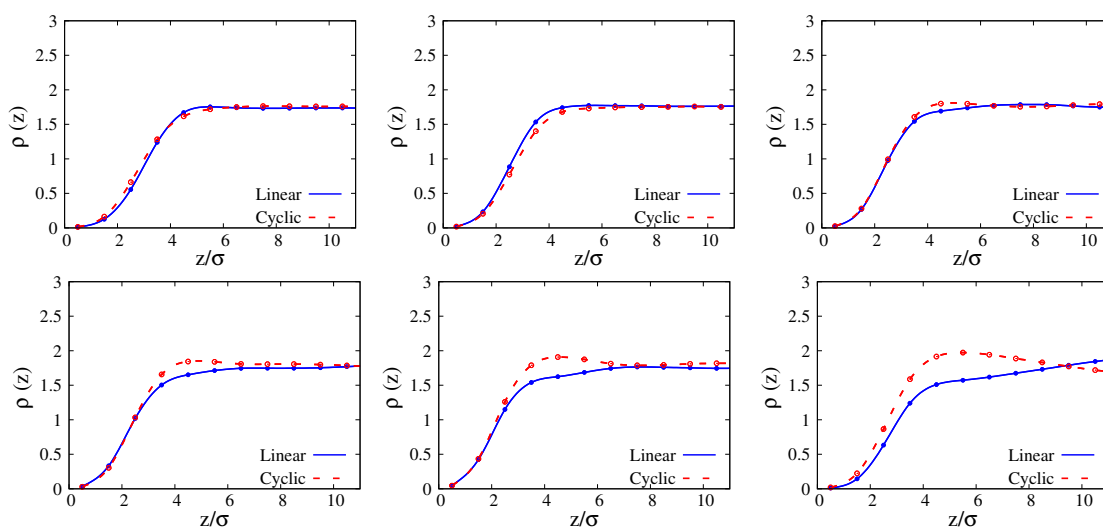


Figure 4.29: Local density profiles of free-standing films made of 7-mers, 10-mers, 20-mers (top panel: from left to right), 30-mers, 50-mers, and 100-mers (bottom panel: from left to right) at equimolar composition.

#### 4.4.2 Radius of Gyration

In this sub-section, we monitored again the radius of gyration  $R_g$  (we remind that this quantity is linked to polymer flexibility and conformational entropy), as a function of the distance from the interface. In the subsequent discussion, even if we refer to the average square of the radius of gyration what we report in the figures is the value of the two components  $\overline{R_{g\perp}^2}$  and  $\overline{R_{g\parallel}^2}$  of the radius of gyration as scaled by their respective *bulk* (far from the interface) values.

Looking at the transverse component of  $\overline{R_g^2}$  as a function of the distance from the interface, as reported in Figure 4.31 we retrieve the general trend observed for lower cyclic compositions, i.e. both polymer species fold more and more in the direction perpendicular to the interface when approaching it. However, as we increase the chain length we easily recognize that the transverse dimension of linear polymers gets more folded as compared to cyclic chains when we approach the

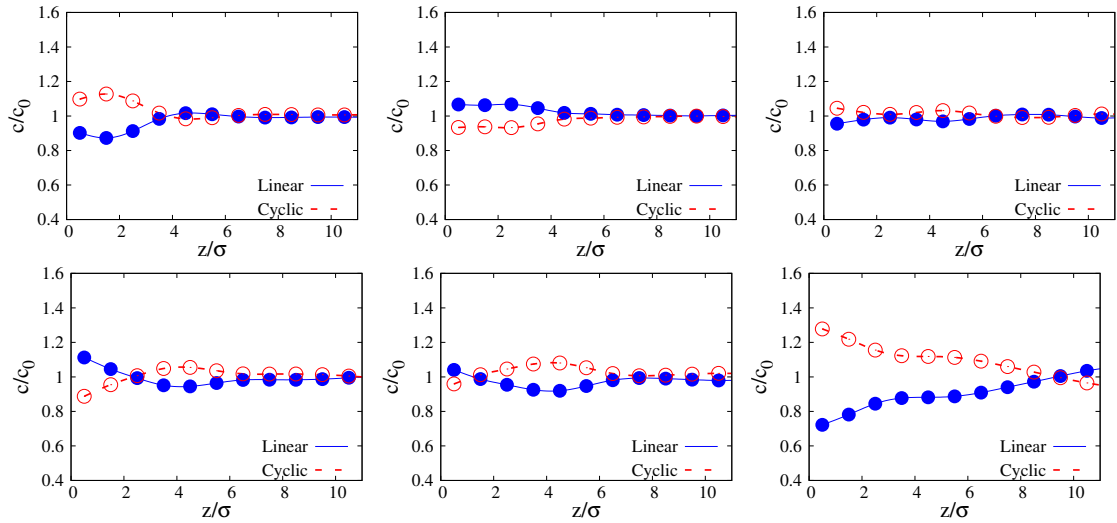


Figure 4.30: Local Composition profile of free-standing films made of 7-mers, 10-mers, 20-mers (top panel: from left to right), 30-mers, 50-mers, and 100-mers (bottom panel: from left to right) at equimolar composition.

interface. By decreasing the linear composition from  $c^0 = 0.8$  to 0.5, we observe by comparison of Figures 4.7, 4.8 and 4.31 that for longer chains the separation between the transverse components of the radius of gyration  $\overline{R}_{g\perp}^2$  of linear and cyclic polymers very close to the interface becomes in general more marked, even though the amount of folding of linear polymers with respect to the *bulk* value keeps almost unchanged. This feature is particularly evident for the longest chain length considered, i.e.  $N_b = 100$ . For the longer chains (see bottom panels of Figure 4.31 we observe again that in intermediate range of distances from the interface  $\overline{R}_{g\perp}^2$  becomes smaller for linear chains when we increase the chain length, similarly as for the higher linear compositions discussed before.

The results for the parallel component of  $\overline{R}_g^2$  are reported in Figure (4.32). Similarly as it was shown for the higher linear compositions in Figures 4.10 - 4.11, we clearly see the presence of a maximum in  $\overline{R}_{g\parallel}^2$  at intermediate distances or not far from the interface, which is generally more pronounced for longer chains. Once again, we note that linear polymers get more folded along the directions parallel to the interface as compared to cyclic polymers, and that the relative discrepancy between the  $\overline{R}_{g\parallel}^2$  of linear and cyclic polymers is more pronounced than the one between the transverse components  $\overline{R}_{g\perp}^2$ . The failure of cyclic polymers to fold significantly along the directions parallel to the interface as compared to linear polymers provide again evidence of a higher loss of conformational entropy of linear polymers at the interface for long chains. This effect should support cyclic chain enhancement at the interface for long chains, as we commented before (the higher loss of conformational entropy by linear chains makes them un-favoured at the interface), even if the results for the local composition as reported in the previous section were inconclusive. However, we shall see that when taking into account the roughness of the polymer-

vacuum interface in the next section we will come to a more reasonable picture for these results. The comments that we made before for the observed swelling of the shape of cyclic chains along the directions parallel to the interface still hold in the current case of equimolar composition, that is explained in terms of the topological repulsion of blobs in a ring, which does not allow other rings to be tangled [55]. Similarly it holds for the evidence of the existence of such repulsion between cyclic chains at the interface when we look at the average cyclic-cyclic energy per bead, that is positive (see the sub-section with energy calculations for the equimolar composition as reported subsequently). This energetic repulsion diminishes for longer chains because the more open shape of cyclic chains along the interface favours self interactions among cyclic polymers. Then, we would not be surprised if we could verify by other means that for longer chains, the composition of cyclic polymers is enhanced nearby the interface again.

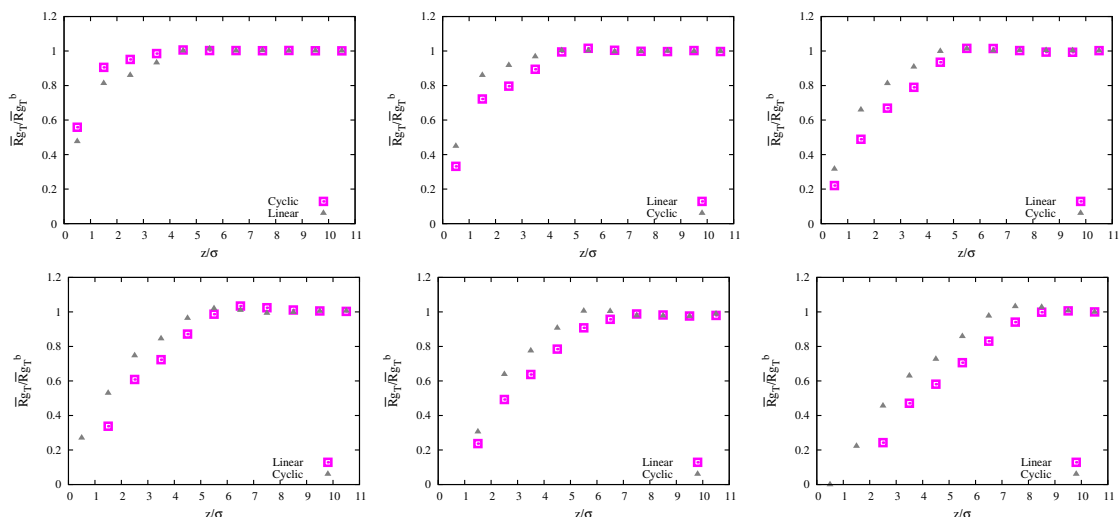


Figure 4.31: Average perpendicular component radius of gyration of 7-mers, 10-mers, 20-mers (top panel: from left to right), 30-mers, 50-mers, and 100-mers (bottom panel: from left to right) at equimolar composition.

#### 4.4.3 Instantaneous Interface

Now we eliminate the bias of not having a clear-cut planar interface between the empty space and the polymer blend also for the equimolar case. Given the poor evidence of any trend in the enhancement of one of the two polymer species at the surface, as it emerged in the previous density/local composition profiles, the next calculations are especially useful to highlight any preferential adsorption. The percentage of linear and cyclic chains in each bin starting from the instantaneous interface is reported in Figure 4.33. The evidence reported in this Figure is a clear one and confirms what the previous calculations on the radius of gyration seemed to suggest to us: by increasing the chain length (top panels from left to right and bottom panels again from left to right) we move smoothly from a situation where linear chains are more adsorbed than cyclic

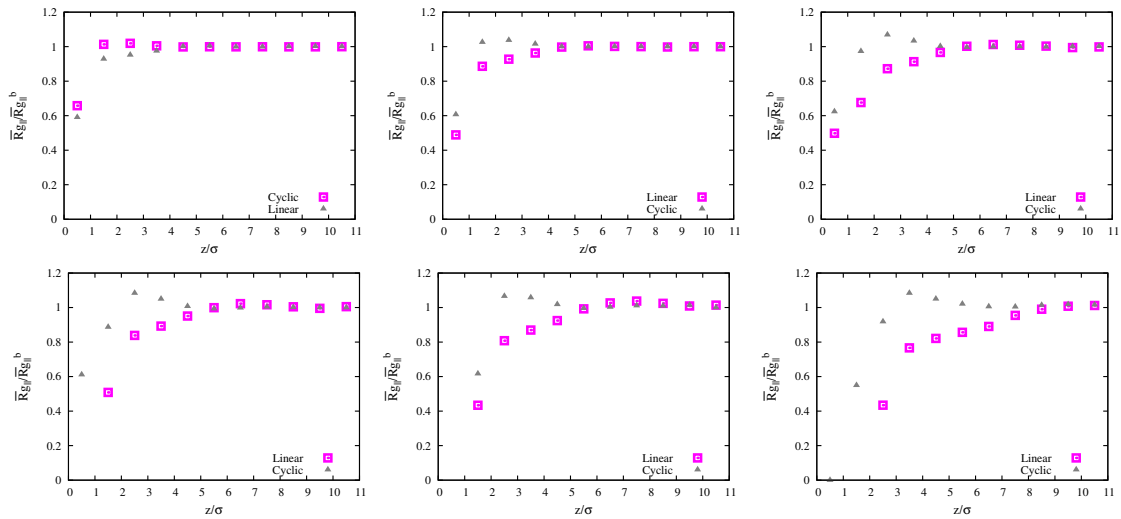


Figure 4.32: Average parallel component of the radius of gyration of free-standing films of 7-mers, 10-mers, 20-mers (top panel: from left to right), 30-mers, 50-mers, and 100-mers (bottom panel: from left to right) at equimolar composition.

chains (short-chain lengths), to a situation at intermediate chain lengths where the two species are competing for getting to the surface, until eventually cyclic chains are more enhanced than linear ones at the interface (long-chain lengths). In all the cases, the two polymer species are enhanced at the interface with respect to their *bulk* values: it is their relative enhancement that is different at the interface and it is suggesting us that we have enhancement of the composition of linear polymers in the short chain case, and depletion in the long chain case. The threshold for passing from linear enhancement to cyclic one is observed between  $N_b = 20 - 30$  beads per polymer for the equimolar composition, while it was detected at higher degrees of polymerization for the higher linear compositions (see Figure 4.14). We also note that in this case it is not the concentration of cyclic polymers only that is subject to higher fluctuations as we move far away from the interface for the long-chain lengths, but the same holds also for the linear concentration (compare Figures 4.14 and 4.33).

When we look at the percentage of chain-ends and middle-beads of linear polymers as a function of the distance from the interface, as reported in Figure 4.34, we find once again that chain-ends are always preferred at the interface. However, for the equimolar case we were also able to find an interesting trend when comparing the enhancement of chain-ends and the one of middle beads at the interface: while both the two quantities are enhanced, we note that chain-ends are always more enhanced, which suggests once again the geometry sketched in Figure 4.16; (a) for the linear polymers adsorbed at the interface; aside that, the relative difference between the chain-ends and the middle beads enhancement tend to become larger as the chain length is increased from  $N_b = 7$  to 100, which suggests that the geometry of the linear polymer of Figure 4.16; (a) standing flat at the interface is particularly expected for short-chain lengths.

The conclusions as related to these results are then similar to the ones we drew in the higher linear chain composition regime. In the short chain case we can explain the observed and expected enhancement of the composition of linear polymers in terms of the existence of an entropic mechanism due to the chain-ends getting preferentially adsorbed at the interface. In the equimolar case, the percentage of chain-ends reported in Figure 4.15 is found not that larger for the long chain case in comparison to the short chain case, which suggests the entropic contribution originating from their presence is even less likely to have a sufficient magnitude to overcome the loss of conformational entropy of linear polymers. In fact, now we can interpret the results reported in Figure 4.32, showing that linear polymers get better folded at the interface in the long-chain case, in terms of a much greater loss of conformational entropy of linear polymers as compared to cyclic chains. In summary, in the long chain case, the competition of the entropy due to chain-ends (increasing for linear chains) and the one due to polymer conformation (decreasing for linear chains) favours cyclic polymers enrichment at the interface. For the short chain case, linear chains are expected to preferentially enrich the surface because of the gain in entropy due to chain-ends, while the conformational entropy is not playing a significant role due to the shortness of the polymer chains. In this case, we will see once again that when considering also the enthalpic contribution to the free energy of the system (see section reporting the energy calculations), that contribution will provide us with an additional reason to expect linear polymer enhancement at the interface for short chains.

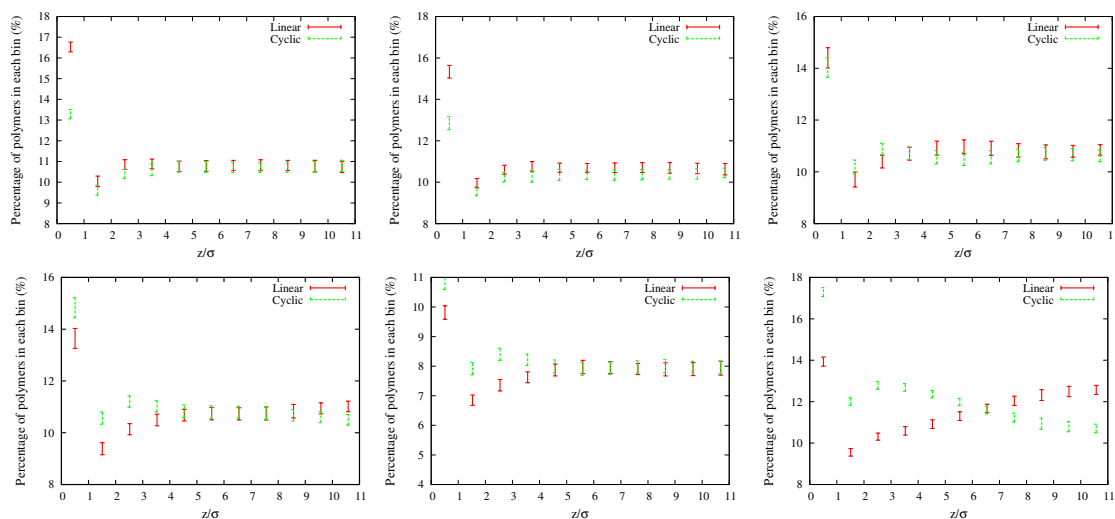


Figure 4.33: Average percentage number of polymer species made of 7-mers, 10-mers, 20-mers (top panel: from left to right), 30-mers, 50-mers, and 100-mers (bottom panel: from left to right) at equimolar composition.

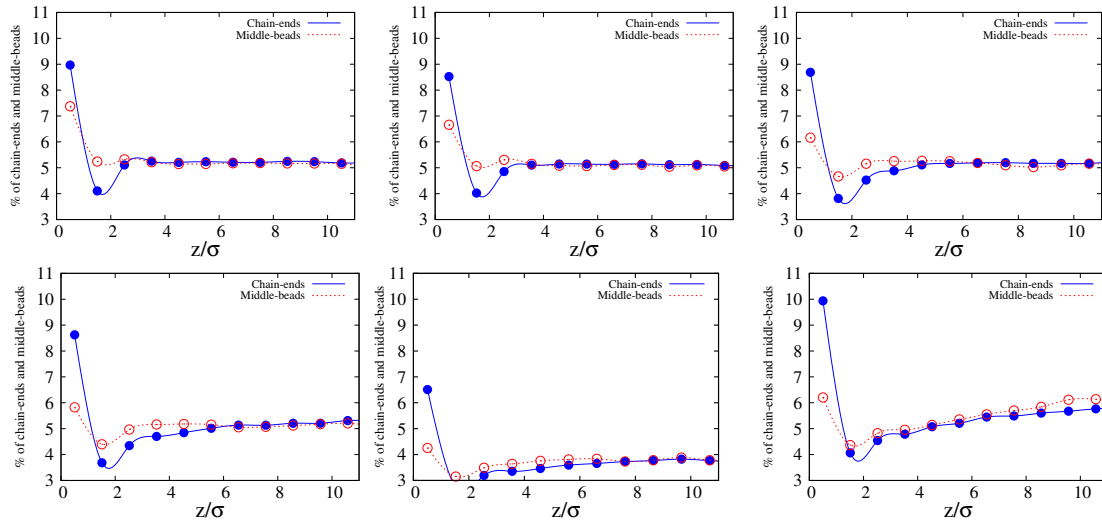


Figure 4.34: Average percentage number of chain-ends and middle points of linear polymers made of 7-mers, 10-mers, 20-mers (top panel: from left to right), 30-mers, 50-mers, and 100-mers (bottom panel: from left to right) at equimolar composition.

#### 4.4.4 Diffusion coefficients

The parallel and transverse components of the diffusion coefficient as a function of the distance from the interface are reported in Figures 4.35 and 4.36, respectively. The diffusion coefficients are scaled by their *bulk* counterparts, similarly as it was done in the previous section dealing with the low cyclic compositions. The tendency of the diffusion coefficient of the two polymer species to increase as they get closer to the interface from the *bulk* is still present in the equimolar case. The main difference between the behaviour of the parallel and transverse components is that the parallel diffusion coefficient of linear polymers tends to achieve higher maximum values in the intermediate range of distances from the interface in comparison to cyclic chains. On the contrary, the transverse component of the two polymer species is very similar and tends to exhibit the same local minimum at values slightly below the respective *bulk* ones in the range of distances between  $4 - 6\sigma$ .

#### 4.4.5 Interaction Energies of polymer species

In this section we focus on the interaction energy among polymer beads for the equimolar case. The remarks we have done before still hold and we expect that since the energy parameters we selected for the study of this section are the same for both linear and cyclic chains, there won't be any preferential enthalpic contribution favouring self-interactions between polymer beads belonging to the same species, or crossed interactions between polymer beads belonging to different species. Besides that, the fact we are considering a 50%-50% case should make the energies of the two polymer species equal to each other, unless the different topologies of the two species make them

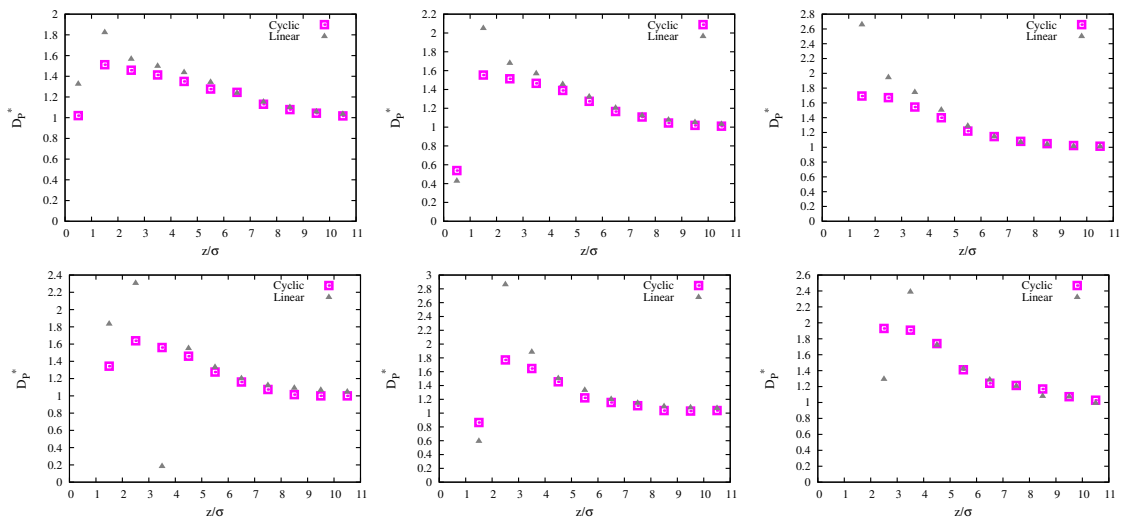


Figure 4.35: Parallel component of the diffusion coefficient as a function of distance from the surface for polymer species made of 7-mers, 10-mers, 20-mers (top panel: from left to right), 30-mers, 50-mers, and 100-mers (bottom panel: from left to right) at equimolar composition.

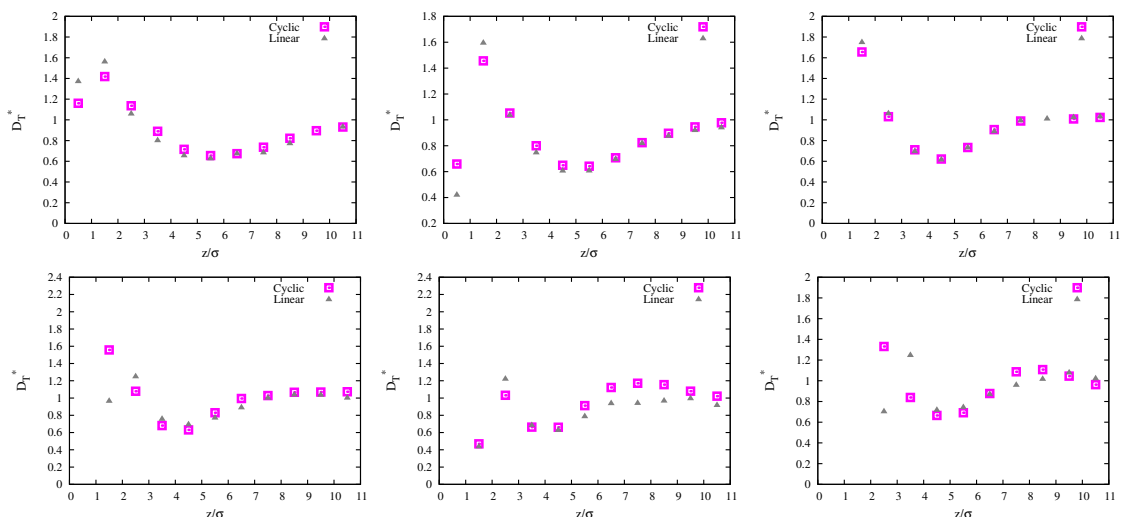


Figure 4.36: Transverse component of the diffusion coefficient as a function of distance from the surface for polymer species made of 7-mers, 10-mers, 20-mers (top panel: from left to right), 30-mers, 50-mers, and 100-mers (bottom panel: from left to right) at equimolar composition.

different.

We keep the same notations adopted in the higher linear chain composition case, and we report the total and self- energies per bead for the two polymer species in Figure (4.37) as a function of the distance from the interface. As expected both the two different types of energy are similar across the two polymer species. Strikingly enough, any difference in the near-interface values of the energy are detected in the small chain cases only. Then, we can confirm also in the equimolar case that this effect is driven by the loop topology of cyclic chains, which generates a geometrical

constraint on cyclic molecules preventing them from packing against each other effectively as linear chains. The fact that self-energies among linear polymers are smaller than cyclic ones, and that the difference between the self-energies and the total energies as reported in Figure (4.37) are of the same magnitude, strongly supports again that the better ability of linear chains to pack onto chains of the same species so to minimize their self-energy is an especially important factor when we consider short-chain lengths. What is most important to us is that this combined effect of energy gain of linear polymers and energy depletion of cyclic polymers at low degrees of polymerization is a genuine enthalpic effect, and it is also one of the factors which determine cyclic chain depletion at the interface (i.e. linear chain enhancement) for systems with small polymer mass, as we anticipated in the calculations based on the instantaneous interface. In other words, since cyclic polymers are less flexible than linear polymers at small degrees of polymerization, they achieve a less than optimal number of pair interactions among their beads with beads belonging to the same species. Once again, the lack of flexibility of cyclic polymers as determined by the loop topology when their chain length is small emerges as a tight constraint affecting their tendency to move towards the surface. The better minimization of their surface energy, allows linear polymers to achieve a lower interfacial free energy than cyclic polymers, by also being assisted by the maximization of their entropy thanks to the mechanism offered by their chain-ends.

In the long chain case, the energies per bead tend to become very similar both nearby the interface and far away from it, as shown in Figure 4.37. The conclusion is again that when the chain lengths is long enough, the loop constraint becomes less important in undermining the flexibility of polymer chains. Cyclic polymers will achieve a lower interfacial free energy than linear polymers because they possess an higher conformational entropy, as it was demonstrated in Figure 4.32.

#### 4.4.6 Percolation

When looking at the percolation of the two polymer species starting from the interface, we calculated again the percentage of clusters starting from the interface and their percolation size into the *bulk* of the blend, as well as the average number of polymers these clusters were formed of. The procedure to detect a cluster percolating from the interface has already been explained in the previous section considering the case of low cyclic compositions. The relevant percolation properties of linear and cyclic polymers are reported for  $N_b = 10, 30, 50$  beads per polymer in Figure 4.38. This Figure shows clearly that the longer percolation distances from the interface reached by linear polymers (top panel) are not trivially due to the fact that before we were considering systems where cyclic polymers were less concentrated than linear polymers. In fact, the percolation lengths always extend deeper into the blend for clusters of linear polymers also in the equimolar case. This evidence supports the idea of better self-packing properties achieved by linear chains in comparison to cyclic ones, even in the case of small chain lengths.

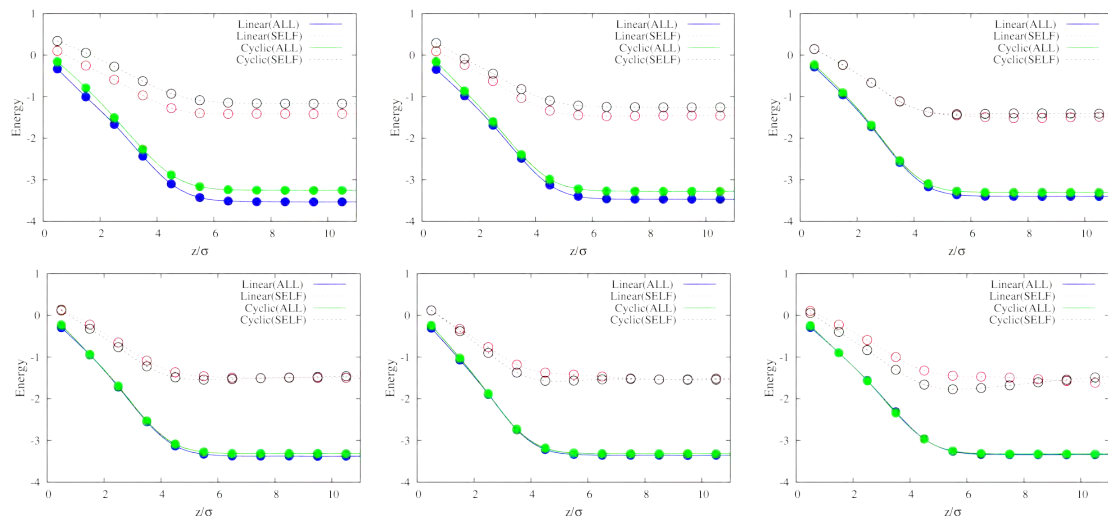


Figure 4.37: Energy per bead of different polymer species as a function of distance from the surface for polymer species made of 7-mers, 10-mers, 20-mers (top panel: from left to right), 30-mers, 50-mers, and 100-mers (bottom panel: from left to right) at equimolar composition. ALL refers to the energy per bead as calculated regardless of the nature of the bead. SELF refers to the energy per bead as calculated by considering beads belonging to the same polymer species only.

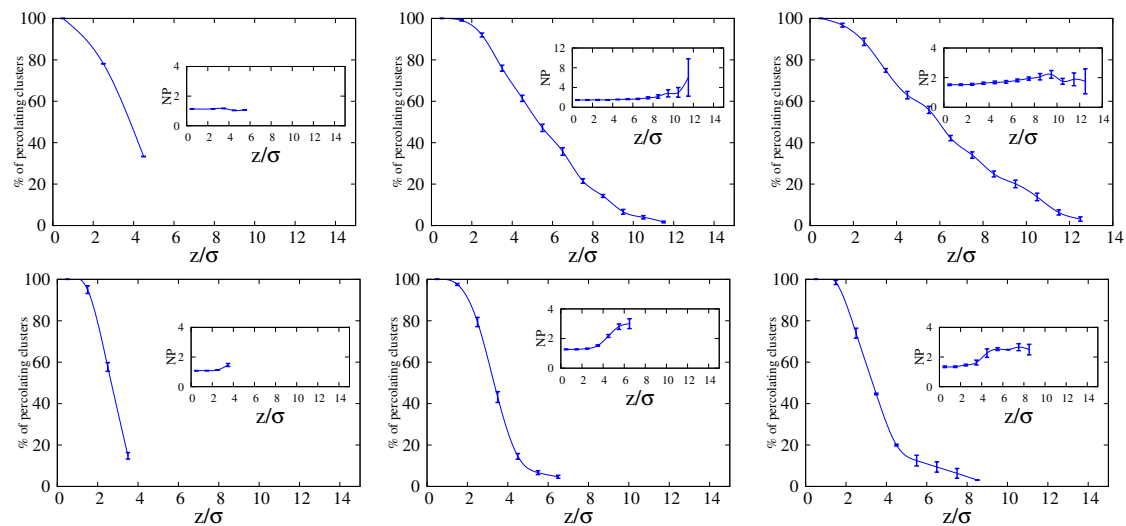


Figure 4.38: Percentage of percolating clusters starting from the interface as a function of the distance from it for polymer species made of 10-mers (leftmost panels), 30-mers (middle panels), and 50-mers (rightmost panels) at equimolar composition. Upper panels are the results for linear chains. Bottom panels for cyclic chains. Insets report the average number of polymers per cluster as a function of the distance from the interface.

## Chapter 5

# Experimental study of polymer blends

### 5.1 Introduction

Organic thin film solar cells has evolved into a promising technology for renewable energy sources in recent years, as a result of a steady improvement in power conversion efficiency (PCE) since the first report of planar donor-acceptor heterojunction [88]. Notable improvement in PCE of organic photovoltaic cell was observed after the introduction of bulk heterojunctions (BHJ) device structure employing blends of donor and acceptor materials. The phase separation between donors and acceptors in the photoactive medium into nanoscale interpenetrating networks dramatically increases the donor-acceptor interfaces per unit volume [60]. The most efficient BHJ-OTFSC devices to date is fabricated based on conjugated polymers, poly(3-hexylthiophene) (P3HT), blended with soluble fullerene derivatives such as, [6,6]-phenyl C<sub>61</sub> butyric acid methyl ester (PCBM). In fact, the best blend of P3HT:PCBM in solar cells deliver power conversion efficiencies of (5-9)% [89, 90]. The chemical synthesis of various conjugated polymer molecules depicted in Figure 1.1 have also brought light to the realization of OTFSC. Moreover, a number of investigations employing suitable buffer layers, mixed solvents and thermal annealing have been performed to optimize the phase separation between P3HT and PCBM and induce crystallization into P3HT domain with the objective of improving device performance. In addition, it has been reported that morphology of the BHJ active layer in Polymer Solar Cells (PSCs) can be modified using mixed solvents and additives [91] with different boiling points [92, 93] to induce more preferential phase segregations in the blend. In experimental investigation Zhang *et al.*[92] recorded significant improvement in  $J_{sc}$  from 3.2 to 5.2 mA/cm<sup>2</sup> in APFO-3:PC<sub>61</sub>BM blend solar cell by adding a small amount of guest solvent chlorobenzene into a chloroform solution due to the formation of a more homogeneous nanomorphology. On the other hand, J. Peet *et al* [94] reported that the efficiency of the

PCPDTBT:PC<sub>71</sub>BM solar cell improved from 2.8% to 5.5% by using alkane dithiols as processing additive solvents. They reported that this was due to the more beneficial active layer morphology and since then, processing solvent additives have been widely used in the nanoscale morphological modification [95, 96, 97]. Lee *et al*[91], proposed two criteria for choosing the processing solvent additive in optimizing the nanomorphology of the BHJ active layer: one is that the polymer and the fullerene derivative should show selective solubility in the solvent additive; the other is the boiling point of the solvent additive, which should be higher than that of the host solvent. On an investigation using regioregular poly(3-hexylthiophene) (P3HT) [98, 99, 100] showed that the deposition conditions had a strong impact on the ordering of the polymer. For instance, in P3HT:PCBM blend active layer the crystallization of the P3HT phase can be inhibited by the clustering of fullerene in the blend annealing. This effect could be avoided by using a high boiling point solvent additive with selective solubility for fullerene, thereby allowing increased crystallinity of the P3HT without disruption by fullerene during thermal treatment[98, 101]. Looking at the active layer based on P3HT:PC<sub>61</sub>BM, it was observed that the processing solvent additive 1,8-diiodooctane, delayed the duration of drying process of the film which gave P3HT more time to crystallize. Likewise, the processing solvent additive was found to improve the morphology of the active layer based on PCPDTBT:PC<sub>71</sub>BM via improving the aggregation of the polymer[102].

Polymer-fullerene bulk heterojunction solar cells which contain blends of poly(3-hexylthiophene-2,5-diyl) and [6,6]-phenyl-C<sub>61</sub>-butyric acid methyl ester have been widely studied. Various studies have shown high power conversion efficiencies and well-defined nano-morphology [103, 104]. Clearly, the performance of these devices is critically dependent on the morphology of the donor and acceptor blend active layer. In our study, we created different types of morphologies in the P3HT:PCBM active layer by exploiting three different processing solvent additives with different boiling points. The reference blend was P3HT and PCBM which was dissolved in chloroform (CF) host solvent. Solvent additives such as 1,8-diiodooctane (DIO), 1-chloronaphthalene (CN), and dimethyl sulfoxide (DMSO) were used separately for different device preparations. The boiling points of the additives are 168°C(DIO), 250°C (CN) and 189°C (DMSO), respectively. These boiling points are higher than the host solvent CF (61.2°C) which ensures that there will be increase in nanoscale phase separation. However, the mechanism of interactions of the host solvent with DIO, CN and DMSO in the photoactive medium and its effectiveness on device stability remained unclear. An investigation of the relation between device performances and different morphologies as well as the charge transport properties of the device and the influence of additives are presented in the section below.

## 5.2 Material and Methods

The materials used in the preparation of bulk heterojunction devices were obtained from various chemical suppliers. Poly(3,4-ethylenedioxythiophene): poly(styrenesulfonate) (PEDOT:PSS),

poly(3-hexylthiophene-2,5-diyl), [6,6]-phenyl C61-butyric acid methyl ester and ITO coated glass substrate were purchased from Oscilla Ltd and used without further purification. Isopropanol, acetone, chloroform (CF), 1,8-diiodooctane, 1-chloronaphthalene and dimethyl sulfoxide were purchased from Sigma Aldrich and used as received. The solution of the photoactive layer composed of P3HT and PCBM blend at 1:1 ratio by weight was prepared in chloroform solvent at the concentration of 20 mg/ml. Four types of solutions were prepared; one without additive and three others with additives such as DIO, CN and DMSO, respectively. The DIO and CN were used 3% by volume with CF host solvent, however, we used 1% and 10% DMSO with respect CF.

The organic solar cell were fabricated using ITO coated glass substrate (30 cm × 30 cm) which were partially etched using acid solution containing HCl:H<sub>2</sub>O:NH<sub>3</sub>O<sub>3</sub>. The substrates were then cleaned by ultrasonic bath using deionized water, acetone and isopropanol sequentially for 10 minutes. The substrates were then dried in an open oven at 120°C for 10 minutes holding time. The hole transport layer PEDOT:PSS were spin coated on each substrate at 3500rpm and followed by annealing in Nitrogen (N<sub>2</sub>) atmosphere at 120°C for 10 minutes. This buffer layer assures better hole mobility from the polymer to the ITO electrode. PEDOT:PSS also prevents any possible short circuiting due to the ITO spikes and pin holes. The photoactive layers were spin coated from the solution at 1200rpm on top of the PEDOT:PSS layer. After holding the samples for nearly 5 minutes at 70°C in the furnace, they were immediately transferred into a vacuum deposition chamber for the counter electrode deposition. Once the vacuum pressure reached the lowest possible value ( $\approx 2 \times 10^{-6}$ mbar) then lithium ferrite (LiF) and aluminium (Al) electrodes were deposited sequentially at 0.4nm and 50nm thickness, respectively. The active region of the diodes formed by the deposition mask ranged between 0.03 cm<sup>2</sup> and 0.05cm<sup>2</sup>. Optical absorption of the films were measured using double beam UV/VIS spectrophotometer (Model: UV-1601). The electrical properties of the devices were taken using computer interfaced Keithley HP2400 source-meter both under illumination and dark condition. The solar simulator (model SS50AAA) and AM1.5 was used operating at an integrated power intensity of 100mW/cm<sup>2</sup>. To investigate the variation of in-plane morphology induced by solvent mixing the scanning electron microscope (SEM) (Zeiss crossbeam series with Gemini FESEM) was used.

### 5.3 Solar cell parameters

The behavior of a solar cell resembles very much like a simple diode whose current can be described by a simple diode equations. The properties of a solar cell can be modeled in terms of an equivalent circuit containing a rectifying diode as depicted in Fig 5.1. The most common equivalent electrical circuits used to model OTFSCs are the one-diode model (ODM) or two-diode model (TDM) [66, 67, 68, 69]. These models have been used to describe most inorganic p-n junction solar cells which can equally be applied to the organic counter part [70]. The current output from a solar cell can be derived from the diode equations which takes the following form when the diode is under

illumination;

$$J = J_s \left[ \exp\left(\frac{qV}{k_B T}\right) - 1 \right] - J_{ph}, \quad (5.1)$$

where  $J_s$  and  $J_{ph}$  are the reverse saturation current and the photo-generated current densities, respectively.  $q$  is the elementary charge,  $V$  is the applied voltage,  $k_B$  is the Boltzmann constant,  $T$  is the temperature. Under dark conditions, the cell can be thought of as a current source where  $J_{ph}$  is a reverse current and an output from the cell can be described as:

$$J = J_s \left[ \exp\left(\frac{qV}{k_B T}\right) - 1 \right]. \quad (5.2)$$

With this basic diode equation, the important parameters of the solar cell were evaluated. The

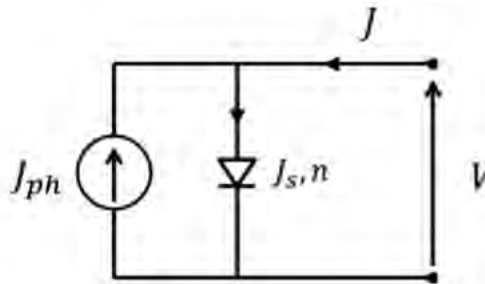


Figure 5.1: Equivalent circuit diagram of ideal solar cells [65].

power conversion efficiency (PCE) is defined as;

$$\eta = \frac{P_{out}}{P_{in}} = \frac{J_{max} V_{max}}{P_{in}} = \frac{J_{sc} V_{oc}}{P_{in}} FF \quad (5.3)$$

where  $P_{in}$  is the light power incident on the device generated when solar simulators are used,  $P_{out}$  is the maximum extractable power by the solar cell. The rest of the parameters, used in the determination of performance of organic solar cells (OSC), are known as fill factor (FF), given by the relation;

$$FF = \frac{J_{max} V_{max}}{J_{sc} V_{oc}}. \quad (5.4)$$

The short-circuit current density ( $J_{sc}$ ) and open-circuit voltage ( $V_{oc}$ ) can be measured directly from the J-V curve. A short-circuit current density is the current that flows through an illuminated solar cell when the voltage across the solar cell is zero, i.e. when the electrodes of the device are directly connected together. It is the largest current that the cell is able to produce. The open-circuit voltage is the largest possible voltage across the cell under sunlight when no current is flowing. In order to maximize the PCE of the cell, all the physical parameters mentioned above need to be maximized. This issue has been addressed by several publications which show that,  $J_{sc}$  can be affected by light absorption, charge recombination and charge collection by electrodes. Similarly, the value of  $V_{oc}$  can be determined by the energy levels mismatch of the materials, recombination and current leakage while the FF can be affected by internal resistance of the cell, electrodes charge collection, and recombination[68, 70].

### 5.3.1 Space Charge limited current

The space charge limited current provides information about field dependant charge transport properties in the medium in the absence of photon induced generation of charges. The measured dark current carries all the necessary information about the nature of the charge transport in the device. Figures. 5.2 shows typical characteristics of the dark currents taken from the diode of a sample in the logarithm scale with their respective regions. Region S1 is the ohmic regime at lower voltage where the current is proportional to the electric field ( $J \propto V$ ), while Region S2 is the nonohmic regime where the current is in the exponential form ( $J \propto \exp^{qV/kT}$ ). As the voltage increases, the charges tend to move towards the region (S3) between the electrodes and the electric field. This region S3 is named space charge limited current (SCLC) regime where the current is proportional to the square of the electric field ( $J \propto V^2$ ). The shape of the J–V characteristics

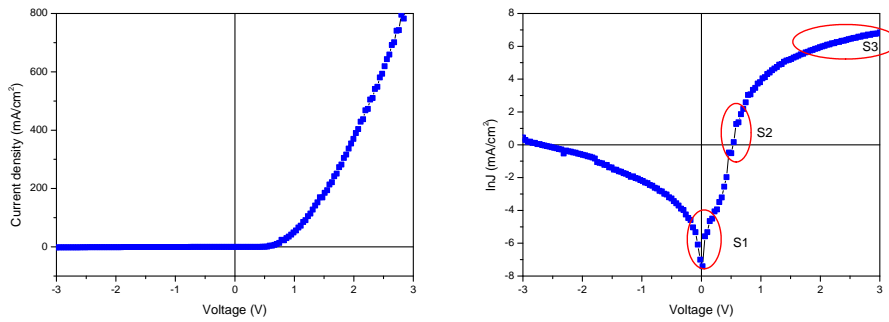


Figure 5.2: J vs V graph of organic thin film based solar cell under dark conditions.

is nonlinear curve which is based on the fact it clearly gives us the typical diode knees at various applied voltages and represent the different transport phenomena in any semiconductor device. However, it should be noted that in a semiconductor, there is a background concentration of charges  $N_0$  due to thermal excitation as well as impurities. As a result, when the injected carrier density  $N_i$  is much lower than  $N_0$  at very low voltages, then the current obeys Ohm's law where the current is directly proportional to the applied voltage:

$$J_{OHM} = eN_0\mu \frac{V}{L} \quad (5.5)$$

where  $e$  is the electronic charge,  $\mu$  is the carrier mobility,  $V$  is the voltage drop across the sample and  $L$  is the active layer thickness. As the applied voltage increases more charges are injected from the the electrodes and the current in the device sharply increased. This current region is called injection limited current and the current grew exponentially with applied voltage. Finally, at high applied voltage the current in the device slowly reaches maximum at slower rate. This region is called space charge limited current (SCLC) which is limited by the maximum amount of charge available in the medium. Therefore, the maximum current that can flow through a trap-free semiconductor can be described by Mott-Gurney law expressed by the following current density

equation[105, 106]

$$J_{SCL} = \frac{9}{8} \varepsilon \varepsilon_0 \mu \frac{V^2}{L^3} \quad (5.6)$$

where  $\varepsilon$  is the relative dielectric permittivity of the material,  $\varepsilon_0$  is the permittivity of free space. However, the relationship between charge mobility and electric field ( $E = V/L$ ) in highly field-dependent semiconductor is given by Poole-Frenkel equation described as;

$$\mu = \mu_0 \exp(\gamma \sqrt{E}) \quad (5.7)$$

where  $\mu_0$  is the low-field mobility and  $\gamma$  is an empirically determined field activation factor. Substituting Eq. (5.7) in Eq. (5.6) one obtain;

$$J_{SCL} = \frac{9}{8} \varepsilon \varepsilon_0 \mu_0 \exp(\gamma \sqrt{V/L}) \frac{V^2}{L^3}, \quad (5.8)$$

## 5.4 Results and Discussion

In this section, we discussed the results of the optical and electrical properties as well as the morphology of the fabricated P3HT:PCBM organic thin film solar cell. Bulk heterojunction organic thin film solar cell with the chemical solvent additives of DIO, CN and DMSO were fabricated under ambient laboratory conditions where the samples were prepared and tested in an open laboratory atmosphere. A sandwich type device structure consisting of a sequence of layers such as ITO/PEDOT:PSS/P3HT:PCBM/LiF/Al was employed. The samples were prepared under different conditions of P3HT:PCBM solution; namely with and without processing solvent additives.

### 5.4.1 Optical absorption properties of the devices

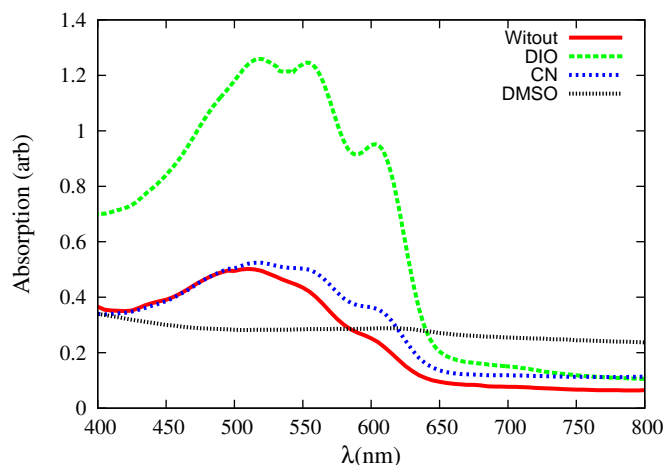


Figure 5.3: Optical absorption spectra of four different organic active layers of P3HT:PCBM blend fabricated with and without different solvent additive.

The optical absorption properties of P3HT:PCBM blend film with and without additives are studied and presented in this section. Figure. 5.3 shows the optical absorption spectra of the four

different P3HT:PCBM blend prepared without additive and with DIO, CN and DMSO processing solvent additives. The absorption spectra reflect the influence of processing solvent on the performance of the device and the morphology of the active layer with a significant changes being seen with the device prepared with DIO. From this spectra, it was noted that, the devices prepared without and with DIO and CN have the absorption bands extending over the range of 420-650 nm, while the one prepared with DMSO is completely flat over the same range. However, It can be seen that the device containing DIO exhibited the highest absorption coefficient whose peak absorbance is concentrated within 520-620 nm and the one with DMSO exhibited the lowest absorption coefficient, while the other two devices have apparently lower absorption coefficient but similar characteristics over the same range of wavelength. The stronger absorption observed in the device containing DIO solvent additive could be attributed to the more ordered structure of P3HT, which could contributed to the  $J_{sc}$  enhancement. Zero absorption observed in the device prepared with DMSO could be due to the fact that, DMSO processing solvent additive reduced the drying time of the wet film during spin coating which the polymer did not have enough time to crystallize. Clearly, this observation gives an idea on the best region of wavelength to compute the energy band gap of the device which is a very important factor in semiconductors.

#### 5.4.2 Electrical properties of the devices

This section discusses in detail the current-voltage characteristics of the OTFSC blend fabricated without additive and from DIO, CN and DMSO procesing solvent additives under illumination and dark conditions in an open atmosphere laboratory. It starts with the P3HT:PCBM blend spin coated from CF without additive and followed by the blend with different processing solvent additives.

##### P3HT:PCBM without additive solvent

Table 5.1: Photovoltaic parameters of best performed diodes of organic thin film solar cell devices based on the blend of P3HT:PCBM active layer prepared without additive.

Diodes	Voc (V)	Jsc (mA/cm <sup>2</sup> )	FF (%)	PCE (%)	Rs (ohms)
d1	0.578	7.830	40.08	1.813	601.96
d2	0.583	7.237	36.13	1.523	751.11
d3	0.572	7.613	43.27	1.884	442.87
d4	0.563	7.507	45.45	1.920	418.40
d5	0.562	7.656	43.84	1.887	630.04

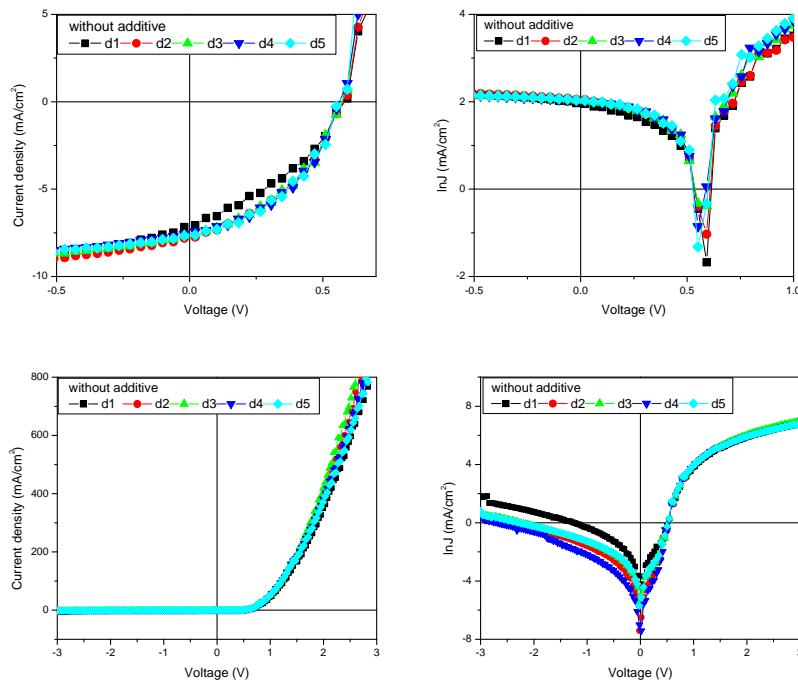


Figure 5.4: J-V characteristics of organic thin film solar cell devices based on the blend of P3HT:PCBM active layer prepared without additive under illumination and dark conditions.

The reference sample in this study was prepared from the solution containing P3HT:PCBM blend in host chloroform solvent without any processing additives. The solution was sonicated for 3 hours before use. The photoactive layer was then spin coated on top of PEDOT:PSS coated substrate at 1200rpm. The current-voltage characteristics given in Figure 1.1 clearly shows the nonlinear nature of the current output. The J-V curve taken under illumination shows the power output of the device as expressed by the large fill factor in the fourth quadrant. The measured parameters of the diodes are given in Table 5.1. The value of PCE is obviously lower than that found in literature though prepared in similar laboratory environment[107]. This low PCE results could be due to the poor miscibility of the blend within the active layer. Moreover, the measured fill factor is reasonably good under the preparation condition, however, the observed high series resistance of the devices seriously affect the shape of the J–V curves under illumination as reported in Figure 5.4. The open circuit voltage ( $V_{oc}$ ) and short circuit current ( $J_{sc}$ ) measured under illumination are comparable with the data reported in literatures. The space charge limiting current were found to be similar for all the diodes as reported in the bottom right hand panel of Figure 5.4. This suggest the good quality of the sample and an indication for good uniformity of active layer.

### P3HT:PCBM with 3% DIO

For performance improvement and optimization of the nanomorphology of the active layer purpose, 3% DIO by volume processing solvent additive was added into the reference blend solution based. The solution was then sonicated for three hours to allow homogeneity and inter-dispersion of the molecules. Afterwards, the same standard device preparation procedure described earlier was used in the device fabrication process. After sonication the photoactive layer was coated on PEDOT:PSS coated substrate at 1200rpm. As the result, the measured current-voltage characteristics of the devices indicated that the short circuit current ( $J_{sc}$ ) decreases significantly as we move from one diode to another as it can be seen from Table. 5.2. The decreasing tendency of the  $J_{sc}$  could be attributed to the light exposure time of the diodes, that is why we observed highest  $J_{sc}$  from diodes measured earlier than those measured latterly. Similarly, the open circuit voltage ( $V_{oc}$ ) as well as the power conversion efficiency (PCE) of the device exhibited an average value of 0.47 V and 2.77% respectively for all the diodes. However, this value of  $V_{oc}$  is a bit low compare to the value obtained in the device without additive (from 0.57 to 0.47). This situation was also noted in other studies, and it was attributed to the fact that polymer domains were more ordered in the active layers after the addition of DIO[94, 97]. In contrast, the performance of the device has improved by adding DIO into the blend based device, which result in to an increase in  $J_{sc}$ , in FF and in PCE. It was observed that, the enhancement in the FF positively affect the shape of the J–V curves showing in the top panel of Figure 5.5 under illumination conditions. The fill factor enhancement could be due to the more percolated networks for carrier transport in the active layer. The bottom panel of Figure 5.5 displays the dark currents of the devices.

Table 5.2: Photovoltaic parameters of best performed diodes of organic thin film solar cell devices based on the blend of P3HT:PCBM active layer prepared with DIO processing solvent additive.

Diodes	Voc (V)	Jsc (mA/cm <sup>2</sup> )	FF (%)	PCE (%)	Rs (ohms)
d1	0.469	11.359	50.624	2.699	104.670
d2	0.471	11.190	51.422	2.709	95.074
d3	0.469	10.410	56.117	2.741	207.363
d4	0.469	10.409	55.980	2.735	59.302
d5	0.469	9.909	59.650	2.773	175.977

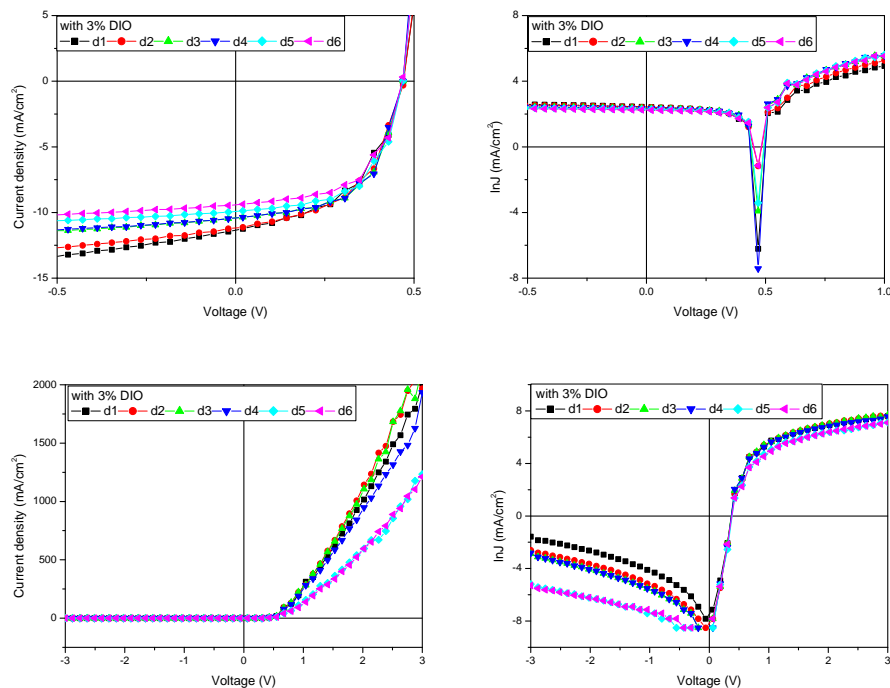


Figure 5.5: J-V characteristics of organic thin film solar cell devices based on the blend of P3HT:PCBM active layer prepared with DIO under illumination (top) and dark conditions (bottom).

Table 5.3: Photovoltaic parameters of best performed diodes of organic thin film solar cell devices based on the blend of P3HT:PCBM active layer prepared with CN processing solvent additive.

Diodes	Voc (V)	Jsc (mA/cm <sup>2</sup> )	FF (%)	PCE (%)	Rs (ohms)
d1	0.541	6.874	51.360	1.909	536
d2	0.549	10.701	48.586	2.859	671
d3	0.548	8.420	54.940	2.535	877
d4	0.537	8.540	44.667	2.046	699
d5	0.539	5.762	52.656	1.637	763

### P3HT:PCBM with 3% CN

The third set of samples was also prepared following the same procedure described in the reference sample, but this time, a 3% CN by volume of processing solvent was added in order to create another

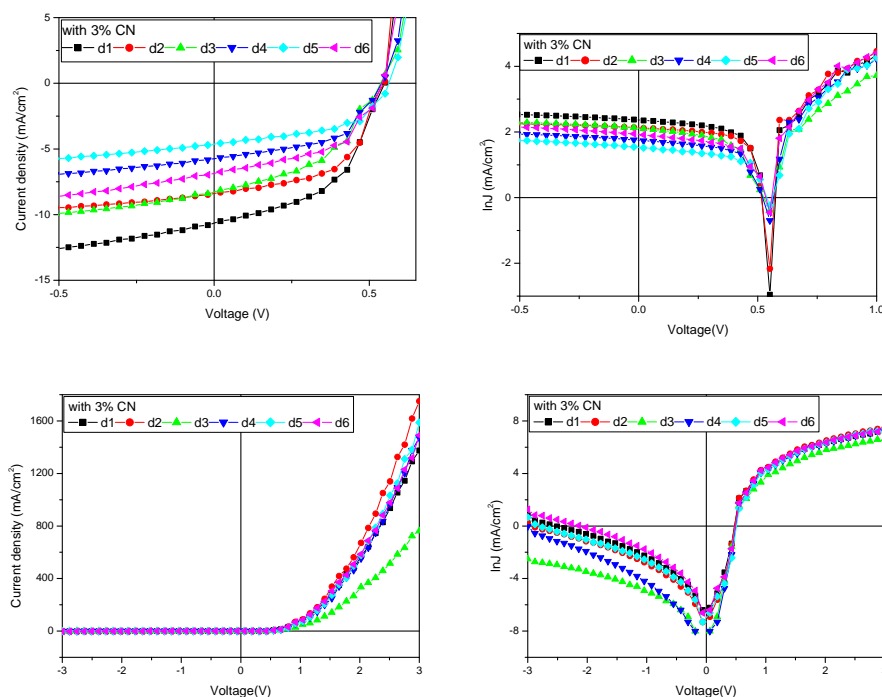


Figure 5.6: J-V characteristics of organic thin film solar cell devices based on the blend of P3HT:PCBM active layer prepared with CN under illumination and dark conditions.

type of morphology of the device and to be able to study the impact of this particular additive on the device. The J–V characteristics depicted in Figs. 5.6 were taken under illumination and dark conditions on the samples prepared from CN solvent. As a result, we found a significant drop on the short circuit current as compare to the device with DIO discussed above. The differences can clearly be seen in Table. 5.3. We also noted an average PCE value of 2.2% and a FF of 50.7% which are respectively lower than those reported in the device prepared with DIO. This could be attributed to the higher boiling point of CN (250°C) which results to moderate morphology formation of the polymers molecules.

### P3HT:PCBM with 1% DMSO

Figure. 5.7 shows the J–V characteristics of the OTFSC with blends prepared by diluting P3HT:PCBM solution with the host solvent CF and with 1v% DMSO under illumination and dark conditions. The devices performed poorly compare to all other devices discussed above. This result is surprising because DMSO has been used as processing additive moreover, it satisfies the requirements of processing additives: nonreacting materials with either the polymer and fullerene; selective solubility of one of the components and; higher boiling point than the host solvent. This appalling results could be attributed by the fact that, DMSO is the “secondary dopant” which is usually used as anodic buffer layers mainly to enhance conductivity of solar cells[108]. In our case, it was directly

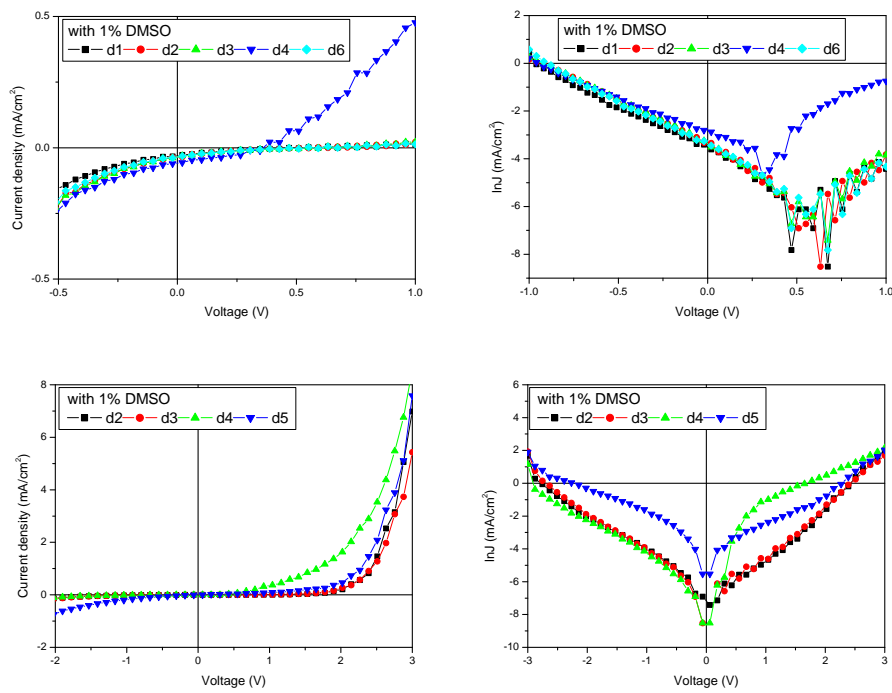


Figure 5.7: J-V characteristics of organic thin film solar cell devices based on the blend of P3HT:PCBM active layer prepared with DMSO under illumination and dark conditions.

Table 5.4: Photovoltaic parameters of best performed diodes of organic thin film solar cell devices based on the blend of P3HT:PCBM active layer prepared with DMSO processing solvent additive.

Diodes	Voc (V)	Jsc (mA/cm <sup>2</sup> )	FF (%)	PCE (%)	Rs (ohms)
d1	0.662	0.0350	13.752	0.0032	68981
d2	0.579	0.0302	16.389	0.0029	121271
d3	0.612	0.0356	15.019	0.0033	213740
d4	0.582	0.0345	15.282	0.0031	123135
d5	0.663	0.0388	14.244	0.0037	89168

added to the P3HT:PCBM active layer.

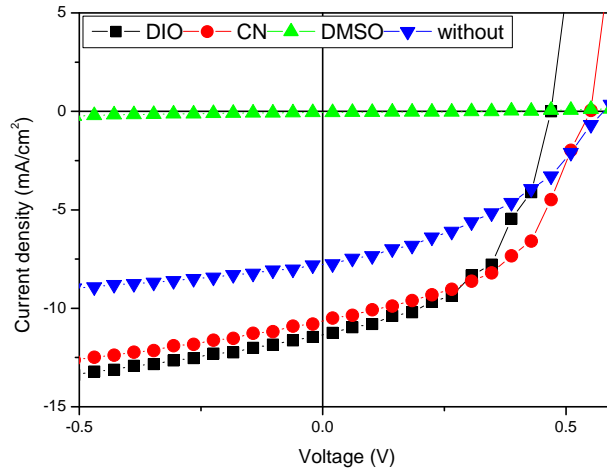


Figure 5.8: J-V characteristics of the four different organic thin film solar cell devices based on blended active layer of P3HT:PCBM prepared with different organic solvent mixture.

### 5.4.3 Comparison on the effect of various additives on performance of OTFSC

The J-V characteristics of four types of OTFSC based on blended active layer of P3HT:PCBM under illumination are shown in Fig 5.8. Likewise, the photovoltaic average performance parameters of the four different OTFSC devices are summarised in Table 5.5. From the summarised data, we noted that the OTFSC prepared without additive shows a PCE of 1.8%, while the one prepared with DIO and CN show respectively a PCE of 2.7% and 2.2%. These enhancements in PCE after adding DIO and CN were mostly contributed by the improved photocurrent and FF. Consequently, more advantageous nanomorphology of the device could be presumed in the SEM measurements. However, the device prepared using DMSO processing solvent additive exhibited poor  $J_{sc}$  and FF leading to a lowest PCE. These could be mainly due to the poor miscibility between P3HT and PCBM after adding DMSO, which resulted in a heterogeneous phase separation in the active layer. The open circuit voltages of the OTFSC are comparable. The DIO based cell exhibited the lowest  $V_{oc}=0.47V$  and the DMSO based cell the highest  $V_{oc}=0.62V$ . The device without additive and that with CN have their value in between; at  $V_{oc}=0.55V$  and  $V_{oc}=0.57V$  respectively. This observation could be related to the increased degree of orderliness of the molecules in polymer phase [109] or it could also be resulting from recombination of charge carriers. Finally, the best FF is observed in the device prepared with DIO (55.55%) whereas, the lowest is observed in the device prepared with DMSO (14.93%). The fill factor of the devices made with CN and without additive fall in between at (50.74%) and (41.75%). These differences in FF significantly impact the shapes of the J-V curves shows in Fig 5.8 with the best be the one prepared with DIO and the one prepared with DMSO has a dark current shape.

Table 5.5: Photovoltaic parameters of the four different organic thin film solar cell devices based on the blend of P3HT:PCBM active layer prepared with different organic solvent mixture.

P3HT:PCBM	Voc (V)	Jsc (mA/cm <sup>2</sup> )	FF (%)	PCE (%)	Rs (ohms)
CF with DIO (3v%)	0.468	10.655	54.758	2.729	128
CF with CN (3v%)	0.546	8.058	50.438	2.200	709
CF without additive	0.571	7.564	41.754	1.805	568
CF with DMSO (1v%)	0.619	0.0346	14.937	0.003	40792

#### 5.4.4 Charge transport properties on solvent mixtures

In this section, we discuss the charge transport properties of the photoactive layers composed of P3HT:PCBM with and without processing additives. The transport parameters often derived from the space charge limited current measured under dark condition. The measured space charge limited currents were fitted with equation (5.8) which resulted from Mott-Gurney's law. We employed field-dependent mobility (FDM) equation to describe the transport in defect free medium. The relative permittivity was taken to be  $\epsilon = 3$  which is within the range of (3-5) for many polymers and the active layer thickness in this experiments was  $L = 120\text{nm}$ . The space charge current data taken from the OTFSCs prepared under the four conditions were compared with the current density equation of Eq. (5.8). The results displayed in Figure 5.9 show a summary of all the cases studied for the transport properties of the space charge limited current. This demonstrated, that, the trap free space charge limited theory agreed very well with the data. In this figure, the experimental data is represented by squares while the theoretical fits are represented by solids lines in accordance to Eq. (5.8). The average value of the zero field mobility and the field activation factor derived from those fits are tabulated in Table 5.6. There was clear evidence that the hole mobility obtained in DIO based device is better than the one of CN based device as well as the one without additive. However, their respective average values are in the range of the good mobility obtained so far in literatures with the highest value of  $0.1 \text{ cm}^2\text{V}^{-1}\text{s}^{-1}$  [110, 111]. The DMSO based device has a very low mobility compared to others, which contributed to the poor performance of the device. In fact, we noted that, there was a significant increase in hole mobility in DIO based device than the one with CN. This improvement in hole mobility could be attributed to the fact that DIO performs better as solvent for PCBM rather than for P3HT, which makes P3HT to neatly arrange itself into ordered domains, at the same time PCBM remains in the solution for a longer period there by avoiding excessive aggregation [91, 112]. Therefore, the higher hole mobility results from the high ordering of molecular structure. Furthermore, we noted that the mobility of the blend with CN based device increased compared to the device without additive. This could be attributed

to the fact that CN helps the distribution of PCBM into P3HT and allows a longer time for P3HT molecules to self-stack into highly ordered structure which enables high hole mobility and consequently a better fill factor.

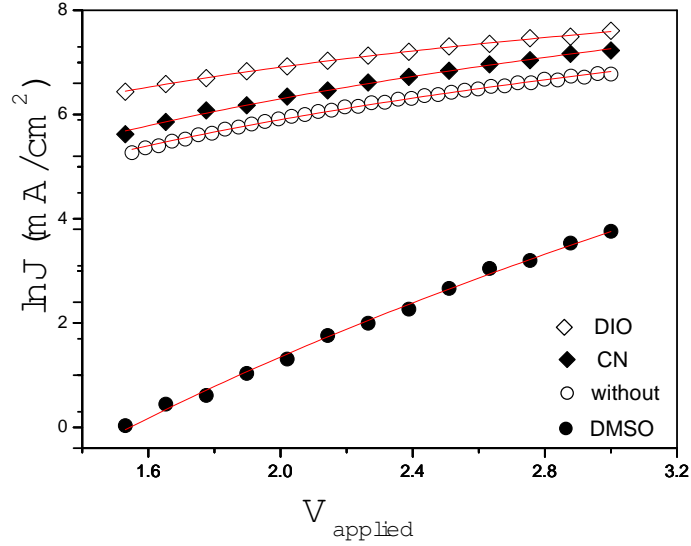


Figure 5.9:  $J$  vs  $V$  graph for a hole only diode of P3HT:PCBM prepared without and with solvent additives of OTFSC. The solid lines are computer fits according to Eq. (5.8) occurring at high forward biases, while the black squares are experimental data.

Table 5.6: Summary of the transport parameters.

P3HT:PCBM	$\mu_0$ ( $\text{cm}^2\text{V}^{-1}\text{s}^{-1}$ )	$\gamma$ ( $\text{cmV}^{-1/2}$ )
CF without additive	$1.83 \times 10^{-5}$	$1.56 \times 10^{-2}$
CF with DIO (3v%)	$1.65 \times 10^{-4}$	$-1.35 \times 10^{-2}$
CF with CN (3v%)	$2.40 \times 10^{-5}$	$2.07 \times 10^{-2}$
CF with DMSO (1v%)	$3.14 \times 10^{-9}$	$1.88 \times 10^{-1}$

## 5.5 Surface Morphologies of the Photoactive layers

The Scanning Electron Microscope (SEM) was used to characterize the surface morphology of the photoactive films produced by spin coating on the glass substrate of each device. Further information on the evolution of morphology resulting from the effect of additives on P3HT:PCBM OTFSC

active layer was also investigated. Energy Dispersive X-ray Spectroscopy (EDX) was conducted on the SEM images to find out the contents of the different features of the surface. The images reported in Figure 5.10 show a certain pattern involving the polymer chain and the distribution of PCBM and the EDX data taken from the islands of those samples indicate that, the lighter spots are rich in P3HT, while the darker spots are rich in PCBM. SEM image (Figure 5.10: top) of the P3HT:PCBM film prepared without additive, shows similar nanostructures with very little white spots at the surface of the film, this could be due to the weak inter-mixing of donors and acceptors at the molecular level. On the contrary, the film prepared with DIO (Figure 5.10: a) solvent additive shows homogeneous phase separation and interconnected regions between P3HT and PCBM components. It appears that the phase segregation between P3HT and PCBM domains in the film containing DIO processing solvent additive leads to much finer phase separation between the two materials without large aggregates of PCBM or P3HT. This small-scale phase separation which could be in the order the exciton diffusion length contributed to the large  $J_{sc}$  value obtained for this device. In contrast, the film containing CN (Figure 5.10: b) additive is quite poor and exhibited large-scale phase separated morphology where only a small fraction of the photo-generated excitons could diffuse to reach a P3HT:PCBM interface. This large-scale phase separated morphology could be attributed to the low  $J_{sc}$  observed on film surface. SEM image of the P3HT:PCBM film prepared with DMSO solvent additive, show heterogeneous nanostructures with formation of clusters at the surface of the film. The poor phase separation and formation of clusters as indicated (Figure 5.10: c) unfavors the creation of donors and acceptors at the interface, which resulted in to a poor performing device. The surface morphology confirmed the existence of the interpenetrating network of P3HT and PCBM in the photoactive layer. Such a network is suitable for the creation of the interfaces between the donor and acceptor, which could facilitate the dissociation of the exciton and the charges transport as well as the enhanced current in the device.

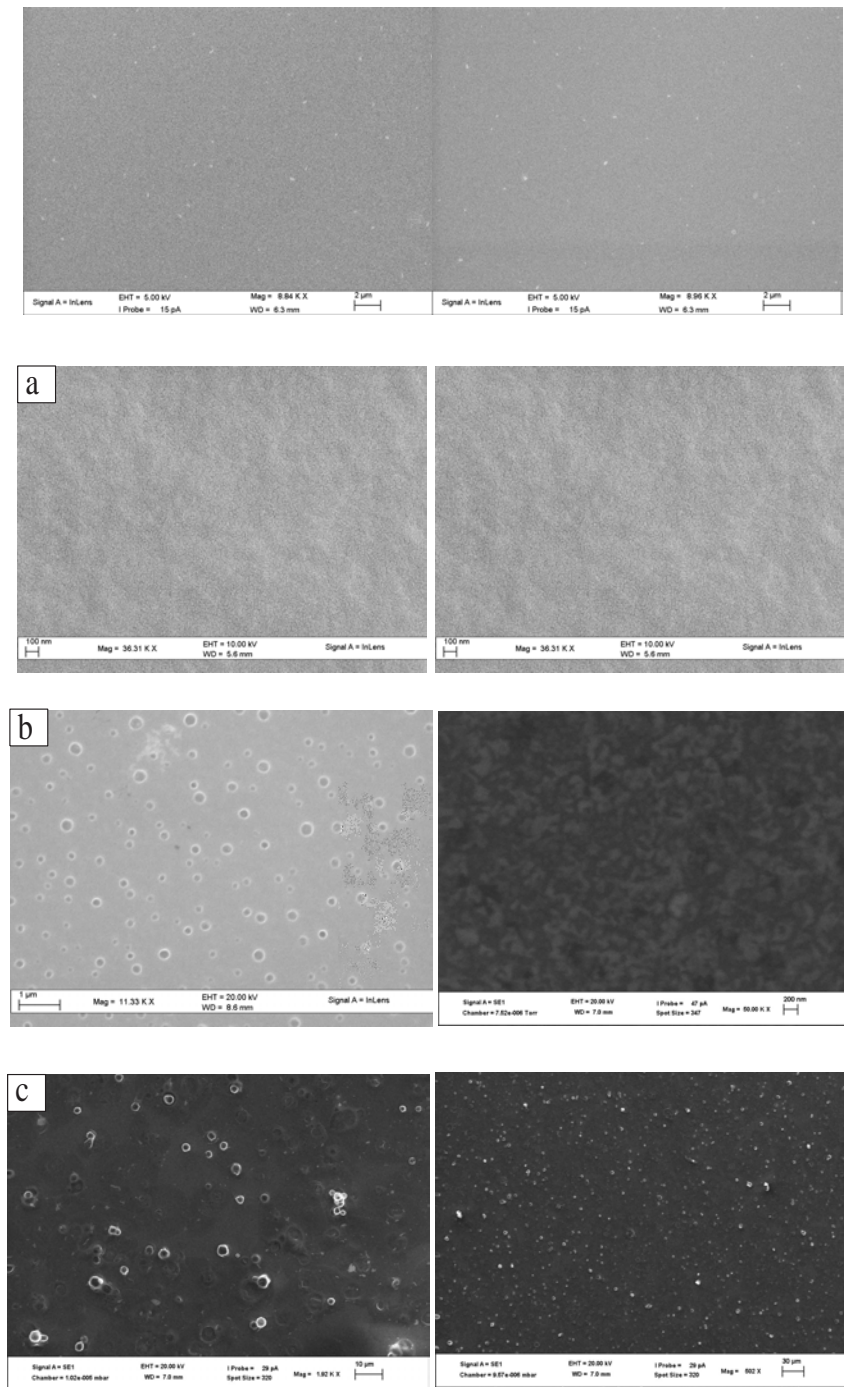


Figure 5.10: Scanning electron microscopy images of P3HT:PCBM blend films OTFSC spin coated from chloroform and mixed solvent: (top) without additive (a) with DIO; (b) with CN; and (c) with DMSO.

## Chapter 6

# Conclusions

Within the computational part of our research endeavour we studied a model blend of linear and cyclic polymers by means of extensive molecular dynamics computer simulations. For blends of linear and cyclic polymers, results from recent experiment using polystyrene polymer [12] provided evidence on the enrichment of linear chains at the surface, contradicting the once accepted conclusion from theory using Self-consistent Gaussian Field Theory [42] that cyclic polymers should be in excess at the surface independently of the molecular weight of the polymers. We found that the composition of linear polymers is in excess at the interface compared to cyclic polymers for short-chain lengths in agreement with experiment. Furthermore, increasing the molecular weight of the polymer chains ultimately results in the enrichment of cyclic chains at the surface agreeing with theory for the long chain limit. For the case of polymers with polystyrene chemistry, we predict a transition from linear chains enriching the surface to cyclic chains enriching the surface at a molecular weight in the range of 6000 to 10,000 g/mol.

We have explained the role of enthalpic and entropic factors in determining which of the two chain architectures enrich the surface at a given molecular weight. Our results demonstrate clearly that since cyclic polymers are way less flexible than linear polymers at small degrees of polymerization, they pack less efficiently and achieve a less than optimal number of pair interactions among their beads, which prevents them from decreasing their energy content as efficiently as linear polymers at the interface. We found the evident reason for this property in the severe constraint imposed on the flexibility of cyclic polymers by the loop topology when their chain length is small. In summary, for short chains linear polymers can achieve a lower interfacial free energy than cyclic polymers because they achieve a better minimization of their surface energy than cyclic chains and they maximize their entropy by exposing their chain-ends to the surface. Our conclusion in this regime is that linear enhancement at the interface is the result of an entropy-mediated process, where also the enthalpy is playing an important role.

In the long chain regime, we found that the loop constraint becomes less important in undermining the flexibility of polymer chains. Cyclic polymers are now likely to achieve a lower

interfacial free energy than linear polymers because they possess an higher conformational entropy since their surface energy becomes similar to the one of linear polymers. Our conclusion in this case is that the enhancement of the composition of cyclic polymers at the interface emerges as a genuine entropic process, where once again the loop topology of cyclic chains plays a major role since it prevents them from folding at the interface as efficiently as linear chains.

Besides the general interest of our findings within the field of polymer science, surface science, biomaterials, and surface chemistry, we also believe that our study is relevant for biological systems where the intrinsic topological constraints of cyclic polymers, including non-knotting and non-concatenation, are present in chromatin polymer models [23, 24]. These models apply physics-based approaches that highlight the importance of entropy for understanding nuclear organization, ultimately consisting in the packaging of a long linear polymer such as DNA into the highly crowded structure known as chromatin [113].

In the experimental work, organic thin film solar cells with and without processing solvent additives have been fabricated and characterized under ambient laboratory atmosphere. The performance of the device produced without solvent additive was comparable with solar cells produced under the same condition in the literatures. We have employed here three types of solvent additives DIO, CN and DMSO in chloroform based host solvent in order to be able to compare the miscibility of the P3HT:PCBM blend. According to the electrical measurements taken from the devices the performance of the film mixed with DIO solvent outperforms all other variety of solvent additives. We have recorded device parameters as high as  $J_{sc} = 11 \text{ mA/cm}^2$ ,  $V_{oc} = 0.47\text{V}$ ,  $\text{FF} = 60\%$  and  $\text{PCE} = 2.8\%$  which are far better than those devices without solvent additive. These results indicated that the power conversion efficiency has grown by 55% and the fill factor by 32% by using only 3% DIO solvent additive in P3HT:PCBM blend. The second best performing thin film organic solar cell was those devices whose active layer were mixed with 1-chloronaphthalene (CN) solvent additive. In this case, the power conversion efficiency rose to 2.2% which shows nearly a 22% growth. However, we found very low performance from those devices based on DMSO solvent additives. All the device parameters measured from DMSO based active layer were found to be well below the devices without solvent additive (reference sample).

The films morphologies were also investigated using SEM images taken from DIO, CN and DMSO additives based devices. We found strong correlation between the uniformity of the film with that of device performance. According the SEM images given in the thesis the film with DIO additive appeared to be very smooth compared to all other devices prepared in this investigation. This can be translated to the fact that the chloroform:DIO solvent could have favored the formation of good interpenetrating network which could facilitate the charge transport across the film. In fact, the space charge limited current investigated in this work compliment the same conclusion which confirms that DIO based devices have the highest charge mobility than all other devices. The relative higher boiling point of the processing solvent of CN ( $250^\circ\text{C}$ ) than the DIO ( $168^\circ\text{C}$ )

could have caused slow crystallization process of P3HT polymer which presumably influence the nanomorphology of the film. More investigations are need using other spectroscopy methods to understand the actual mechanisms of film formation in the preparation organic solar cell.

## Chapter 7

# Bibliography

- [1] R. L. Hirsch, R. Bezdek, and R. Wendling. Peaking of world oil production: Impacts, mitigation, and risk management. *Science Applications International Corporation/U.S. Department of Energy, National Energy Technology Laboratory*.
- [2] R. Po, C. Carbonera, A. Bernardi, F. Tinti, N. Camaioni, and Nadia. Polymer and carbon-based electrodes for polymer solar cells: Toward low-cost, continuous fabrication over large area. *Solar Energy Materials and Solar Cells*, **100**:97, 2012.
- [3] N. Yeh and P. Yeh. *Renewable and Sustainable Energy Reviews*, **21**:421, 2013.
- [4] S. H. Park, A. Roy, S. Beaupre, S. Cho, N. Coates, J. S. Moon, D. Moses, M. Leclerc, K. Lee, and A. J. Heeger. Bulk heterojunction solar cells with internal quantum efficiency approaching 100%. *Nature Photonics*, **3**:297–303, 2009.
- [5] C. K. Lee, C. W. Pao, and C. W. Chu. *Energy. Environ. Sci.*, **4**:4124, 2011.
- [6] M. L. Chabinyo. *Polymer Rev.*, **48**:463–492, (2008).
- [7] R. J. Kline, D. M. DeLongchamp, D. A. Fischer, E. K. Lin, L. J. Richter, M. L. Chabinyo, M. F. Toney, M. Heeney, and I. McCulloch. *Macromolecules*, **40**:7960–7965, 2007.
- [8] J. F. Chang, J. Clark, N. Zhao, H. Sirringhaus, D. W. Breiby, J. W. Andreasen, M. M. Nielsen, M. Giles, M. Heeney, and I. McCulloch. *Phys. Rev. B*, **74**:115–318, 2006.
- [9] A. Zen, M. Saphiannikova, D. Neher, J. Grenzer, S. Grigorian, U. Pietsch, U. Asawapirom, S. Janietz, U. Scherf, I. Lieberwirth, and G. Wegner. *Macromolecules*, **39**:2162–2171, 2006.
- [10] M. C. Gurau, D. M. DeLongchamp, B. M. Vogel, E. K. Lin, D. A. Fischer, S. Sambasivan, and L. J. Richter. *Langmuir*, **23**:834–842, 2007.
- [11] G. Subramanian and S. Shanbhag. *Macromolecules*, **41**:7239, 2008.

- [12] S. Wang, X. Li, R. L. Agapov, C. Wesdemiotis, and M. D. Foster. *ACS. Macro. Lett.*, **1**:1024–1027, 2012.
- [13] J. S. Lee, N. H. Lee, S. Peri, M. D. Foster, C. F Majkrzak, R. Hu, and D. T. Wu. *Phys. Rev. Lett*, **113**:225702, 2014.
- [14] J. D. Halverson, W. B. Lee, G. S. Grest, A. Y. Grosberg, and K. Kremer. *J. Chem. Phys.*, **134**:204904, 2011.
- [15] G. Subramanian and S. Shanbhag. *Phys. Rev. E*, **77**:011801, 2008.
- [16] S. f. Wang, S. Yang, J. Lee, B. Akgun, D. T. Wu, and M. D. Foster. *Phys. Rev. Lett*, **111**:068303, 2013.
- [17] K. Schäler, E. Oostas, K. Schröter, T. Thurn-Albrecht, W. H. Binder, and K. Saalwächter. *Macromolecules*, **44**:2743, 2011.
- [18] G. B. McKenna, G. Hadziioannou, P. Lutz, G. Hild, C. Strazielle, C. Straupe, and P. Rempp. *Macromolecules*, **20**:498, 1987.
- [19] M. Sikka, N. Singh, A. Karim, and F. S. Bates. *Phys. Rev. Lett*, **70**:307, 1993.
- [20] D. G. Walton, P. P. Soo, A. M. Mayes, S. J. S. Allgor, J. Fujii, L. G. Griffith, J. F. Ankner, H. Kaiser, J. Johansson, G. D. Smith, J. G. Barker, and S. K. Satija. *Macromolecules*, **30**:6947, 1997.
- [21] N. Ouarti, P. Viville, R. Lazzaroni, M. Schappacher, A. Deffieux, and R. Borsali. *Langmuir*, **21**:9085, 2005.
- [22] C. M. Kuo, S. J. clarson, and J. A. Semlyen. *Polymer*, **35**:4623, 1994.
- [23] J. Mateos-Langerak, M. Bohn, W. de Leeuw, O. Giromus, E. M. Manders, P. J. Verschure PJ, M. H. Indemans, H. J. Gierman, D. W. Heermann, R. van Driel, and S. Goetze. *Proc. Natl. Acad. Sci. U.S.A*, **22**:19234129, 2009.
- [24] G. Fudenberg and L. A. Mirny. *Curr. Opin. Genet. Dev*, **22**:115–124, 2012.
- [25] G. S. Grest and K. Kremer. *Phys. Rev. A*, **33**:3628, 1986.
- [26] K. Kremer and G. S. Grest. *J. Chem. Phys*, **92**:5057, 1990.
- [27] J. S. Higgins, K. Dodgson, and J. A. Semlyen. *Polymers*, **20**:553, 1979.
- [28] M. Ragnetti, D. Geiser, H. Hocker, and R. C. Oberthur. *Makromol. Chem*, **186**:1701, 1985.
- [29] J. Roovers. *J. Polym. Sci. Polym. Phys. Ed*, **23**:1117, 1985.

- [30] G. Hadziioannou, P. M. Cotts, G. Tenbrinke, C. C. Han, P. Lutzs, C. Strazielle, P. Rempp, and A. J. Kovacs. *Macromolecules*, **18**:493, 1987.
- [31] S. Geyler and T. Pakula. *Makromol. Chem. Rapid. Commun*, **9**:617, 1988.
- [32] B. V. S. Iyer, A. K. Lele, and S. Shanbhag. *Macromolecules*, **40**:5995, 2007.
- [33] M. Müller, J. P. Wittmer, and M. E. Cates. *Phys. Rev. E*, **53**:5063, 1996.
- [34] S. Brown and G. Szamel. *J. Chem. Phys*, **108**:4705, 1998.
- [35] S. Brown and G. Szamel. *J. Chem. Phys*, **109**:6184, 1998.
- [36] M. Müller, J. P. Wittmer, and M. E. Cates. *Phys. Rev. E*, **61**:4078, 2000.
- [37] S. Brown, T. Lenczycki, and G. Szamel. *Phys. Rev. E*, **63**:052801, 2001.
- [38] M. E. Cates and J. M. Deutsch. *J. Phys. (Paris)*, **47**:2121–2128, 1986.
- [39] J. D. Halverson, G. S. Grest, A. Y. Grosberg, and K. Kremer. *Phys. Rev. Lett*, **108**:038301, 2012.
- [40] T. Sakaue. *Phys. Rev. Lett*, **106**:167802, 2011.
- [41] T. Sakaue. *Phys. Rev. Lett*, **85**:021806, 2012.
- [42] D. T. Wu and G. H. Fredrickson. Effect of architecture in the surface segregation of polymer blends. *Macromolecules*, **29**:7919–7930, 1996.
- [43] R. A. Jones, E. J. Kramer, M. Rafailovich, J. Sokolov, and S. A. Schwarz. *Phys. Rev. Lett*, **62**:280, 1989.
- [44] A. Hariharan, S. K. Kumar, and T. P. Russell. *J. Chem. Phys*, **98**:4163, 1993.
- [45] U. Steiner, J. Klein, E. Eiser, A. Budkowski, and L. J. Fetters. *Science*, **258**:1126, 1992.
- [46] F. Scheffold, A. Budkowski, U. Steiner, E. Eiser, J. Klein, and L. J. Fetters. *J. Chem. Phys*, **104**:8795, 1996.
- [47] M. Sikka, N. Singh, F. S. Bates, A. Karim, S. K. Satija, and C. F. Majkrzak. *J. Phys. II (Paris)*, **4**:2231, 1994.
- [48] A. Yethiraj. Integral equation theory for the surface segregation from blends of linear and star polymers. *Computational and Theoretical Polymer Science*, **10**:115–123, 2000.
- [49] G. H. Fredrickson and J. P. Donley. *J. Chem. Phys*, **97**:8941, 1992.
- [50] A. Yethiraj, S. K. Kumar, A. Hariharan, and K. S. Schweizer. *J. Chem. Phys*, **100**:4691, 1994.

- [51] S. K. Kumar, A. Yethiraj, K. S. Schweizer, and F. A. M. Leermakers. *J. Chem. Phys.*, **103**:10, 1995.
- [52] A. Yethiraj. Entropic and enthalpic surface segregation from blends of branched and linear polymers. *Phys. Rev. Lett.*, **74**:2018–2021, 1995.
- [53] D. G. Walton and A. M. Mayes. *Phys. Rev. E*, **54**:2811, 1996.
- [54] R. Dickman and C. K. Hall. *J. Chem. Phys.*, **89**:3168, 1988.
- [55] E. Lee and Y. J. Jung. *Soft Matter*, **11**:6018, 2015.
- [56] D. M. Huang, R. Faller, K. Do, and A. J. Moule. *J. Chem. Theory. Comput.*, **6**:526–537, 2010.
- [57] D. M. Huang, A. J. Moule, and R. Faller. *Fluid. Phase. Equilibria*, **302**:21–25, 2011.
- [58] D. Reith, B. Müller, F. Müller-Plathe, and S. Wiegand. *J. Chem. Phys.*, **116**:9100–9106, 2002.
- [59] J. Ghosh, Q. Sun, and R. Faller. Point dependence and transferability of potentials in systematic structural coarse-graining: In coarse-graining of condensed phase and biomolecular systems. *Voth. G. A. Ed. CRC Press: Boca Raton FL*, pages 69–82, 2008.
- [60] G. Yu, J. Gao, J. C. Hummelen, F. Wudl, and A. J. Heeger. *Science*, **270**:1789, 1995.
- [61] S. E. Shaheen, C. J. Brabec, N. S. Sariciftci, F. Padinger, T. Fromherz, and J. C. Hummelen. *Appl. Phys. Lett.*, **78**:841, 2001.
- [62] G. Tessema. Charge transport across bulk heterojunction organic thin film. *Appl. Phys. A*, **106**:53–57, 2012.
- [63] E. A. A. Arbaba, B. A. Taleatua, and G. T. Mola. Ternary molecules blend organic bulk heterojunction solar cell. *Materials Science in Semiconductor Processing*, **40**:158–161, 2015.
- [64] V. Shrotriya, G. Li, Y. Yao, T. Moriarty, K. Emery, and Y. Yang. Accurate measurement and characterisation of organic solar cells. *Adv. Funct. Mater.*, **16**:2016, 2006.
- [65] B. Qi and J. Wang. *Phys. Chem. Chem. Phys.*, **15**:8972, 2013.
- [66] A. Moliton and J. M. Nunzi. How to model the behaviour of organic photovoltaic cells. *Polymer International*, **55**:583–600, 2006.
- [67] S. Yoo, B. Domercq, and B. Kippelen. Intensity-dependent equivalent circuit parameters of organic solar cells based on pentacene and c60. *Journal of Applied Physics*, **97**:103706–103706, 2005.

- [68] A. Cheknane and et al. An equivalent circuit approach to organic solar cell modelling. *Microelectron. J.*, **39**:1173–1180, 2008.
- [69] W. J. Potscavage, A. Sharma, and B. Kippelen. Critical interfaces in organic solar cells and their influence on the open-circuit voltage. *Accounts of Chemical Research*, **42**:1758–1767, 2009.
- [70] W. Shockley. The theory of p-n junction in semiconductor and p-n junction transistors. *Bell System Technical Journal*, **28**:435–489, 1949.
- [71] H. J. Snaith and R. H. Friend. *Thin Solid Films*, **567**:451–452, 2004.
- [72] H. Hoppe and N. S. Sariciftci. *J. Mater. Chem.*, **45**:16, 2006.
- [73] R. A. Marsh, C. Groves, and N. C. Greenham. *J. Appl. Phys.*, **101**:083509, 2007.
- [74] P. K. Watkins, A. B. Walker, and G. L. B. Verschoor. *Nano. Lett.*, **5**:1814, 2005.
- [75] T. Martens, J. DHaen, T. Munters, Z. Beelen, L. Goris, J. Manca, M. DOLieslaeger, D. Vanderzande, L. De Schepper, and R. Anderiessen. *Synth. Met.*, **138**:243–247, 2003.
- [76] H. Hoppe, M. Niggemann, C. Winder, J. Kraut, R. Hiesgen, A. Hinsch, D. Meissner, and N. S. Sariciftci. *Adv. Funct. Mater.*, **14**:1005–1011, 2004.
- [77] M. Rubinstein and R. H. Colby. *Polymers Physics*. Oxford University Press, Oxford, (2003).
- [78] M. Megnidio-Tchoukouegno, G. Pellicane, and M. Tsige. *Unpublished*.
- [79] S. Plimpton. *J. Comput. Phys.*, **117**:1, 1995.
- [80] S. F. Wang. *PhD dissertation*. The University of Akron, Ohio, USA, 2011.
- [81] D. Tsalikis, T. Koukoulas, and V. G. Mavrantzas. *React. Funct. Polym.*, **7**:80, 2014.
- [82] L. Liu, S. Parameswaran, A. Sharma, S. M. Grayson, H. S. Ashbaugh, and S. W. Rick. *J. Phys. Chem. B*, **118**:6491, 2014.
- [83] M. Tsige, G. Leuty, and J. Bedard. *J. Polym. Sci.*, **47**:2556, 2009.
- [84] Y. Y. Yimer, A. Dhinojwala, and M. Tsige. *J. Chem. Phys.*, **137**:044703, 2012.
- [85] E. Minima and A. Arnold. *Macromolecules*, **48**:4998, 2015.
- [86] S. F. Wang, Q. He, D. T. Wu, and M. D. Foster. *AIChE Conference Proceedings*, 2012.
- [87] V. Arrighi, S. Gagliardi, A. C. Dagger, J. S. Higgins J. A. Semlyen, and M. J. Shenton. *Macromolecules*, **37**:8057, 2004.
- [88] C. W. Tang. *Appl. Phys. Lett.*, **48**:183, 1986.

- [89] Z. He, C. Zhong, S. Su, M. Xu, H. Wu, and Y. Cao. *Nat. Photonics*, **6**:591, 2012.
- [90] D. C. Watters, J. Kingsley, H. Yi, T. Wang, A. Iraqi, and D. Lidsey. *Org. Electron*, **13**:1401, 2012.
- [91] J. Lee, W. Ma, C. J. Brabec, J. Yuen, J. S. Moon, J. Y. Kim, K. Lee, G. C. Bazan, and A. J. Heeger. *J. Am. Chem. Soc.*, **130**:3619–3623, 2008.
- [92] F. Zhang, K. G. Jespersen, C. Björström, M. Svensson, M. R. Andersson, K. Sundström, E. Moons, A. Yartsev, and O. Inganäs. Influence of solvent mixing on the morphology and performance of solar cells based on polyfluorene copolymer/fullerene blends. *Adv. Funct. Mater.*, **16**:667–674, 2006.
- [93] Y. Yao, J. Hou, Z. Xu, G. Li, and Y. Yang. Effects of solvent mixtures on the nanoscale phase separation in polymer solar cells. *Adv. Funct. Mater.*, **18**:1783–1789, 2008.
- [94] J. Peet, J. Y. Kim, N. E. Coates, W. L. Ma, D. Moses, A. J. Heeger, and G. C. Bazan. Efficiency enhancement in low-bandgap polymer solar cells by processing with alkane dithiols. *Nat. Mater.*, **6**:497–500, 2007.
- [95] J. S. Moon, C. J. Takacs, S. Cho, R. C. Coffin, H. Kim, G. C. Bazan, and A. J. Heeger. Effect of processing additive on the nanomorphology of a bulk heterojunction material. *Nano. Lett.*, **10**:4005–4008, 2010.
- [96] J. T. Rogers, K. Schmidt, M. F. Toney, E. J. Kramer, and G. C. Bazan. Structural order in bulk heterojunction films prepared with solvent additives. *Adv. Mater.*, **23**:2284–2288, 2011.
- [97] Z. Ma, E. Wang, M. E. Jarvid, P. Henriksson, O. Inganäs, F. Zhang, and M. R. Andersson. Synthesis and characterization of benzodithiopheneisoindigo polymers for solar cells. *J. Mater. Chem.*, **22**:2306–2314, 2012.
- [98] L. Li, H. Tang, H. Wu, G. Lu, and X. Yang. Effects of fullerene solubility on the crystallization of poly(3-hexylthiophene) and performance of photovoltaic devices. *Organic. Electronics*, **10**:1334–1344, 2009.
- [99] L. Li, H. Tang, H. Wu, G. Lu, and X. Yang. Effects of fullerene solubility on the crystallization of poly(3-hexylthiophene) and performance of photovoltaic devices. *Organic. Electronics*, **10**:1334–1344, 2009.
- [100] W. B. Liao, A. S. Liu, and W. Y. Chiu. Morphology and growth kinetics in poly(butylene terephthalate)/polyarylates based on bisphenol a isophthalate. *Macromolecular Chemistry and Physics*, **203**:294–300, 2002.

- [101] B. Nandan, L. D. Kandpal, and G. N. Mathur. Crystallization and melting behavior of poly(ether ether ketone)/poly(aryl ether sulfone) blends. *Journal of Applied Polymer Science*, **90**:2906–2918, 2003.
- [102] J. Peet, N. S. Cho, S. K. Lee, and G. C. Bazan. Transition from solution to the solid state in polymer solar cells cast from mixed solvents. *Macromolecules*, **41**:8655–8659, 2008.
- [103] G. Li, V. Shrotriya, J. Huang, Y. Yao, T. Moriarty, K. Emery, and Y. Yang. *Nat. Mater.*, **4**:864, 2005.
- [104] W. Ma, C. Yang, X. Gong, K. Lee, and A. J. Heeger. *Advanced Functional Materials*, **15**:1617, 2005.
- [105] M. A. Lampert and P. Mark. *Current injection in solids*. Academic Press, New York, (1970).
- [106] P. N. Murgatroyd. *J. Phys. D*, **3**:151, 1970.
- [107] J. T. Bell and G. T. Mola. *Physica B: Condensed Matter*, **437**:63–66, 2014.
- [108] M. Vosgueritchian, D. J. Lipomi, and Z. Bao. *Adv. Funct. Mater.*, **22**:421–428, 2012.
- [109] K. Vandewal, A. Gadisa, W. D. Oosterbaan, S. Bertho, F. Banishoeib, I. V. Severen, L. Lutsen, T. J. Cleij, D. Vanderzande, and J.V. Manca. The relation between open-circuit voltage and the onset of photocurrent generation by charge-transfer absorption in polymerfullerene bulk heterojunction solar cells. *Advanced Functional Materials*, **18**:2064–2070, 2008.
- [110] H. Zhou, Y. Zhang, J. Seifert, S. D. Collins, C. Luo, and G. C. Bazan et al. High-efficiency polymer solar cells enhanced by solvent treatment. *Adv. Mater.*, **25**:4636–4643, 2013.
- [111] O. Ramírez, V. Cabrera, and L. M. Reséndiz. Optimum ratio of electron-to-hole mobility in P3HT:PCBM organic solar cells. *Opt. Quant. Electron*, pages 1291–1296, 2013.
- [112] F. C. Chen, H. C. Tseng, and C. J. Ko. *Applied Physics Letters*, **92**:103316, 2008.
- [113] K. Luger, M. L. Dechassa, and D. J. Tremethick. *Nat. Rev. Mol. Cell Biol.*, **13**:436–447, 2012.